

## INFORMATION TO USERS

This manuscript has been reproduced from the microfilm master. UMI films the text directly from the original or copy submitted. Thus, some thesis and dissertation copies are in typewriter face, while others may be from any type of computer printer.

**The quality of this reproduction is dependent upon the quality of the copy submitted.** Broken or indistinct print, colored or poor quality illustrations and photographs, print bleedthrough, substandard margins, and improper alignment can adversely affect reproduction.

In the unlikely event that the author did not send UMI a complete manuscript and there are missing pages, these will be noted. Also, if unauthorized copyright material had to be removed, a note will indicate the deletion.

Oversize materials (e.g., maps, drawings, charts) are reproduced by sectioning the original, beginning at the upper left-hand corner and continuing from left to right in equal sections with small overlaps.

Photographs included in the original manuscript have been reproduced xerographically in this copy. Higher quality 6" x 9" black and white photographic prints are available for any photographs or illustrations appearing in this copy for an additional charge. Contact UMI directly to order.

ProQuest Information and Learning  
300 North Zeeb Road, Ann Arbor, MI 48106-1346 USA  
800-521-0600

UMI<sup>®</sup>



**University of Alberta**

**DETERMINATION OF THE PHYSICAL PROPERTIES OF MELTS**

**BY**

**STEVEN JOHN ROACH**



A thesis submitted to the Faculty of Graduate Studies and Research in partial fulfillment  
of the requirements for the degree of Master of Science in Chemical Engineering.

**Department of Chemical & Materials Engineering**

**Edmonton, Alberta**

**Spring 2001**



**National Library  
of Canada**

**Acquisitions and  
Bibliographic Services**

**395 Wellington Street  
Ottawa ON K1A 0N4  
Canada**

**Bibliothèque nationale  
du Canada**

**Acquisitions et  
services bibliographiques**

**395, rue Wellington  
Ottawa ON K1A 0N4  
Canada**

*Your file Votre référence*

*Our file Notre référence*

The author has granted a non-exclusive licence allowing the National Library of Canada to reproduce, loan, distribute or sell copies of this thesis in microform, paper or electronic formats.

The author retains ownership of the copyright in this thesis. Neither the thesis nor substantial extracts from it may be printed or otherwise reproduced without the author's permission.

L'auteur a accordé une licence non exclusive permettant à la Bibliothèque nationale du Canada de reproduire, prêter, distribuer ou vendre des copies de cette thèse sous la forme de microfiche/film, de reproduction sur papier ou sur format électronique.

L'auteur conserve la propriété du droit d'auteur qui protège cette thèse. Ni la thèse ni des extraits substantiels de celle-ci ne doivent être imprimés ou autrement reproduits sans son autorisation.

0-612-60491-8

**Canada**

**University of Alberta**

**Library Release Form**

**Name of Author:** STEVEN JOHN ROACH

**Title of Thesis:** DETERMINATION OF THE PHYSICAL PROPERTIES OF MELTS

**Degree:** Master of Science

**Year this Degree Granted:** 2001

Permission is hereby granted to the University of Alberta Library to reproduce single copies of this thesis and to lend or sell such copies for private, scholarly or scientific research purposes only.

The author reserves all other publication and other rights in association with the copyright in this thesis, and except as herein before provided, neither the thesis nor any substantial portion thereof may be printed or otherwise reproduced in any material form whatever without the author's prior written permission.

**Signature:** Steven Roach.

Advanced Materials and Processing Laboratory  
536 Chemical/Mineral Building  
University of Alberta  
Edmonton, Alberta  
CANADA  
T6G 2G6

**Date:** April 4 / 2001.

**University of Alberta**

**Faculty of Graduate Studies and Research**


The undersigned certify that they have read, and recommended to the faculty of Graduate Studies and Research for acceptance, a thesis entitled DETERMINATION OF THE PHYSICAL PROPERTIES OF MELTS submitted by STEVEN JOHN ROACH in partial fulfillment of the requirements for the degree of Master of Science in Chemical Engineering.

  
Dr. Hani Henein (Supervisor)

  
Dr. Zhenghe Xu (Committee Member)

  
Dr. Janet Elliott (Committee Member)

  
Dr. Tom W. Forest (Committee Member)

Date Thesis Approved: 

## **ABSTRACT**

It has been determined that surface tension is required in quantifying the fluid dynamics of a stream exiting an orifice under the influence of gravity under certain circumstances. Liquids of high surface tension (i.e. melts) and low density typically exhibit low Bond numbers and indicate situations where surface tension must be included in the formulation relating flow rate and head with the discharge coefficient.

A new formulation is presented that relates experimental quantities of head and flow rate, with surface tension, viscosity and density, facilitating the calculation of all three properties. Experiments performed with molten aluminum as a function of temperature indicate that surface tension and density is within 6.5% and 2.5% respectively of values obtained in the literature. The viscosity has been determined to be significantly less than data reported from other sources. Results are also presented for AZ91D magnesium alloy.

## **ACKNOWLEDGEMENTS**

The author wishes to thank his supervisor, Dr. Hani Henein, for his continuous support, guidance, and dedication during the course of his degree. The author is also indebted to his committee members consisting of Dr. Suzanne Kresta, Dr. Zhenghe Xu, Dr. Janet Elliott, and Dr. Tom W. Forest who have proven to be an excellent source of information and guidance during the completion of this work. The author would like to thank David Leon and other employees from Alcoa Inc. for producing an excellent collaborative effort. Financial support from the National Research Council of Canada made this work possible.

The Advanced Materials and Processing Laboratory provided an environment where others contributed significantly to the completion of this Thesis. Many friendships were forged in the process. The support of Dr. B. Wiskel, Craig Owens, Arvind Prasad, Manual Reider, Tuyet Le, Zaheer Champasi, and many others past and present is a cornerstone of the author's experience at the University of Alberta. Others in the department to be acknowledged for design work and technical support are Bob Smith, Bob Konzic, Bob Scott, and Walter Boddez. The author also appreciates the aid of the Business Development Bank of Canada in Toronto for services rendered during the printing of this document.

Finally, the author wishes to express his gratitude to his family for the continuous love and support. Thanks Mom, Dad and Mark.



## **TABLE OF CONTENTS**

	<b>Page #</b>
<b>CHAPTER 1: INTRODUCTION</b>	<b>1</b>
<b>CHAPTER 2: LITERATURE REVIEW</b>	<b>6</b>
<b>2.1 Surface Tension of Molten Metals</b>	<b>6</b>
<b>2.1.1 Gibbs Adsorption Equation: Effects of Composition</b>	<b>9</b>
<b>2.1.2 Dependence on Temperature</b>	<b>18</b>
<b>2.1.3 Dynamic Surface Tension</b>	<b>21</b>
<b>2.1.4 Techniques to Measure Surface Tension</b>	<b>23</b>
<b>2.1.5 Experimental Data</b>	<b>34</b>
<b>2.2 Viscosity of Molten Metals</b>	<b>42</b>
<b>2.2.1 Theoretical Determination of Viscosity</b>	<b>43</b>
<b>2.2.2 Techniques to Measure Viscosity</b>	<b>44</b>
<b>2.2.3 Experimental Data</b>	<b>47</b>
<b>2.3 Density of Molten Metals</b>	<b>50</b>
<b>2.3.1 Techniques to Measure Density</b>	<b>51</b>
<b>2.3.2 Experimental Data</b>	<b>54</b>
<b>2.4 The Saybolt Viscometer</b>	<b>55</b>
<b>2.5 Conclusions</b>	<b>61</b>
<b>CHAPTER 3: EXPERIMENTAL</b>	<b>63</b>
<b>3.1 Low Temperature Apparatus</b>	<b>63</b>
<b>3.1.1 Orifice Plates</b>	<b>66</b>

3.1.2	Procedure for Low Temperature Experiments	67
3.2	Overview of High Temperature Apparatus	68
3.2.1	Orifice Plates	70
3.2.2	Crucibles	72
3.2.3	Induction Furnace	72
3.2.4	Purging Gas	74
3.2.5	Metal Selection	76
3.2.6	Data Acquisition System	78
3.2.7	Oxygen Analyzer	80
3.2.8	Procedure for High Temperature Experiments	81
3.3	Conclusions	83
CHAPTER 4:	CHARACTERIZATION OF FRICTIONAL LOSSES	84
4.1	Flow From a Draining Vessel: Neglecting Surface Tension	84
4.1.1	Formulation	84
4.1.2	Results	90
4.2	Flow From a Draining Vessel: A New Approach	93
4.2.1	Formulation	94
4.2.2	Results	97
4.3	Considerations for High Temperature Fluids	98
4.4	Conclusions	104

<b>CHAPTER 5:</b>	<b>FORMULATION OF PHYSICAL PROPERTY MEASUREMENTS</b>	<b>106</b>
<b>5.1</b>	<b>Formulation of Surface Tension Measurements: Fluids with Known Density and Viscosity</b>	<b>106</b>
5.1.1	Error Analysis	108
5.1.2	Data Analysis	110
5.1.3	Surface Tension of Water at 321.5 K	115
<b>5.2</b>	<b>Formulation for Simultaneous Determination of Surface Tension, Viscosity, and Density</b>	<b>119</b>
5.2.1	Error Analysis	124
5.2.1.1	Surface Tension	125
5.2.1.2	Density	125
5.2.1.3	Viscosity	128
5.2.1.4	Summary of Propagation of Errors	133
5.2.2	Data Analysis	136
5.2.3	The Surface Tension, Viscosity and Density of Aluminum at 1073 K	141
<b>5.3</b>	<b>Conclusions</b>	<b>145</b>
<b>CHAPTER 6:</b>	<b>DISCUSSION</b>	<b>148</b>
<b>6.1</b>	<b>Density</b>	<b>148</b>
6.1.1	Density of Aluminum	149
6.1.2	Density of AZ91D	151
<b>6.2</b>	<b>Viscosity of Aluminum and AZ91D Alloy</b>	<b>154</b>
<b>6.3</b>	<b>Surface Tension</b>	<b>159</b>
6.3.1	Surface Tension of Aluminum	159
6.3.2	Surface Tension of AZ91D Alloy	163

<b>6.4</b>	<b>Conclusions</b>	<b>165</b>
<b>CHAPTER 7:</b>	<b>SUMMARY</b>	<b>167</b>
<b>REFERENCES</b>		<b>171</b>
<b>APPENDIX A:</b>	<b>QUANTIFYING TRANSIENT TERMS</b>	<b>177</b>
<b>APPENDIX B:</b>	<b>MULTIPLE NON-LINEAR REGRESSION PROGRAM</b>	<b>180</b>
<b>APPENDIX C:</b>	<b>SURFACE TENSION AND VISCOSITY OF ALUMINUM (REGRESSION ON ALL THREE PROPERTIES)</b>	<b>186</b>
<b>APPENDIX D:</b>	<b>OXYGEN PARTIAL PRESSURE</b>	<b>188</b>

## LIST OF FIGURES

	<b>Page #</b>
Figure 2.1: Molecular forces acting at an interface separating a liquid from a gas.	7
Figure 2.2: Interface region representing the concentration gradient that exist between phases $\alpha$ and $\beta$ .	8
Figure 2.3: Surface energy for a variety of fluids plotted against the respective heats of vaporization [10].	9
Figure 2.4: Surface tension of Al-based alloys as functions of alloying composition at 973 K. Atmosphere and oxygen concentration are not specified. (From Lang, G. [11]).	10
Figure 2.5: Effect of oxygen present as a solute on the surface tension of molten iron. Temperature and atmosphere are not specified. (From Keene, B.J. [7]).	11
Figure 2.6: Effects of oxygen present in the gas phase on the surface tension of copper. Temperature and atmosphere are not specified. (From Keene, B.J. [7]).	12
Figure 2.7: a) Interface region separating phases $\alpha$ and $\beta$ . b) Dividing surface used in Gibbs Model approximating the interface region separating phases $\alpha$ and $\beta$ .	14
Figure 2.8: Surface tension of iron-3% carbon alloy with varying concentrations of chromium at 1623 K. Atmosphere and oxygen concentration are not specified. (From Whalen et al. [15]).	18
Figure 2.9: Temperature dependence of surface tension as a function of lead concentration exhibiting positive values for $d\sigma/dT$ . Temperature, atmosphere, oxygen concentration are not specified. (From Joud and Passerone, [5]).	21
Figure 2.10: Characteristic times of a 0.01m diameter droplet to be saturated with oxide at a total pressure of oxygen of 1Pa, for various metallic systems (From Ricci et al. [40]).	23
Figure 2.11: Dimensions of sessile droplet required for calculation using the analysis approach of Bashford and Adams [42].	25

Figure 2.12:	Dimensions of pendant droplet required for calculation using formulation by Andreas et al. [43] (From Iida and Guthrie, [2]).	26
Figure 2.13:	Capillary rise method for determining the surface tension of a liquid.	31
Figure 2.14:	Surface tension of high purity aluminum, and aluminum deliberately contaminated with oxygen (From Levin et al. [19]).	36
Figure 2.15:	Surface tension of aluminum and alumina as a function of temperature, quoted from a variety of sources (From Kaptay [8]).	37
Figure 2.16:	Surface tension dependence on the coverage of $\text{Al}_2\text{O}_3$ of pure aluminum determined experimentally [32], and theoretically [37] at 973 K.	39
Figure 2.17:	Surface of aluminum subjected to coverage of $\text{Al}_2\text{O}_3$ : a) $X < 0.3$ ; b) $X > 0.5$ .	39
Figure 2.18:	Velocity profile of fluid subjected to external force.	42
Figure 2.19:	Experimental viscosity of molten aluminum as a function of temperature from different sources.	48
Figure 2.20:	Viscosity of aluminum and magnesium quoted in the literature [17,52].	50
Figure 2.21:	Dimensions of the Saybolt viscometer.	60
Figure 3.1:	Low temperature apparatus.	64
Figure 3.2:	Orifice plate design for low temperature apparatus.	66
Figure 3.3:	High temperature apparatus.	69
Figure 3.4:	Orifice plate dimensions for aluminum and AZ91D experiments.	71
Figure 3.5:	Schematic of clay graphite crucible used for aluminum and AZ91D experiments.	73
Figure 3.6a:	Time required to heat 1.275 kg Aluminum to 1173 K. Aluminum Test# 29.	75

Figure 3.6b:	Time required to heat 0.62 kg AZ91D to 1073 K. AZ91D Test# 4.	76
Figure 3.7:	Data acquisition system used to acquire loadcell, thermocouple, and oxygen sensor data.	79
Figure 4.1:	Schematic of draining vessel depicting flow rate of a fluid through an orifice placed at the bottom.	85
Figure 4.2:	Control element on streamline neglecting frictional losses.	86
Figure 4.3:	Cumulative mass versus time for water at 293 K through a 0.003m Teflon orifice plate from an initial head of approximately 0.17m.	92
Figure 4.4:	Head versus time for water at 293 K through a 0.003m Teflon orifice plate from an initial head of approximately 0.17m.	92
Figure 4.5:	$C_d$ versus $Re_{exp}$ , calculated using Equation (76) for a 0.003m diameter orifice draining under the influence of gravity. Ethylene glycol and water are presented at different temperatures.	93
Figure 4.6:	Radius of curvature defining the gas-liquid interface of a free jet.	95
Figure 4.7:	Pressure acting at orifice tip for stream of liquid exposed to the atmosphere.	95
Figure 4.8:	$C_d$ versus $Re_{exp}$ , calculated using Equations (90) for a 0.003m diameter orifice draining under the influence of gravity. Ethylene glycol and water are presented at different temperatures.	98
Figure 4.9:	Dependence of the Bond and Froude relation on the density-surface tension ratio.	100
Figure 4.10:	Relative magnitude of Bond numbers for a variety of liquids. Density and surface tension are obtained from Iida and Guthrie [2].	101
Figure 4.11:	Water: Accuracy in neglecting surface energy for variable orifice design, for heads ranging from 0.1m to 0.01m.	103

Figure 4.12:	Molten iron: Accuracy in neglecting surface energy for variable orifice design, for heads ranging from 0.1m to 0.01m.	103
Figure 4.13:	Molten aluminum: Accuracy in neglecting surface energy for variable orifice design, for heads ranging from 0.1m to 0.01m.	104
Figure 5.1:	Experimental head measurements for water at 321.5 K.	111
Figure 5.2:	Deviations between experimental head and calculated head for water at 321.5 K.	112
Figure 5.3:	Cumulative mass as a function of time for water at 321.5 K through a 0.003m diameter Teflon orifice.	113
Figure 5.4:	Calibration for a 0.003m diameter orifice hole using water at room temperature.	114
Figure 5.5:	Experimental surface tension as a function of head for water at 321.5 K for four separate calibrations.	116
Figure 5.6:	Maximum head height determined for a specified error in surface tension for water draining through a 0.003m diameter orifice at 321.5 K.	118
Figure 5.7:	Average surface tension of water at 321.5 K.	119
Figure 5.8:	Errors in property measurements as a function of $h$ and $Q_{exp}$ , due to errors in $Q_{exp}$ and $C_d$ .	134
Figure 5.9:	Errors in property measurements as a function of $C_d$ , due to errors in $Q_{exp}$ and $C_d$ .	135
Figure 5.10:	Errors in property measurements as a function of $r_o$ , due to errors in $h$ and $Q_{exp}$ .	136
Figure 5.11:	Volume within the crucible corresponding to a particular head height.	138
Figure 5.12:	Experimental head measurements for aluminum at 1073 K. Aluminum Test #32.	139
Figure 5.13:	Cumulative mass versus time for aluminum at 1073 K. Aluminum Test #32.	140



Figure 5.14:	Frictional characteristics of 0.005m orifice used for high temperature experiments.	141
Figure 5.15:	The experimental surface tension determined for aluminum at 1073 K, with expected error represented by the solid bars. Aluminum Test #32.	144
Figure 5.16:	The experimental viscosity determined for aluminum at 1073 K, with expected error represented by the solid bars. Aluminum Test #32.	144
Figure 5.17:	The experimental density determined for aluminum at 1073 K, with expected error represented by the solid bars. Aluminum Test #32.	145
Figure 6.1:	Density of 99.95% aluminum as a function of temperature and compared with sources in the literature [2,17].	150
Figure 6.2:	Density of AZ91D alloy as a function of temperature compared with theoretical relations [17].	153
Figure 6.3:	Viscosity of 99.95% purity aluminum as a function of temperature compared with sources in the literature.	156
Figure 6.4:	Viscosity of AZ91D as a function of temperature.	157
Figure 6.5:	Surface tension of 99.95% aluminum as a function of temperature compared with sources in the literature [2,7,32].	161
Figure 6.6:	Surface tension of AZ91D as a function of temperature compared with sources in the literature [17,58].	164
Figure A.1:	Velocity at reference points 1 and 2 indicated in Figure 4.1 as a function of time.	178
Figure A.2:	Discharge coefficient as a function of Reynolds number taking into account transient terms in the formulation.	179
Figure C.1:	Surface tension of aluminum as a function of temperature determined through multiple non-linear regression on all three properties.	186

Figure C.2:	Viscosity of aluminum as a function of temperature determined through multiple non-linear regression on all three properties.	187
Figure D.1:	Representation for the partial pressure of oxygen as a function of temperature during a purging and heating cycle.	188
Figure D.2:	Oxygen partial pressure during the purging and heating cycle for Aluminum Test #31 up to 973 K.	190
Figure D.3:	Oxygen partial pressure during the purging and heating cycle for Aluminum Test #38 up to 1023 K.	191
Figure D.4:	Oxygen partial pressure during the purging and heating cycle for Aluminum Test #35 up to 1073 K.	192
Figure D.5:	Oxygen partial pressure during the purging and heating cycle for Aluminum Test #39 up to 1173 K.	193
Figure D.6:	Oxygen partial pressure during the purging and heating cycle for AZ91D Test #2 up to 967 K.	194

## LIST OF TABLES

	<b>Page #</b>
Table 2.1: Surface tension of aluminum quoted from a variety of sources. The temperature coefficient, atmosphere and purity are included. SD: Sessile Drop. MBP: Maximum Bubble Pressure.	<b>35</b>
Table 2.2: Surface tensions of aluminum and magnesium from sources in the literature [2,7,17,32].	<b>40</b>
Table 2.3: Surface tensions of Mg-Al-Zn-Mn alloys as a function of alloying composition [58].	<b>41</b>
Table 2.4: Viscosity of aluminum and magnesium from sources in the literature [17,52].	<b>49</b>
Table 2.5: Density of aluminum and magnesium from sources in the literature [2,17].	<b>55</b>
Table 2.6: Standard dimensions of the Saybolt Universal viscometer.	<b>61</b>
Table 3.1: Power requirements of induction furnace.	<b>74</b>
Table 3.2: Percent of elements found as impurities present in aluminum [62].	<b>77</b>
Table 3.3: Percent of elements added to or contained within AZ91D alloy [9].	<b>77</b>
Table 5.1: Polynomial constants that describe the discharge coefficient as a function of Reynolds number.	<b>116</b>
Table 5.2: Comparison between experimental surface tension and literature value for water at 321.5 K [61].	<b>119</b>
Table 5.3: Physical properties of aluminum determined by using different density values to calculate head at 1073 K.	<b>143</b>
Table 5.4: Summary of results for aluminum at 1073 K in comparison to literature quantities.	<b>146</b>
Table 6.1: Density of 99.95% aluminum determined experimentally.	<b>149</b>

Table 6.2:	Temperature dependence of density determined from experiments and from sources in the literature [2,17].	150
Table 6.3:	Density of AZ91D alloy determined experimentally.	151
Table 6.4:	Temperature dependence of density determined from experiments, and from the average values taken from sources in the literature [17].	154
Table 6.5:	Viscosity of 99.95% aluminum determined experimentally.	155
Table 6.6:	Viscosity of AZ91D alloy determined experimentally.	156
Table 6.7:	Surface tension of 99.95% aluminum determined experimentally.	160
Table 6.8:	Temperature dependence of surface tension determined from experiments and from sources in the literature [2,7,17].	162
Table 6.9:	Surface tension of AZ91D alloy determined experimentally.	163

## NOMENCLATURE

- $A$  = Constant in Arrhenius' formula ( $\text{Ns/m}^2$ ).
- $A_c$  = Cross sectional area for Bernoulli formulation ( $\text{m}^2$ ).
- $A_{m1}$  = Resonant amplitude of oscillating plate method in air (m).
- $A_{m2}$  = Resonant amplitude of oscillating plate method in liquid (m).
- $A_r$  = Surface area ( $\text{m}^2$ ).
- $a$  = Polynomial constant describing 3rd order term in polynomial fit of the discharge coefficient curve.
- $B$  = Constant in Arrhenius' formula (J/mole).
- $Bo$  = Bond number =  $\rho g r h / \sigma$  (no units).
- $b$  = Polynomial constant describing 2nd order term in polynomial fit of the discharge coefficient curve.
- $C_d$  = Discharge coefficient (no units).
- $C_m$  = Cumulative mass (kg).
- $\dot{C}_1$  = Constant used in converting Saybolt Universal or Furol seconds to kinematic viscosity ( $\text{m}^2/\text{s}^2$ ).
- $\dot{C}_2$  = Constant used in converting Saybolt Universal or Furol seconds to kinematic viscosity ( $\text{m}^2$ ).
- $c$  = Polynomial constant describing 1st order term in polynomial fit of the discharge coefficient curve.
- $d$  = Polynomial constant describing the y-intercept of the polynomial fit of the discharge coefficient curve.
- $d_{\text{cap}}$  = Diameter of orifice of the Saybolt viscometer (m).
- $d_{\text{tube}}$  = Outer diameter of the outlet of the orifice of Saybolt viscometer (m).
- $d_v$  = Diameter of vessel or container of the Saybolt viscometer (m).
- $F$  = Helmholtz free energy (J).

$F_o$  = Force (N).  
 $Fr$  = Froude number =  $u_{theo}^2/(2gh)$  (no units).  
 $g$  = Gravitational constant ( $m/s^2$ ).  
 $\hat{h}$  = Average head for Saybolt viscometer (m).  
 $h$  = Liquid head above a point of reference (m).  
 $j$  = Constant from Bashworth and Adams table for sessile drop measurements (no units).  
 $K_e$  = Equilibrium constant (no units).  
 $l$  = Correction factor related to the shape of the meniscus for detachment techniques (no units).  
 $l_{cap}$  = Length of orifice tube of Saybolt viscometer (m).  
 $M$  = Molecular weight (kg/mole).  
 $m$  = Mass (kg).  
 $n$  = Number of moles (no units).  
 $P$  = Pressure (Pa).  
 $Q$  = Flow rate ( $m^3/s$ ).  
 $q$  = Constant from Bashworth and Adams table for sessile drop measurements (no units).  
 $R$  = Radius of curvature (m).  
 $Re$  = Reynolds number =  $\rho 2r_o u / \mu$  (no units).  
 $r$  = radius (m).  
 $S$  = Entropy (J/K).  
 $s$  = Specific entropy ( $J/m^2K$ ).  
 $T$  = Temperature (K).

- $t$  = Time (s).
- $u$  = Velocity (m/s).
- $U$  = Internal energy (J).
- $\hat{u}$  = Average velocity of liquid through the orifice tube of the Saybolt viscometer (m/s).
- $\nu$  = Atomic volume ( $\text{m}^3/\text{mole}$ ).
- $V$  = Volume ( $\text{m}^3$ ).
- $V_d$  = Volume discharged from Saybolt viscometer =  $6.0 \times 10^{-5} \text{ m}^3$  ( $60 \text{ cm}^3$ ).
- $\hat{w}$  = Constant from Harkins and Brown tables for drop weight measurements (no units).
- $\Delta w_{\text{ob}}$  = Difference in weight of object for Archimedean determination of density (N).
- $X$  = Maximum width of sessile droplet or pendant droplet (m).
- $X'$  = Width dimension on pendant drop dependant on the dimension  $X$  (no units).
- $x$  = Mole fraction (no units).
- $Y$  = Apparatus constant for oscillating plate method ( $\text{kg}^2 \text{s}^{-2} \text{m}^{-4}$ ).
- $y$  = Shape factor from Andreas tables for pendant drop measurements (no units).
- $Z$  = Distance between geometric center and top of sessile droplet (m).
- $z$  = Distance on z-axis (m).
- $\alpha$  = Symbol corresponding to phase " $\alpha$ ".
- $\beta$  = Symbol corresponding to phase " $\beta$ ".
- $\delta$  = Error in a measurement. Also represents standard deviation.
- $\varepsilon$  = Interaction coefficient (no units).
- $\Gamma$  = Surface excess-concentration on gas-liquid interface ( $\text{moles/m}^2$ ).
- $\gamma$  = Activity coefficient (no units).

- $\eta$  = Viscosity ( $\text{Nsm}^{-2}$ ).
- $\lambda$  = Interfacial tension ( $\text{N/m}$ ).
- $\mu$  = Chemical potential ( $\text{J/mole}$ ).
- $\nu$  = Kinematic viscosity ( $\text{m}^2/\text{s}$ ).
- $\theta$  = Contact angle (degrees).
- $\rho$  = Density ( $\text{kg/m}^3$ ).
- $\sigma$  = Surface tension of liquid ( $\text{N/m}$ ).
- $\sigma_e$  = Surface tension of liquid at equilibrium ( $\text{N/m}$ ).
- $\sigma_o$  = Pure dynamic surface tension of liquid ( $\text{N/m}$ ).
- $\tau$  = Shear stress ( $\text{N/m}^2$ ).
- $\omega$  = Frequency of oscillation for levitating-drop technique ( $\text{Hz}$ ).
- $\xi$  = Kinetic energy correction factor for Saybolt viscometer (m).
- $\psi$  = Couette correction factor for Saybolt viscometer (m).

## SUBSCRIPTS

- cap: Capillary.
- curve "a": Location describe by radius of curvature.
- curve "b": Location described by radius of curvature.
- d: Droplet.
- exp: Experimental.
- g: Gauge.
- GS: Gas-Substrate Interface.
- i: Chemical component "i".



**j:** Iteration number for mutiple non-linear regression analysis.

**LS:** Liquid-Substrate Interface.

**m:** Melting point (or liquidus point).

**Max:** Maximum.

**o:** Orifice.

**ob:** Object.

**poly:** Polynomial.

**r:** Ring.

**St:** Saturation.

**theo:** Theoretical.

**v:** Vessel.

**vap:** Vaporization

**$\sigma$ :** Surface Tension.

#### **SUPERSCRIPTS**

**s:** Location corresponding to gas-liquid interface.

**$\alpha$ :** Denoting phase “ $\alpha$ ”.

**$\beta$ :** Denoting phase “ $\beta$ ”.

## **CHAPTER 1: INTRODUCTION**

Knowledge of the physical properties of melts is of fundamental importance for many metallurgical processes. The term “melt” refers to molten materials such as metals, salts, slags, etc. For the purposes of this thesis, this term refers only to these liquids and not molten materials such as polymers or any other non-metallurgical liquids. The productivity and efficiency of many high temperature applications rely on accurate knowledge of surface tension, viscosity and density of the melt under consideration.

Density is required in studies ranging from simple mass balance calculations to the study of thermal natural convection phenomena in furnaces. Other examples include predicting the separation of slag/metal systems or calculating the terminal velocity of inclusions submerged within a melt. Density is also required to quantify other physical properties such as surface tension and dynamic viscosity.

Viscosity is a quantity of fundamental importance in fluid transport problems, as well as issues concerning reaction kinetics in melt processing. The viscosity of molten systems often dictates the castability (or ability to fill a mold cavity) of many metals and their alloys [1]. Furthermore, the mechanisms of solidification often depend on the viscosity of the melt [2,3].

Surface tension is significant in terms of the efficiency to which atomization processes operate in the powder metallurgy industry [4]. Of considerable significance is the Marangoni effect, which describes the convection induced within a liquid from a gradient in surface tension. This results, from either concentration or temperature differences at the gas-liquid interface, in surface tension driven flow that can often have

significant implications. An example is welding, where the penetration of the liquid phase depends on the movements of the liquid pool [5]. This is also relevant in steelmaking applications, where the Marangoni effect plays a crucial role in the corrosion of refractory material at slag-gas and slag-metal interfaces. The rate of nitrogen absorption in iron (which impacts the mechanical properties) is also dependent on this phenomenon in steelmaking [6].

These processes exemplifying the fundamental significance of density, viscosity and surface tension are merely a diminutive measure of the vast range of phenomena requiring concise knowledge of these properties. In order to manipulate metallurgical processes, a complete database of information should be available for these properties so that fluid dynamics can be understood. Unfortunately, there is much work that needs to be done in applying property data to many processing environments. For instance, despite years of experimentation, large discrepancies in experimental viscosity values exist for many pure metals such as iron, aluminum, and zinc. This is attributed to the highly reactive nature that many materials exhibit at high temperatures. Contamination issues are thus a continuous source of frustration. In measuring surface tension, this issue becomes monumental since many of the contaminants, in particular oxygen, have a drastic effect on the surface tension of metallic liquids [5,7,8]. Consequently, many of the techniques used in measuring the physical properties of low temperature liquids are not applicable in consideration of these realities. Material selection, temperature control and monitoring, and other such notions place constraints on measurement techniques and modes of operation.

Dealing with melt systems often results in appreciably different fluid dynamic behavior than if low temperature liquids are used. A firmly established concept in comparing low temperature liquids and melt systems is that densities are much larger in metallurgical processes. A less obvious concept is the contribution of surface tension to many high temperature applications. Quantifying the fluid dynamics of melt systems often results in more complex relationships since surface tension is frequently required in the analysis. This study focuses on such a case where surface tension has traditionally been neglected. In the analysis of a liquid draining through an orifice under the influence of gravity, potential and kinetic energies have conventionally been used to predict throughput. Anomalies have been observed in the prediction of flowrate of melts for this system. This is attributed to neglecting the surface tension in an energy balance. Through proper characterization of potential, inertial, viscous as well as surface energy, a more complete model is formulated where the effects of surface tension can be analyzed.

A fortunate aspect of the draining vessel system is that surface tension, viscosity, and density are inherently part of the formulation making it possible to determine all three properties by measuring processing variables. This has statistical advantages over conventional measuring techniques in that conditions change during the course of an experiment making a series of determinations possible. Also, the dynamic nature of the experiments is advantageous over more stagnant conditions since the surface is continuously replenished. Contaminants do not accumulate at the surface under such conditions. Finally, the simultaneous measurement of all three properties using one experimental setup is convenient and unique in comparison with conventional methods.

In Chapter 2, this study will report theory, experimental techniques, and results that establish the current status of knowledge of surface tension, viscosity and density of melts. The challenges in measuring these properties at high temperatures will be emphasized not only in Chapter 2, but Chapter 3 as well, where a description of the experimental apparatus used in this study is presented. Details of measurements at high and low temperatures will be given with information on heat supply, oxygen control, and operational procedure.

Chapters 4 and 5 present the mathematical formulations necessary to determine the physical properties using the new dynamic approach. Validation of the model will be presented in both chapters. Chapter 4 illustrates the characterization of friction through the orifice using the new model. With a rigorous error analysis included, Chapter 5 demonstrates how the surface tension, viscosity, and density can be determined from the formulation presented in Chapter 4.

A discussion of the method applied to systems of molten aluminum and AZ91D alloy is presented in Chapter 6. The highly reactive nature of aluminum and AZ91D alloy with oxygen makes for challenging measurements in this study. By measuring the surface tension, viscosity and density of molten aluminum, it is possible to compare results with data available in the literature and provide a discussion of the merits and limitations of a draining vessel analysis. With measurements of AZ91D alloy (approximately 91%Mg-9%Al-0.5%Zn-0.15%Mn), a valuable contribution is made to the current status of information for commercial alloys. The low density and excellent strength of this material contributes to its success in automotive applications [8]; however, studies of the physical properties of this alloy are lacking. From a fundamental

perspective, it is possible to test theories related to the physical properties of metallic mixtures in consideration of AZ91D.

Finally, conclusions and recommendations will be presented in Chapter 7. Important information from Chapters 2 through 6 will be highlighted and used to generate recommendations for improvements on the technique. Systems of practical importance in process metallurgy will also be considered for future experimentation.

## **CHAPTER 2: LITERATURE REVIEW**

The physical properties of molten metals are fundamental quantities used in understanding many metallurgical processes, as discussed in Chapter 1. Theoretical concepts must be understood in order to gain knowledge from the information available for surface tension, viscosity and density. This chapter will provide theory describing the effects that composition and temperature have on each physical property. A review of the literature on the properties of molten aluminum reveals that issues of oxygen contamination are paramount in making these measurements. Finally, the current methods used to measure surface tension, viscosity, and density will be discussed.

### **2.1 Surface Tension of Molten Metals**

In defining surface tension, it is necessary to analyze fluids on a molecular level, where attractive and repulsive forces dictate the magnitude of cohesion between molecules. Within the bulk of a pure fluid, attractive forces are balanced in all directions. However, when considering the interface between two separate phases, the resultant forces are not of the same magnitude, nor do they uniformly act in the same direction. Refer to Figure 2.1 for an illustration of a gas-liquid interface. An imbalance of the cohesive forces at the surface results in the asymmetric resultant force acting inward to the direction of the bulk liquid.

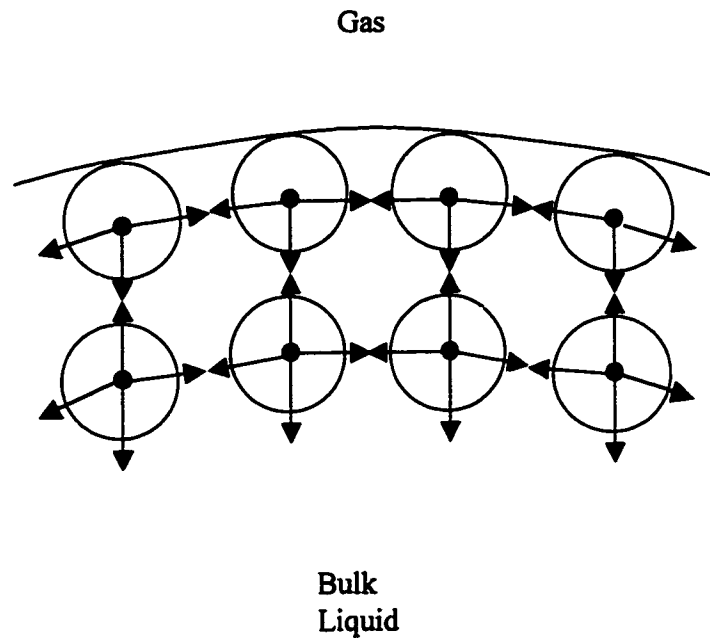


**Figure 2.1: Molecular forces acting at an interface separating a liquid from a gas.**

Referring to Figure 2.2, there exists between pure phases  $\alpha$  and  $\beta$ , a region called the interface region where the concentration of either phase varies and properties change from those characteristics of either phase. If a liquid-gas system is considered, the focus of this thesis, the cohesive forces are much higher in the liquid phase [7]. The *surface tension* can be defined as the property related to the intermolecular forces acting normal to the surface of the gas-liquid interface and has units of Newtons per meter. The surface energy of a liquid-gas system is the product of the surface tension and surface area separating the two phases. The effect of surface energy is to minimize the number of molecules at the surface (i.e. reduce the surface area) [10]. In this study, surface tension will always be referred to as the interfacial tension at a gas-liquid interface only. The



term interfacial tension, however, is used to describe interfacial phenomena between any two phases (e.g. gas-solid, solid-liquid, or gas-liquid).

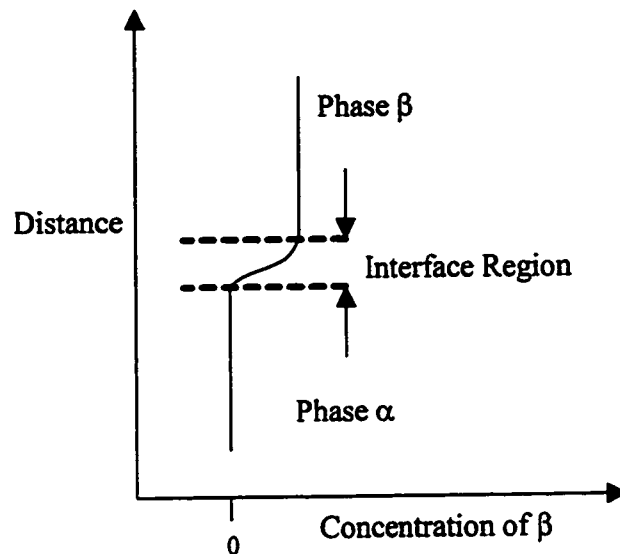


**Figure 2.2: Interface region representing the concentration gradient that exists between phases  $\alpha$  and  $\beta$ .**

In dealing with interfacial phenomenon, it is of interest to note the high magnitude surface energy that molten metals exhibit compared with other fluids. A useful approach to quantifying surface tension is to relate it to other physical properties. This does not condone the determination of surface energy by circumventing experimental techniques. It does, however, provide useful insight into the relative magnitude of surface energy of different fluids, so that the unique characteristics of molten metals can be put into perspective. For example, the heat of vaporization seems to be an indication of surface energy (see Figure 2.3). The surface energy referred to in Figure 2.3 is determined by dividing the surface tension of the liquid by the surface excess concentration that will be derived in Section 2.1.1. From analysis of Figure 2.3, metals clearly have the highest surface energy relative to a wide range of fluids.

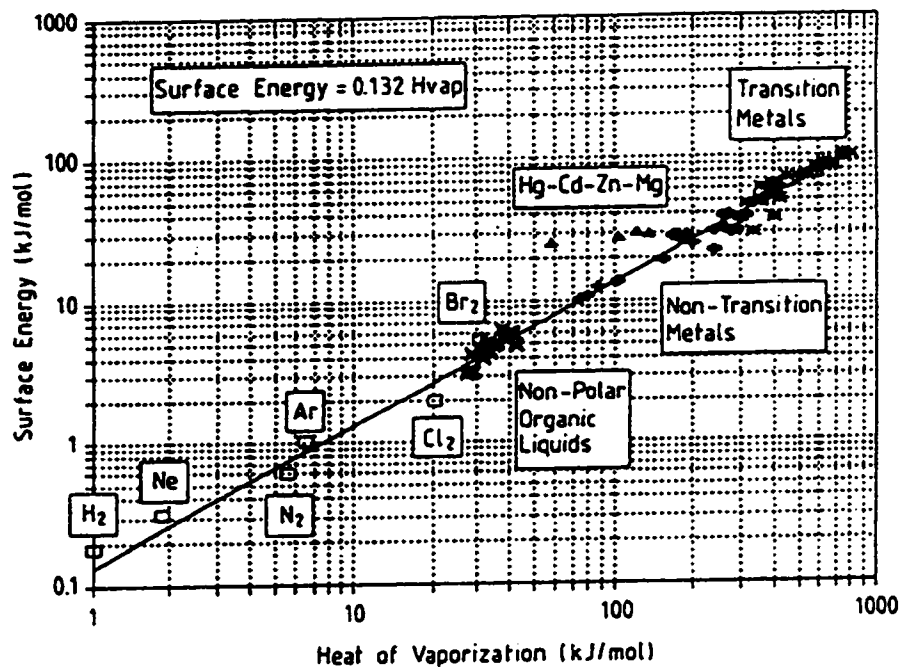


**Figure 2.3: Surface energy for a variety of fluids plotted against the respective heats of vaporization. (From Utigard, T. [10]).**

### 2.1.1 Gibbs Adsorption Equation: Effects of Composition

As explained previously, the surface tension of a particular liquid is a measure of intermolecular forces that are asymmetric in nature at the interface between the liquid and the gas. Often, solutes are “surface active” and preferentially adsorb at the surface, even at low concentrations. The result is a significant decrease in the magnitude of the surface tension because the cohesive forces between molecules at the surface are disrupted with the presence of the solute molecules. This phenomenon is widely observed when considering surface effects of molten metals. Figure 2.4 illustrates the surface tension of aluminum alloys with varying composition of copper, silicon, zinc, tin, antimony,

magnesium and lead. It is clear that elements such as bismuth and lead have a much greater impact on surface tension than other elements.

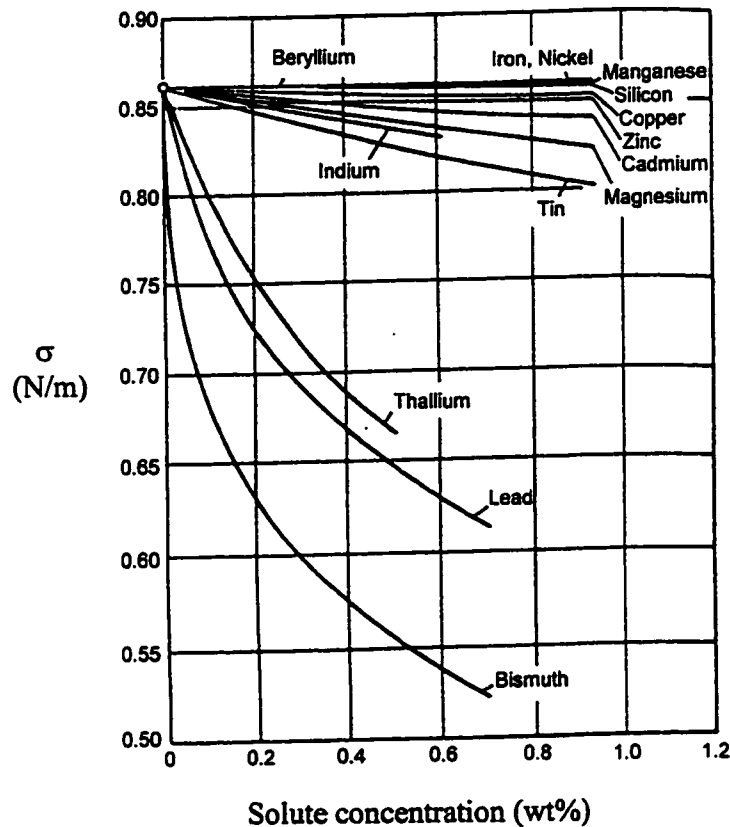


**Figure 2.4: Surface tension of Al-based alloys as functions of alloying composition at 973 K. Atmosphere and oxygen concentration are not specified. (From Lang, G. [11]).**

Interfacial effects can often be greatly affected even by very low levels of impurities. Many impurities drastically affect surface tension, especially oxygen, sulfur, selenium and tellurium [12]. The presence of oxygen is of particular concern in high temperature systems since it is an impurity that is frequently encountered. For a variety of processing conditions, it is difficult to purge atmospheric oxygen from an apparatus to low enough concentrations to avoid surface oxidation. Figures 2.5 and 2.6 illustrate the drastic impact that oxygen has on the surface tension of molten iron and copper,

respectively. The effects of oxygen contamination in aluminum systems have been examined thoroughly in the literature. This will be discussed in detail separately in Section 2.1.5.

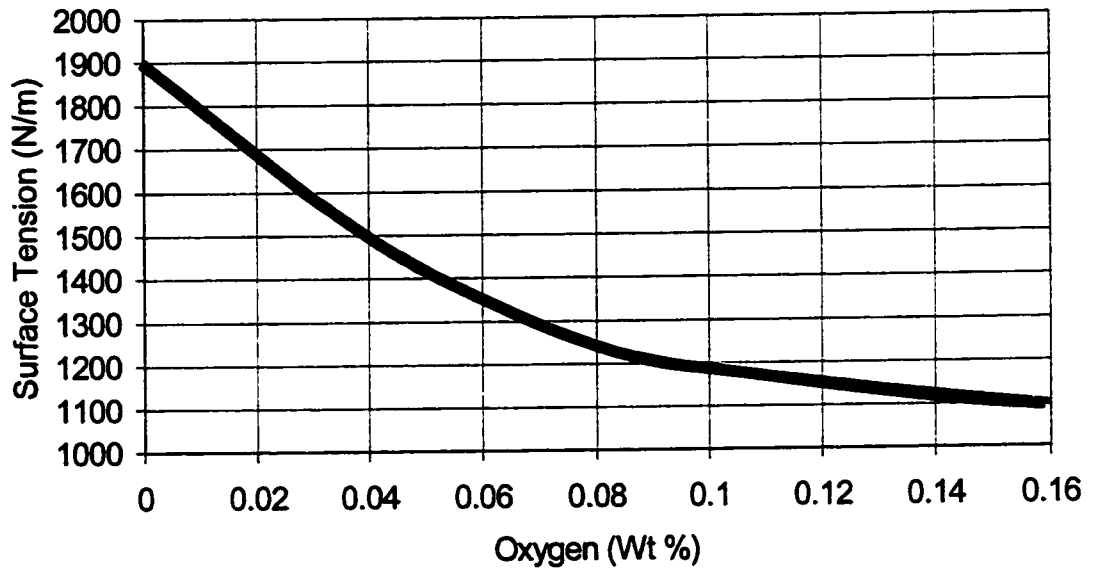


**Figure 2.5: Effect of oxygen present as a solute on the surface tension of molten iron. Temperature and atmosphere are not specified.  
(From Keene, B.J. [7]).**

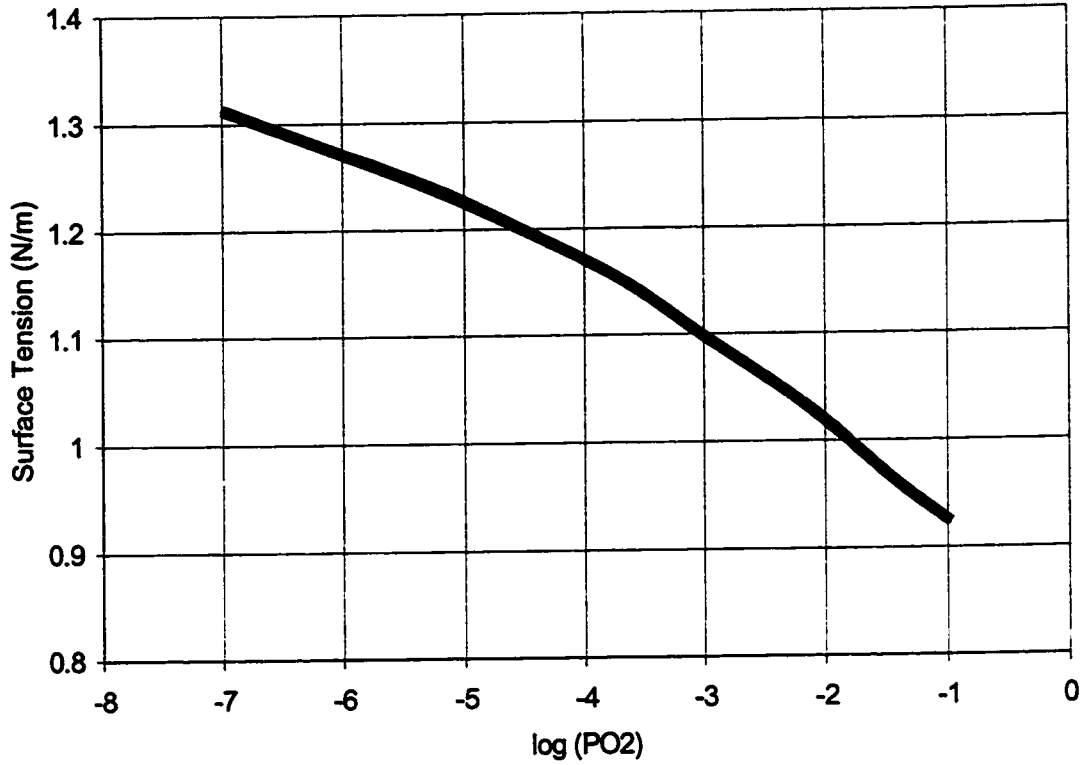


**Figure 2.6: Effect of oxygen present in the gas phase on the surface tension of copper. Temperature and atmosphere are not specified. (From Keene, B.J. [7]).**

To understand how a solute adsorbs at the surface of a liquid, the Gibbs adsorption formulation is used. The presence of an interface introduces an additional term to the function relating the changes in internal energy with changes in volume (V), entropy (S), and molar quantities of species,  $i$  ( $n_i$ ) [5].

$$dU = -PdV + TdS + \sum_i \mu_i dn_i + \sigma dA_r^s \quad (1)$$

where  $A_r^s$  is the area of the interface and  $\sigma$  is the surface tension of the liquid.

The Helmholtz free energy is:

$$F = U - TS \quad (2)$$

The variation in Helmholtz free energy is:

$$dF = dU - TdS - SdT \quad (3)$$

Substituting Equation (1) into Equation (3) yields:

$$dF = -PdV - SdT + \sum_i \mu_i dn_i + \sigma dA_r^s \quad (4)$$

This is a useful relation in understanding the effects of pressure, temperature and solute composition on the free energy of a particular system. When these variables are constant, the thermodynamic definition of surface tension can be stated:

$$\sigma = \left( \frac{\partial F}{\partial A_r^s} \right)_{V, T, n_i} \quad (5)$$

The surface tension of a pure liquid is therefore a measure of the amount of Helmholtz free energy that is necessary to extend a surface by a unit area at constant temperature, volume and composition. In the Gibbs model for surface excess properties, the concentration in the bulk of phase  $\alpha$  is assumed to be constant up to a dividing surface that represents the interface (Figure 2.7). At the dividing surface, the concentration of component  $i$  instantaneously changes to and assumes the concentration in the bulk phase  $\beta$ . The interface region is thus simplified by a distinct dividing surface between phases  $\alpha$  and  $\beta$ . The number of moles of component  $i$  at the dividing surface is determined by using knowledge of the total number of moles and the concentration in phases  $\alpha$  and  $\beta$ :

$$n_i^s = n_{i, total} - n_i^\alpha - n_i^\beta \quad (6)$$

Similarly, the change in free energy at the surface is:

$$dF^s = dF - dF^\alpha - dF^\beta \quad (7)$$

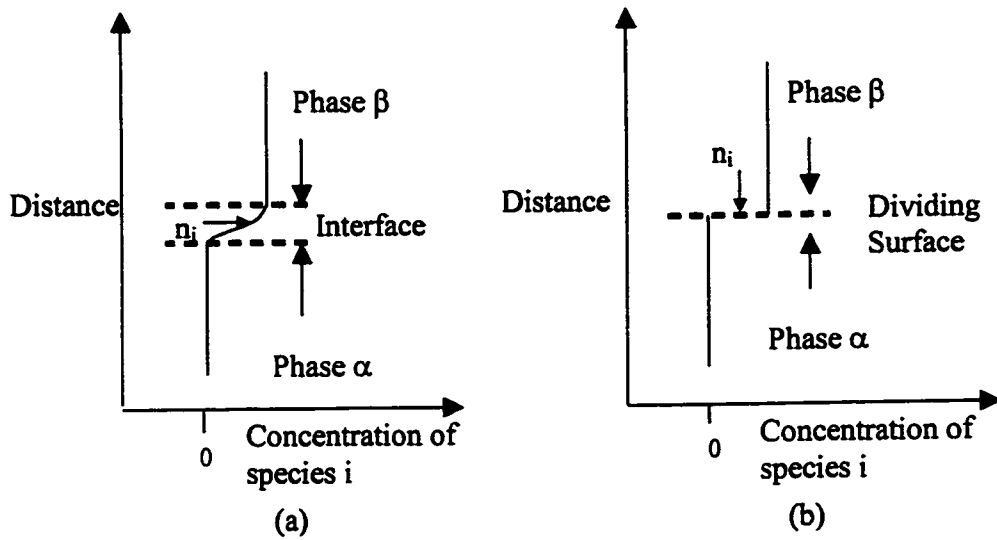


**Figure 2.7: a) Interface region separating phases  $\alpha$  and  $\beta$ . b) Dividing surface used in Gibbs Model approximating the interface region separating phases  $\alpha$  and  $\beta$ .**

Where the change in free energies in the bulk phases are given by:

$$dF^\alpha = -P^\alpha dV^\alpha - S^\alpha dT^\alpha + \sum_i \mu_i^\alpha dn_i^\alpha \quad (8)$$

$$dF^\beta = -P^\beta dV^\beta - S^\beta dT^\beta + \sum_i \mu_i^\beta dn_i^\beta \quad (9)$$

Whether component “ $i$ ” is associated with phase  $\alpha$  or  $\beta$ , its chemical potential is equal in either phase when at equilibrium. Since the entropy of constituent subsystems is additive [13], substituting Equations (4), (8), and (9) into Equation (7) yields the excess free energy of planar interface, for a constant volume and constant temperature system.

$$dF^s = -S^s dT + \sum_i \mu_i dn_i^s + \sigma dA_r^s \quad (10)$$

From Euler’s theorem for a dividing surface and the definition of the Helmholtz function:

$$\sigma = \frac{F^s}{A_r^s} - \sum_i \mu_i \frac{n_i^s}{A_r^s} \quad (11)$$

Differentiating Equation (11) and substituting Equation (10):

$$d\sigma = -\left(\frac{S^s}{A_r^s}\right)dT - \sum_i \frac{n_i^s}{A_r^s}d\mu_i \quad (12)$$

Equation (13) is the Gibbs Adsorption equation:

$$d\sigma = -s^s dT - \sum_i \Gamma_i d\mu_i \quad (13)$$

where  $s^s$  is the surface entropy per unit surface area, and the symbol  $\Gamma_i$  represents the surface excess concentration which has units of moles per unit surface area.

### *Binary Systems*

The significance of  $\Gamma_i$  will now be made clear for binary liquids in contact with a gas. Consider an isothermal binary (i.e.  $s^s dT=0$ ). Equation (13) can be written as:

$$d\sigma = -\Gamma_1 d\mu_1 - \Gamma_2 d\mu_2 \quad (14)$$

Where subscripts 1 and 2 represent the solvent and solute constituents of the binary liquid respectively. The dividing surface can be defined at the point where the surface concentration of the solvent,  $\Gamma_1$  is zero. Equation (14) can now be expressed as:

$$d\sigma = -\Gamma_{2(1)} d\mu_2 \quad (15)$$

$\Gamma_{2(1)}$  is surface excess of component (2) given that the dividing surface was placed at the location where there is no surface excess of component (1). It is theoretically possible to calculate the surface coverage of the solute at the interface. Using Equation (6), and by measuring the concentration of the solute in the liquid and vapor phases, the number of moles of solute at the interface can be determined. The precision required in this determination, as well as practical limitations inherent with molten systems, are such that these computations are rarely carried out.



At constant temperature, the change in chemical potential of species 2 at the interface can be obtained by implementing the activity coefficient of a chemical species in solution,  $\gamma_2$  [14].

$$d\mu_2 = RTd \ln(\gamma_2 x_2) \quad (16)$$

Equation (16) applies at equilibrium when  $\mu_2 = \mu_2^s$ . The mole fraction of the solute in the liquid phase is  $x_2$ . For a dilute solution, the activity coefficient is assumed to be unity. For solutions that are not considered dilute, experimental determination of the activity coefficient is required. Substituting Equation (16) into Equation (15) yields the equation for the adsorption in a binary system at constant temperature.

$$\Gamma_{2(l)} = -\frac{1}{RT} \left( \frac{d\sigma}{d \ln(\gamma_2 x_2)} \right) \quad (17a)$$

For dilute solutions:

$$\Gamma_{2(l)} = -\frac{1}{RT} \left( \frac{d\sigma}{d \ln(x_2)} \right) \quad (17b)$$

A plot of  $\sigma$  vs.  $\ln(x_2)$  provides an analysis where it is possible to determine the effect of concentration of a chemical specie on surface tension due to adsorption at a liquid-gas interface. If an increase in surface tension is observed with increasing concentration, the solute has preferentially transferred to the bulk phase from the surface. A decreasing slope indicates that there is an affinity for molecules in the bulk to adsorb to the surface, typical of a surface active solute [14].

### *Ternary Systems*

The Gibbs adsorption equation can prove to be a useful relation in understanding ternary systems, where interesting interfacial phenomena have been observed. Figure 2.8

illustrates results obtained for iron-carbon-chromium alloys of varying chromium compositions. Equation (13) written for a ternary system at constant temperature such as the one depicted in Figure 2.8:

$$d\sigma = -\Gamma_{2(l)}d\mu_2 - \Gamma_{3(l)}d\mu_3 \quad (18)$$

Similar to the analysis for binary systems, the dividing surface is defined at the position where the surface excess concentration of the solvent is zero. It is not possible to obtain a simple relationship between solute concentration, surface tension and surface coverage, like Equation (17), due to complex interactions between constituents that often take place at the interface. In Figure 2.8, it is clear that the surface tension of a three component system are not additive because of the presence of a minimum at chromium levels between 0.1 and 0.2 atom %. In order to predict this phenomenon, a formulation was presented that makes use of “interaction coefficients” [16]. It is obtained by differentiating Equation (18) with respect to  $\ln(x_2)$  and substituting in Equation (16).

$$-\frac{1}{RT} \left( \frac{d\sigma}{d \ln x_2} \right) = \Gamma_{2(l)} [1 + x_2 \epsilon_2^2] + \Gamma_{3(l)} x_2 \epsilon_3^2 \quad (19)$$

Where  $\epsilon_i^2$  represents the interaction coefficients with respect to component 2, defined as:

$$\epsilon_i^2 = \frac{d \ln(\gamma_i)}{dx_2} \quad (20)$$

Knowledge of activity coefficients is thus a requirement in this formulation. At the minimum, the right hand side of Equation (19) equals zero. Belton [16] used this formulation to predict the concentration of chromium at the minimum. He determined this value to be 0.18 atom fraction, which confirms the minimum observed by Whalen et al. in Figure 2.8.

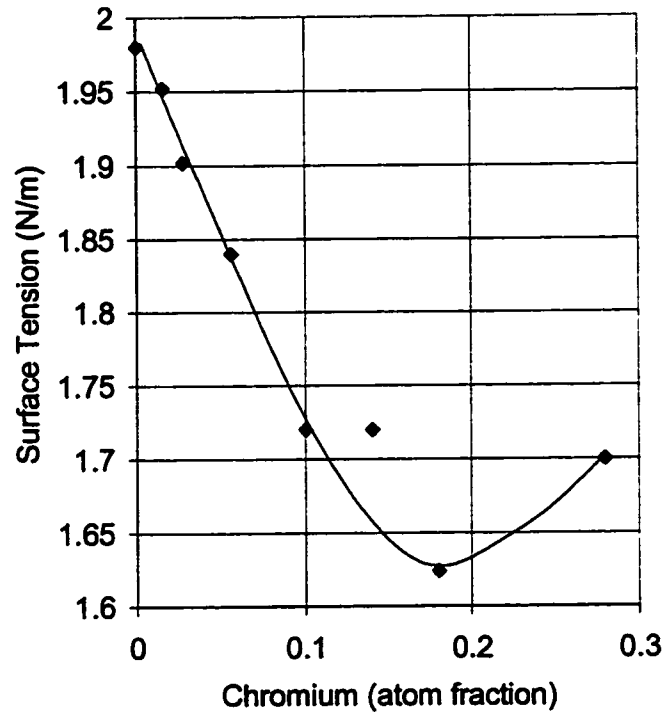


**Figure 2.8: Surface tension of iron-3% carbon alloy with varying concentrations of chromium at 1623 K. Atmosphere and oxygen concentration are not specified. (From Whalen et al. [15]).**

### 2.1.2 Dependence on Temperature

From analysis of the Gibbs Adsorption equation (Equation (13)), the temperature dependence of surface tension for a pure liquid is defined as the entropy per surface area at the interface:

$$\frac{d\sigma}{dT} = -s' \quad (21)$$

It is expected that the magnitude of  $d\sigma/dT$  increases with temperature since entropy increases with temperature. In the literature, however, it is the norm to express the

surface tension as a linear function with temperature [2,7,17]. The linearity is attributed to the fact that measurements are made near the melting temperature relative to the vaporization temperature. Non-linearity is expected as temperature approaches  $T_{\text{vap}}$  since entropy would rapidly increase near vaporization of the melt.

Rearranging equation (21):

$$\int_{\sigma_m}^{\sigma} d\sigma = - \int_{T_m}^T s^s dT \quad (22)$$

Integrating both sides for constant  $s^s$  yields:

$$\sigma = \sigma_m - s^s (T - T_m) \quad (23)$$

where  $\sigma_m$  is the surface tension at the melting point. Substituting Equation (21) into Equation (23) gives the traditional format in which surface tension is expressed as a function of temperature [2,7,17].

$$\sigma = \sigma_m + \frac{d\sigma}{dT} (T - T_m) \quad (24)$$

For a multi-component system, and by applying the Gibbs adsorption equation, the temperature dependence of surface tension is expressed as:

$$\frac{d\sigma}{dT} = - \frac{S^s}{A_r^s} - \sum_{i=2,3,\dots} \Gamma_i \frac{d\mu_i}{dT} \quad (25)$$

For a binary system, and in terms of activity coefficients and molar fractions for constant  $x_2$ :

$$\frac{d\sigma}{dT} = -s' - \Gamma_{2(l)} R \ln(\gamma_2 x_2) \quad (26)$$

Equations (25) and (26) indicate that in multi-component systems, the temperature dependence of surface tension depends not only on the entropy at the surface but also on the activities of the components in the bulk liquid as well. In pure liquids, it is not thermodynamically possible to have the surface tension increase with increasing temperature, as Equation (21) would indicate. In multi-component systems, not only does Equation (26) state that it is thermodynamically possible to have an increase in surface tension with temperature, but it has been confirmed experimentally to occur in some instances. This has been observed with slag melts with high levels of  $\text{SiO}_2$  in which large complex molecular structures are formed. As temperature is increased, these structures dissociate producing an increasing number of broken molecular bonds. The increasing number of unsatisfied bonds increases the free energy at the surface, resulting in an increase in surface tension [7]. Figure 2.9 illustrates the temperature dependence of a silver based alloy with varying lead composition. This phenomenon is attributed to strong surface segregation as temperature is increased [5].

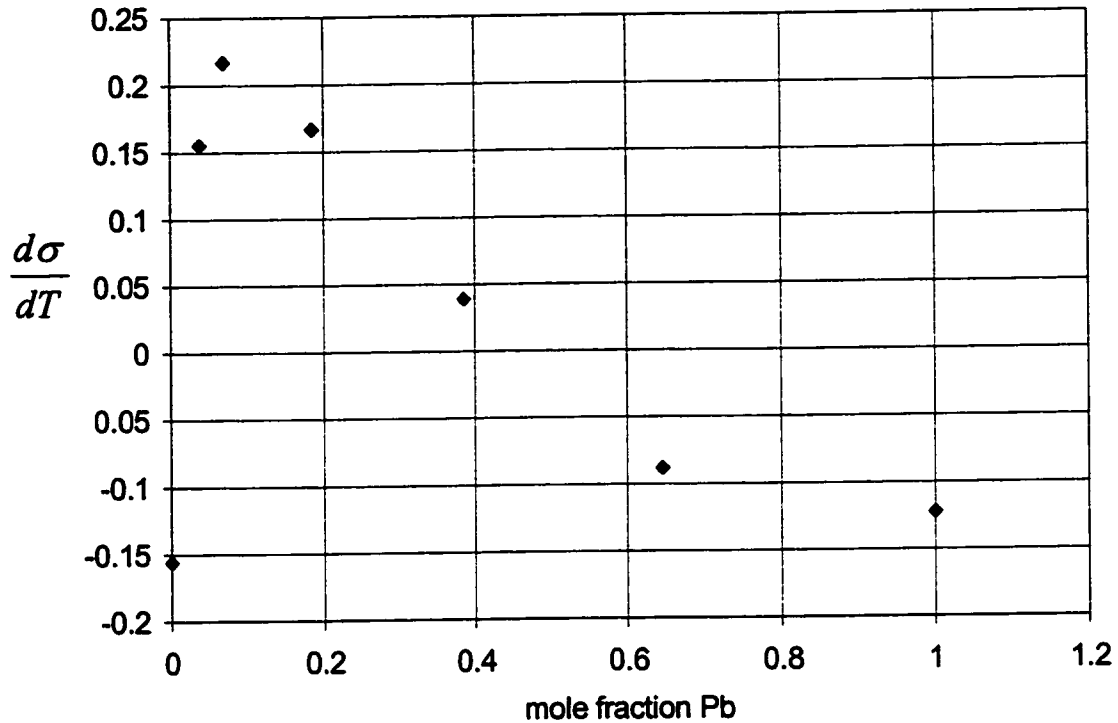


**Figure 2.9: Temperature dependence of surface tension as a function of lead concentration exhibiting positive values for  $d\sigma/dT$ . Temperature, atmosphere, oxygen concentration not specified. (From Joud and Passerone, [5]).**

### 2.1.3 Dynamic Surface Tension

For liquids in general, measuring the surface tension in the presence of surface active substances requires that mass transfer and kinetic issues be considered. When an interface between a liquid and gas is created, surface tension varies from its initial or pure value ( $\sigma_0$ ) to its equilibrium value ( $\sigma_e$ ) in the presence of surface active substances. The time it takes for this to occur varies from approximately  $10^{-6}$ s to hours or days, depending on the system under consideration [29]. For molten metals, the characteristic times for

the surface to reach a saturated state with oxygen (indicating equilibrium condition) have been predicted. This is accomplished through consideration of Knudsen diffusion and imposing saturation values of oxygen pressure [40]. Figure 2.10 illustrates the time required for melts to reach oxide saturation at oxygen pressures of 1Pa (in a vacuum). By definition, the “pure dynamic surface tension” is that measured at the instant of formation of a new surface [5]. In this thesis, the term “pure dynamic surface tension” will refer to this definition. The term “dynamic surface tension” will refer to the surface tension of the liquid at any instant before equilibrium is established. This is an experimentally challenging quantity to determine. Typically, equilibrium surface tension is quoted in the literature with very little experimental studies done on the dynamic surface tension of molten metals. Ricci et al. [40] performed a study on liquid tin. The review of the results is beyond the scope of this study; however it was determined that surface oxidation depends on the dynamics of metal and oxide vapor exchange at various partial pressures. Also, it was determined that the response of surface oxidation depends on the gradient of temperature with time. More relevant to this discussion is the experimental apparatus Ricci et al. used [40]. The sessile drop technique (explained in the next section) was used in this experiment, which implemented an “ion-gun” that removed any oxides formed on the drop prior to taking measurements. The response time of the experimental set-up ranges from 0.5s to hours making it an especially practical procedure for analyzing the response of molten systems to kinetic and mass transfer issues. The observable times that the apparatus could accommodate are within the dotted lines indicated in Figure 2.10. The precise observation times are not stated [40].

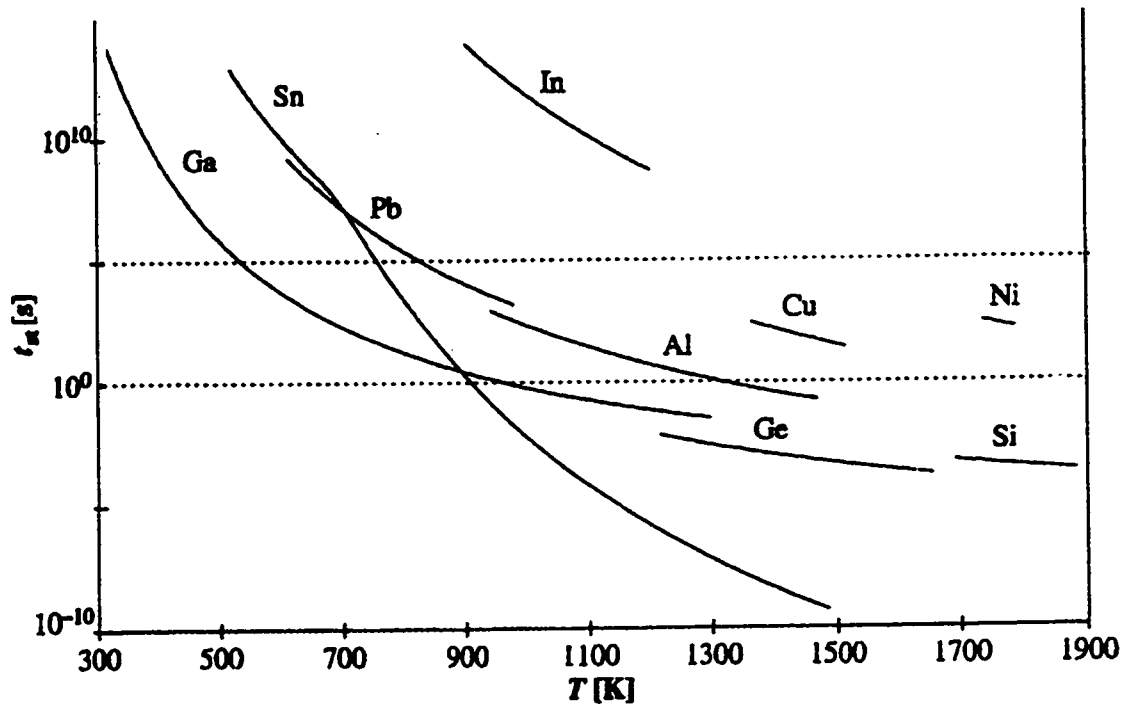


**Figure 2.10: Characteristic times of a 0.01m diameter droplet to be saturated with oxide at a total pressure of oxygen of 1Pa, for various metallic systems (From Ricci et al. [40]).**

#### 2.1.4 Techniques to Measure Surface Tension

Techniques used to measure the surface tension of a liquid are based on a force balance in which surface tension plays a significant role. Again, for reasons of clarity, the term surface tension refers to gas-liquid interfaces only. Most methods rely, in some form, on the Laplace equation that relates the excess pressure ( $\Delta P$ ) at a curved interface with the radii of curvature ( $R_1$  and  $R_2$ ) at a point on the surface:



$$\Delta P = \sigma \left( \frac{1}{R_1} + \frac{1}{R_2} \right) \quad (27)$$

Analysis of Equation (27) indicates that:

For a spherical surface ( $R_1=R_2=R$ ):  $\Delta P = 2\sigma/R$ ;

For a cylindrical surface ( $R_1=R$ ;  $R_2=\infty$ ):  $\Delta P = \sigma/R$ ;

For a planar surface ( $R_1=R_2=\infty$ ):  $\Delta P = 0$ .

The Bond number is a non-dimensional number used to determine the magnitude of the surface forces relative to the potential forces in a particular system. The potential force often will take the form of gravity such as the weight of a droplet resting on a surface or the weight of a droplet suspended from a capillary. The techniques outlined in this section will outline similar potential forces. The form of the Bond number may vary, but it always follows this convention:

$$B_o = \frac{\text{Potential Force}}{\text{Surface Forces}} \quad (28)$$

When the Bond number is small, indicating substantial surface forces, it is often possible to measure surface tension by properly quantifying relevant experimental variables. For most surface tension measurement techniques, a curved interface is usually present with a small radius of curvature resulting in a significant pressure difference according to the Laplace equation. The sessile and pendant drop methods; drop weight, maximum bubble pressure, capillary rise, and detachment techniques all rely on these principles. Exceptions in the following discussion are the vibrating jet and levitating drop techniques that use the principles developed by Raleigh [41]. These approaches involve the influence of surface tension on the instabilities inherent to oscillations on a liquid surface.

## *Shape Methods: Sessile and Pendant Drop Techniques*

### *Sessile Drop (SD):*

This technique uses the dimensions of a stationary droplet resting on a horizontal surface. The resting drop assumes a shape in which a balance of gravitational forces and surface forces is achieved. The Laplace equation is used, but due to the gravitational environment of the droplet, a complex form is required to describe the surface dimensions. Bashworth and Adams [42] determined that the surface tension is related to the dimensions of the droplet as follows:

$$\sigma = \frac{g\rho q^2}{j} \quad (29)$$

Where  $q$  and  $j$  are parameters determined from Bashforth and Adams tables [42] using the measured values of  $X$  and  $Z$  illustrated in Figure 2.11.

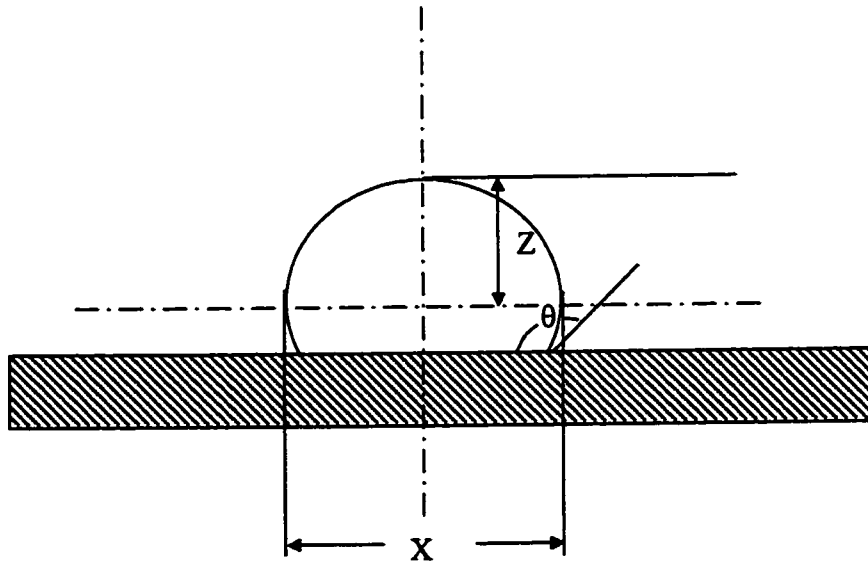


**Figure 2.11: Dimensions of sessile droplet required for calculation using the analysis approach of Bashford and Adams [42].**

This technique facilitates another analysis, which is described by Young's equation to obtain the difference in interfacial tension between the gas-substrate,  $\lambda_{GS}$ , and liquid-substrate,  $\lambda_{LS}$ , using the gas-liquid surface tension,  $\sigma$ , and contact angle,  $\theta$ . Young's equation is defined as:

$$\lambda_{GS} = \lambda_{LS} + \sigma \cos \theta \quad (30)$$

The surface tension is obtained from Equation (29) and substituted into Equation (30).

Note that in the SD technique, only one measurement of  $\sigma$  and  $\theta$  is made per droplet.

*Pendant Drop (PD):*

Similar to the sessile droplet, the pendant droplet technique makes use of the gravitational and surface forces that are in equilibrium, except that the droplet is hanging from the end of a capillary tube. Shape factors are also required to describe the surface of the droplet. Refer to Figure 2.12.

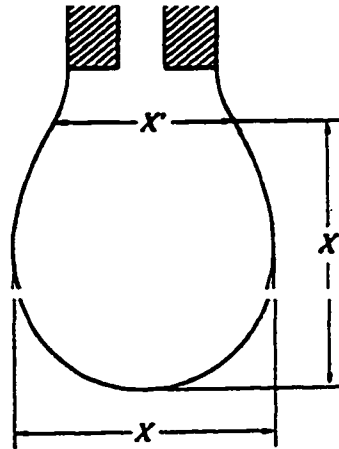


**Figure 2.12: Dimensions of pendant droplet required for calculation using formulation by Andreas et al. [43]. (From Iida and Guthrie, [2]).**

A relationship involving the dimensions of the pendant droplet ( $X/X'$ ), and a set of tables used to determine yet another shape factor ( $y$ ) was proposed by Andreas et al. [43]:

$$\sigma = \frac{\rho g X^2}{y} \quad (31)$$

Both the sessile and pendant drop techniques described above rely on numerical solutions that take the form of shape factors presented in tables. Consequently, there is truncation error associated with the calculations for surface tension. In recent years, however, computerized numerical calculations, enhanced photographic resolution, and effective image analysis techniques have yielded improved accuracy of results. Even with these improvements, many errors associated with these techniques still exist. Camera-monitor distortion, discretization of the surface profile, and evaluation of the system magnification factor (in deriving real drop profile from photograph) all contribute to error in measurements. In order to obtain the magnitude of error, the effect of each source of error must be understood and quantified. Consequently, there are different sources of errors expected depending on the apparatus that is used. When dealing with liquid metals, both techniques are also particularly vulnerable to contamination with the environment since a small quantity of liquid metal is used in a stagnant situation with the surrounding atmosphere. The pendant drop method is not a suitable technique to determine temperature variations. This is because there is a relatively small contact surface between the droplet and the capillary, making it difficult to maintain the droplet's temperature. The capillary is heated to the desired temperature; however, there may be significant temperature gradients between the capillary tip and various areas on the

droplet surface. Similar to the SD technique, the PD method will only provide one measurement per droplet.

*Drop Weight (DW):*

The basis of this technique utilizes the maximum weight a droplet achieves, forming from the tip of a capillary, before detachment takes place due to the influence of gravity. Under ideal circumstances, the gravitational force acting on the droplet at the point of detachment is equal the surface force, and is given mathematically by:

$$m_d g = 2\pi r_{cap} \sigma \quad (32)$$

where,  $m_d$  is the mass of the droplet and  $r_{cap}$  is the radius of the capillary. In reality, however, it has been determined that the formation of the droplet is not as trivial as Equation (32) suggests. Typically, as the drop grows, the neck of liquid connected to the capillary elongates and premature detachment ensues. This often results in liquid that is still attached to the capillary that may even result in the formation of satellite droplets [7]. Harkins and Brown [44] produced tables of factors that relate the real and ideal droplet weights. A slightly modified form of Equation (32) is:

$$m_d g = 2\pi r_{cap} \sigma \hat{w} \quad (33)$$

The factor,  $\hat{w}$  has been determined from calibrations with low temperature fluids such as water and other organic fluids. It has not yet been established if these factors can be used for liquid metals. Since there is a small contact area between the heated capillary and the rest of the droplet, significant temperature gradients are expected making this method an undesirable technique if the effect of temperature is of concern.

### *Maximum Bubble Pressure (MBP):*

The maximum bubble pressure technique utilizes the maximum pressure within a bubble that is formed before detachment from a capillary tube that is submerged at a given location within a liquid. The maximum pressure is the summation of the static pressure of the liquid at a depth,  $h$ , and the surface pressure induced due to the curved surface of the capillary,  $P_\sigma$ , defined by  $r_{cap}$ .

$$P_{Max} = P_\sigma + \rho gh = \frac{2\sigma}{r_{cap}} + \rho gh \quad (34)$$

The density  $\rho$ , is the difference between densities of the liquid and gas and is approximately equal to the density of the liquid. When  $P_{max}$  is plotted versus  $h$ , the slope will yield the density and the y-intercept will produce the surface tension of the liquid. Equation (34) represents an ideal situation where it assumed that the contours of the menisci are spherical. However in many situations involving larger capillaries, and due to gravitational effects, this assumption is rendered invalid. Schrödinger [45] formulated a modified version of equation (34), which addresses this issue:

$$\sigma = \frac{(P_{Max} - \rho gh)r_{cap}}{2} \left[ 1 - \frac{2}{3} \left( \frac{r_{cap} \rho g}{(P_{Max} - \rho gh)} \right) - \frac{1}{6} \left( \frac{r_{cap} \rho g}{(P_{Max} - \rho gh)} \right)^2 10^{-6} \right] \quad (35)$$

MBP is an effective technique in determining the temperature dependence of surface tension since the equipment easily facilitates the use of thermocouples. Also, a fresh surface is created within the liquid, meaning that contamination due to the surroundings is only possible through the introduction of impurities present in the inert bubbling gas. Since gas suppliers can only guarantee a certain purity level in their product, there is always a trace level of oxygen present that is expected to impact the surface tension

measurement. This will be discussed in detail in Section 2.1.5. It is important when using MBP that the “true” radius of the capillary is considered. This refers to cases when the liquid wets the capillary resulting in spreading of the liquid to the outer radius of the tip. This would result in a significant systematic error. There have been instances published in the literature where erroneous data was presented due to this phenomenon [46]. Due to the fact that the bubble is submerged in the melt, it is not possible to make visual observations of the bubble generation. Abnormalities cannot be pinpointed in the experimental method via visual means because of this factor.

#### *Detachment Methods:*

This class of techniques is based on measurement of the maximum force that is exerted by a body as it is pulled from the surface of a liquid. The body may be a ring, plate, etc. The force that is required to detach from the surface is directly a function of the surface forces exhibited by the liquid. These techniques are also referred to as “tensiometric methods”. The equation used for a ring-shape body is the following [47]:

$$\sigma = \left( \frac{F_o}{4\pi r_r} \right) l \quad (36)$$

Where,  $F_o$  is the force required detaching the ring from the surface of the liquid,  $r_r$  is the radius of the ring and  $l$  is a correction factor that is related to the shape of the menisci, which is determined through calibration using a liquid of known surface tension. This technique is limited to liquids that exhibit very good wetting behavior.

#### *Capillary Rise (CP):*

A relationship used to calculate surface tension is based on the analysis of the capillary rise of a liquid through a narrow tube. This technique has been used extensively for organic liquids, but for practical reasons, it has rarely been used for molten metals [7].

When a capillary tube is immersed in a liquid, the level will rise in the tube to a height,  $h_{cap}$ , due to capillary action of the fluid. Refer to Figure 2.13. For a meniscus of a spherical profile:

$$\frac{2\sigma}{R} = h_{cap} g \rho \quad (37)$$

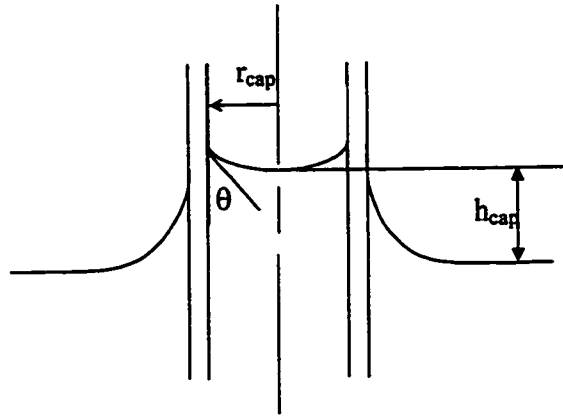


**Figure 2.13: Capillary rise method for determining the surface tension of a liquid.**

The radius of curvature,  $R$ , is related to the contact angle and the radius of the capillary,  $r_{cap}$ , by  $R = r_{cap} / \cos \theta$ . Equation (37) can be expressed as a function of contact angle as:

$$\sigma = \left( \frac{h_{cap} g \rho r_{cap}}{2 \cos \theta} \right) \quad (38)$$

#### *Vibrating Jet Method (VJ):*

It is possible to determine the surface tension of a liquid flowing out of an elliptical orifice. This orifice geometry results in oscillations on the liquid jet that continue on the surface until they are dampened out due to viscous dissipation. The formulation of the method is beyond the scope of this discussion; however, it was



determined that the surface tension is related to the frequency of oscillations. The surface tension acts as a restoring force, meaning that low surface tension results in relatively low frequency oscillations and long wavelengths. A series of measurements may be taken on the surface of the jet that corresponding to the length of time the surface is exposed to the atmosphere. This facilitates time dependant surface tension calculations since the distance from the orifice may vary (refer to Section 2.1.3). Physically unrealistic surface tensions are usually obtained from the first few wavelengths using this technique [39]. Because of the large surface tension of liquid metals, break-up of the jet usually occurs very close to the orifice plate due to the disruptions on the liquid surface under these circumstances. The vibrating jet technique is, therefore, considered not to be an option for molten metal systems.

*Levitating Droplet (LD):*

A relatively recent method for measuring surface tension, a levitating droplet makes use of an electro-magnetic field induced by an induction coil. Approximately 0.5g of an electrically conducting material is placed in the electromagnetic field where it levitates and melts. The resultant droplet oscillates due to perturbations inherent in the system and the frequency,  $\omega$ , is measured. Using the Raleigh equation [41]:

$$\sigma = \frac{3}{8} \pi m \omega^2 \quad (39)$$

Where, m is the mass of the sample. This technique is attractive from the point of view that there is no contact between the droplet and any materials in the apparatus eliminating contamination via that route. However, the atmosphere must be of sufficient purity to ensure that the sample is as clean as possible. Since such a small quantity of sample is used and it is the only hot object in the apparatus, it is particularly vulnerable to

contaminants in the atmosphere. Because electrical conductivity is a requirement for materials subjected to LD, it is confined only to metallic systems. Finally, it is difficult to obtain the temperature of the sample since it is not possible to insert thermocouples. Pyrometric methods can be used; however, sufficiently high temperature must be used such that emissivity data, if available, can be applicable.

### *Considerations For Molten Metals*

Of all the methods that are introduced in this chapter, the sessile drop and maximum bubble pressure method are most frequently used for measuring surface tension of high temperature liquids such as molten metals [2]. Practical issues such as temperature control and measurement, and implications involving equipment design are among the reasons why SD and MBP are typically used. The sessile drop technique is used because it is experimentally simple and it is possible to maintain good temperature control. Contamination issues, however, are at the forefront of limitations when applying SD. The maximum bubble pressure technique is an attractive alternative from the point of view of surface contamination. A fresh surface is created, submerged in the liquid and is not in contact with the atmosphere surrounding the liquid. The main source of contamination is from the bubbling gas that must be of sufficient purity. As mentioned previously, it is not possible to make visual observations of the bubbling process since the capillary is submerged in the melt. It is also important that the pressure transducer used in determining the pressure within the bubble is calibrated and making correct measurements. However, fast bubbling rates can be applied so that under certain circumstances, measurements can be made before the surface is completely oxidized. This facilitates measurements that approach the “pure dynamic surface tension”. Recall

from Section 2.1.3 that this term represents the surface tension at the moment a fresh surface is created. However, under the best conditions for any liquid, the response time for MBP is typically 0.1s to minutes [39]. Given the highly reactive environment at high temperatures, obtaining the “pure dynamic surface tension” is not possible using conventional methods.

### 2.1.5 Experimental Data

As alluded to in Section 2.1.1 and 2.1.4, measuring the surface tension of a pure liquid metal is difficult due to the presence of oxygen that tends to act as a highly surface active contaminant in most circumstances. It is often difficult to obtain experimentally, the surface tension of a “pure” liquid metal since it is extremely difficult to remove all the oxygen from a particular system. The surface tension measurements of molten metals are done in a vacuum or within an inert atmosphere to ensure that oxygen is kept at a minimum. The quality of the equipment, and the measures taken for oxygen removal vary for different sources of data. Keene [7], in a recent review of the surface tension of pure metals proposed a relationship for surface tension of molten aluminum as a function of temperature. It takes the following form:

$$\sigma_{Al} = 0.871 - 0.155(T - T_m) \text{ (N/m)} \quad (40)$$

Where  $T_m$  is the melting temperature (for aluminum,  $T_m = 933\text{K}$  ( $660^\circ\text{C}$ )), and  $\sigma_m = 0.871 \text{ N/m}$  is the surface tension at the melting point. This relationship is based on an

average of a series of functions that have been proposed in the literature [10,17-34]. Table 2.1 summarizes a number of sources and the conditions and methods of measurements that were utilized.

**Table 2.1: Surface tension of aluminum quoted from a variety of sources. The temperature coefficient, atmosphere and purity are included. SD: Sessile Drop. MBP: Maximum Bubble Pressure.**

Authors	Yr	Method	Atmosphere	Purity (%)	$\sigma_{Al(M)}$ (N/m)	$d\sigma/dT$ (N/mK)
Levin et al. [15]	1968	SD	Helium	99.99-99.996	0.865	$-0.15 \times 10^{-3}$
Vatolin et al. [30]	1969	SD	Helium	99.999	0.873	$-0.15 \times 10^{-3}$
Yatsenko et al. [25]	1972	SD	Vacuum	99.999	0.865	$-0.16 \times 10^{-3}$
Lang [29]	1974	MBP	Ar	99.999	0.868	$-0.152 \times 10^{-3}$
Gourimi et al. [14]	1979	SD	Vacuum	99.999	0.865	$-0.15 \times 10^{-3}$
Pamies et al. [31]	1984	MBP	Ar	99.999	0.873	$-0.12 \times 10^{-3}$

In his review, Keene also acknowledged the fact that the data used to generate this relationship are based on measurements in which a certain degree of oxidation is expected. Levin et al. [19] performed a series of experiments and generated data that were in reasonable agreement with other sources. The purity of the aluminum he used was greater than 99.99 %. As well, he implemented titanium getters to remove residual oxygen from the helium atmosphere. As part of the analysis, Levin et al. purposely contaminated a series of the aluminum tests by re-melting the material in air prior to experimentation, consequently increasing the amount of  $Al_2O_3$  in the system. Figure 2.14 illustrates the results that clearly indicate an increase of oxygen contamination has a significant impact on the magnitude of surface tension. The linear relationship is the

recommended function presented by Levin et al. in Table 2.1 and represents the uncontaminated results.

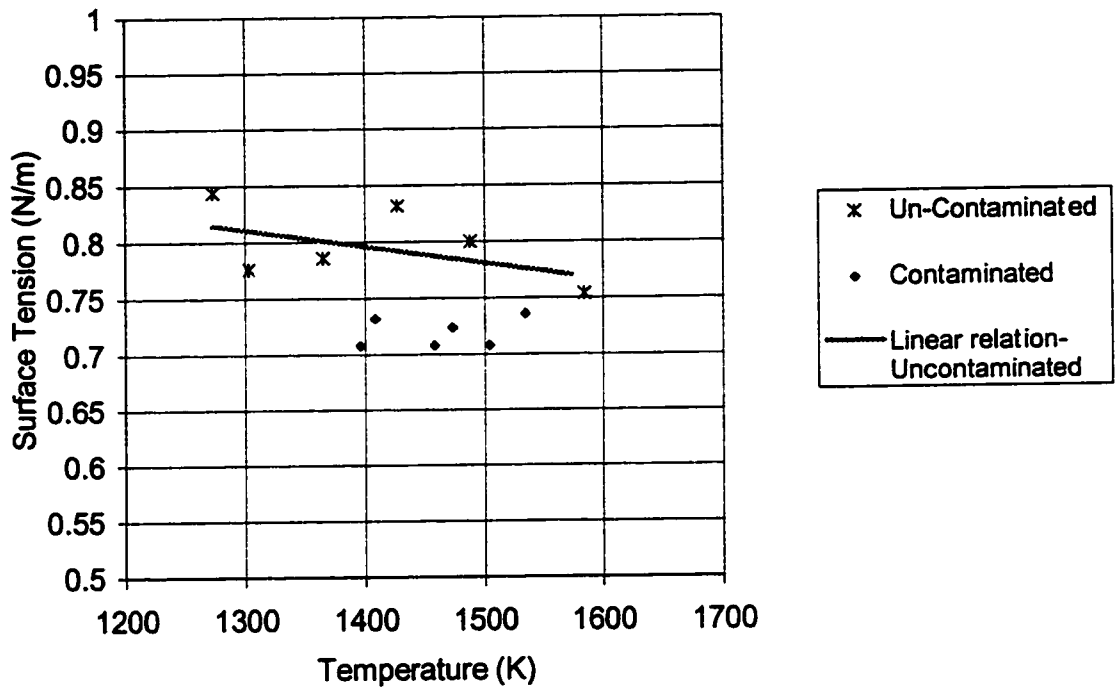
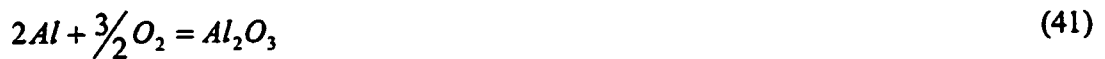


**Figure 2.14: Surface tension of high purity aluminum, and aluminum deliberately contaminated with oxygen (From Levin et al. [19]).**

In studying the effects of surface oxidation for an aluminum-based system, chemical equilibrium between aluminum, oxygen, and aluminum oxide must be considered [8]:



The ratio of the surface activities of  $Al_2O_3$  and Al depend on the partial pressure of oxygen as follows:

$$K_e P(O_2)^{2/3} = \frac{\gamma_{Al_2O_3} x_{Al_2O_3}}{(\gamma_{Al} x_{Al})^2} \quad (42)$$

The equilibrium constant for the formation of  $\text{Al}_2\text{O}_3$  is  $1.23 \times 10^{71}$  at 1000K (723°C) [36]. The magnitude of this number dictates that the reaction will proceed even under exceptionally low oxygen partial pressures. An oxygen pressure of less than  $10^{-44}$  atm is needed to avoid oxidation [38]. From a practical point of view it is very difficult to reach low enough pressures to avoid oxidation. Kaptay [8] proposed that the surface of aluminum in the presence of the oxide layer is, at relatively low temperatures, in a state of super-cooled  $\text{Al}_2\text{O}_3$ . This concept is illustrated in Figure 2.15, where it is suggested that:

$$\sigma(\text{Al, Oxidized}, T) \approx \sigma(\text{Al}_2\text{O}_3, T) \quad (43)$$

The temperature being referred to is the melting point of  $\text{Al}_2\text{O}_3$ .

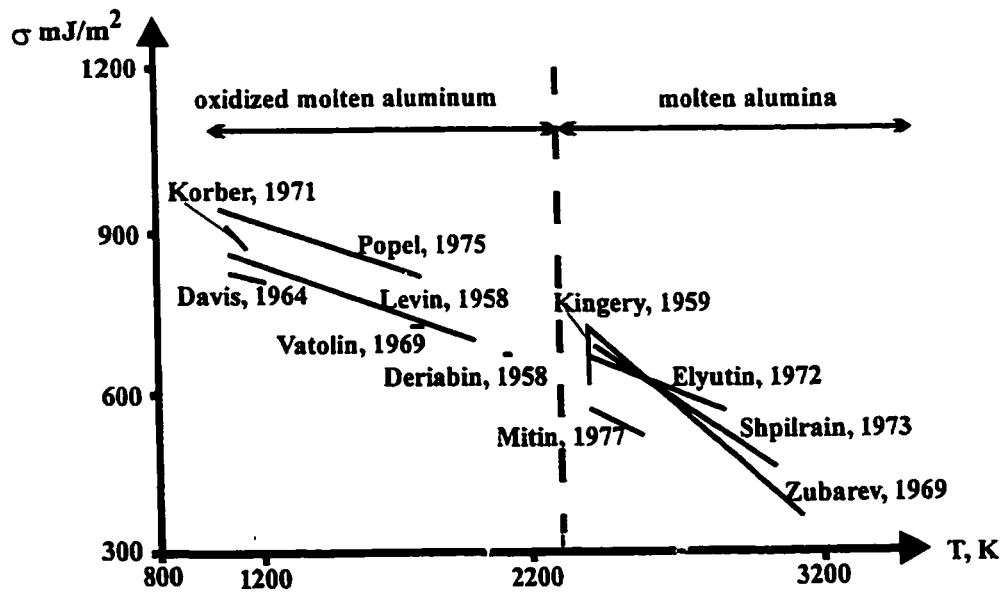


**Figure 2.15: Surface tension of aluminum and alumina as a function of temperature, quoted from a variety of sources (From Kaptay [8]).**

In the 1980's, insight into the surface tension of "pure" aluminum was obtained both theoretically and experimentally. Chacón et al. [37] theoretically calculated the surface tension of pure aluminum to be 1.184 N/m. Previous to this calculation, Gourimi and Joud [32] also published experimental results that indicate that the surface tension of pure aluminum is indeed significantly higher than what has published in the literature.

Gourimiri and Joud used the sessile drop method to determine the surface tension of "pure" liquid aluminum. The extraordinary measures taken in this study to clean the aluminum of oxygen contamination consisted of a combination of heating and ion bombardment of the surface. Using Scanning Auger electron spectroscopy (AES), the surface concentration of oxide on the surface of aluminum-tin alloys was determined. The principle behind this technique is the detection of emission of secondary electrons from a specimen after the surface has been excited with electrons. This acts as a fingerprint of the chemical species on the surface of a specimen. The technique is operated at very low pressures ( $<1.0 \times 10^{-7}$  Pa), but allows for the incident beam to move from one specimen surface region to another for mapping of the elemental distribution on the surface. The experimental results from this study are presented in Figure 2.16. Goumiri and Joud have expressed the surface coverage of  $\text{Al}_2\text{O}_3$  in terms of monolayer units. When  $X = 1$ , the surface is considered to be covered by one layer of  $\text{Al}_2\text{O}_3$  molecules. It is clear from Figure 2.16 that the surface tension of aluminum decreases rapidly at initial oxidation levels and much slower at concentrations greater than one monolayer. It is reasonable to say that because of these results, the surface tension quoted from various sources prior to this study correspond to "oxidized aluminum". It is proposed for low surface coverage ( $X < 0.3$ ), that oxide "islands" are present [8]. As the

oxide coverage increases ( $X > 0.5$ ), the islands form a network that holds the specimen together, which results in surface tension measurements that are more closely related to the values of super-cooled  $\text{Al}_2\text{O}_3$  [8]. Refer to Figure 2.17.

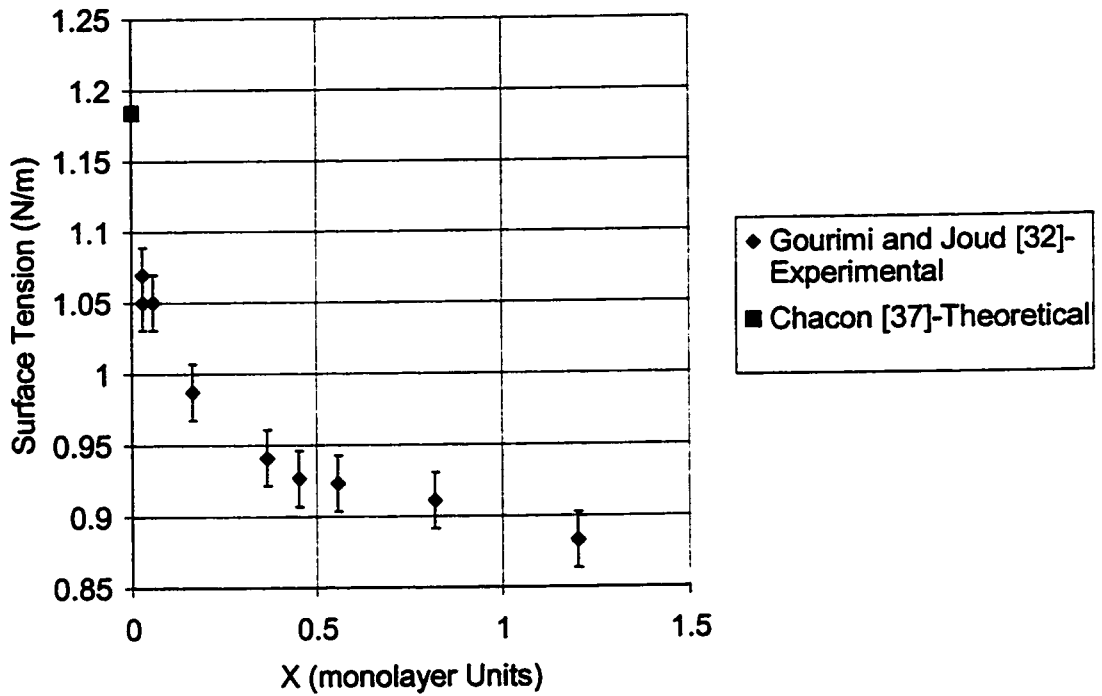


**Figure 2.16: Surface tension dependence on the coverage of  $\text{Al}_2\text{O}_3$  of pure aluminum determined experimentally [32], and theoretically [37] at  $973^\circ\text{C}$ .**

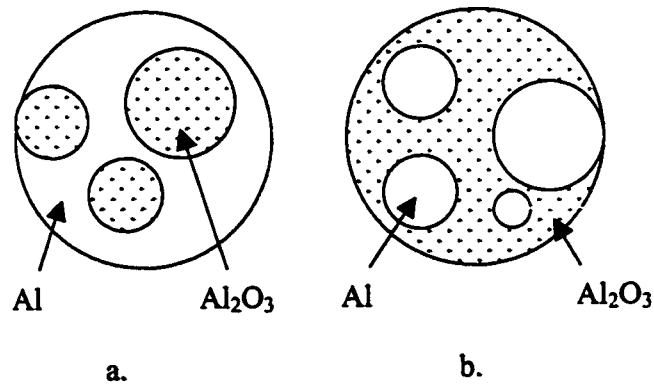


**Figure 2.17: Surface of aluminum subjected to coverage of  $\text{Al}_2\text{O}_3$ : a)  $X < 0.3$ ; b)  $X > 0.5$ .**



Referring to Table 2.2, the surface tension of aluminum and magnesium is available in a number of reference books [2,17]. These sources incorporate the data that was obtained from Allen [57]. The method used by Allen in determining the surface tension of aluminum and magnesium is not specified in these references. Keene's thorough review of the surface tension of pure metals is considered to be an excellent source for the surface tension of pure metals. This is because the relation is based on the average of a series of measurements made by a variety of researchers. Of the 20 sources referenced by Keene [10,17-34] for aluminum, 8 used MBP and 12 used SD. For the magnesium relationship, 5 sources are referenced, including 3 MBP determinations, 1 SD determination and 1 for which the method is not specified. Table 2.2 also includes the surface tension of un-oxidized aluminum obtained from Gourmiri and Joud [32] that was determined using SD.

**Table 2.2: Surface tensions of aluminum and magnesium from sources in the literature [2,7,17,32].**

Source	Material	Surface tension at melting point, $\sigma_m$ (N/m)	Temperature dependence of surface tension, $d\sigma/dT$ ( $Nm^{-1}K^{-1}$ )
1. <u>Physical Properties of Liquid Metals</u> [2], 1988; 2. <u>Smithells Metals Reference Book</u> [17], 1998	Aluminum	0.914	$-0.35 \times 10^{-3}$
	Magnesium	0.559	$-0.35 \times 10^{-3}$
Keene [7], 1996	Aluminum	0.871	$-0.155 \times 10^{-3}$
	Magnesium	0.577	$-0.26 \times 10^{-3}$
Gormiri and Joud [32], 1982 (un-oxidized aluminum)	Aluminum	1.050	N/A
	Magnesium	N/A	N/A

Recall  $\sigma = \sigma_m + d\sigma/dT(T - T_m)$

When discussing results for AZ91D alloy in Chapter 6, knowledge of the physical properties should be available to provide a complete analysis of the data. Unfortunately data were only found for surface tension. Regrettably, the data was only relevant at 1023 K. The surface tension of Mg-Al-Zn-Mn alloys at 1023 K is summarized in Table 2.3. The source is from Patrov et al. [58], who summarized a matrix of alloy compositions as follows:

**Table 2.3: Surface tensions of Mg-Al-Zn-Mn alloys as a function of alloying composition at 1023 K. Atmosphere and oxygen concentration not specified. (From Patrov et al. [58]).**

Alloying Element (wt%)			Surface Tension (N/m)
Aluminum	Zinc	Manganese	
0	0	0	0.570
10	2.5	0.25	0.522
5	5	0.25	0.522
5	2.5	0.5	0.552
0	5	0.5	0.522
10	0	0.5	0.539
10	5	0	0.496
0	0	0.5	0.57
0	5	0	0.57
10	0	0	0.566

## 2.2 Viscosity of Molten Metals

Viscosity is a physical property that quantifies the resistance to flow when subjected to an external force,  $F_o$ . The shear stress that causes the relative motion between layers of fluid is expressed as function of the velocity gradient. For Newtonian fluids:

$$\tau = \eta \frac{du}{dz} \quad (44)$$

Where  $\tau$  is the shear stress exerted on the fluid and  $u$  is the velocity which varies with position,  $z$ . The proportionality constant,  $\eta$ , is the dynamic viscosity of the fluid ( $\text{Nsm}^{-2}$ ). All liquid metals are considered to be Newtonian; however, it is important to keep in mind that Equation (44) is only valid if the flow is laminar (refer to Figure 2.18).

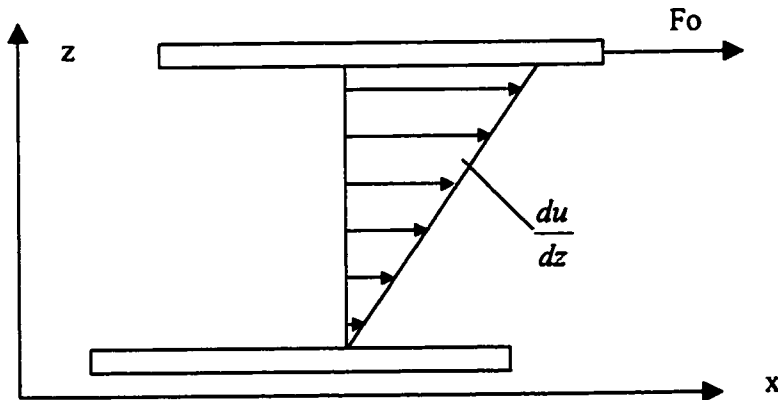


**Figure 2.18: Velocity profile of fluid subjected to external force.**

Figure 2.18 illustrates Couette flow, a laminar flow pattern. The lower plate is stationary and the upper plate moves with a uniform velocity. There is no pressure gradient in the  $x$ -direction. The only forces acting in the fluid are the shear forces due to the action of viscosity described by Equation (44). This flow configuration is relevant to rotational methods that will be described in Section 2.2.2. Other laminar flow configurations used

to determined viscosity are the Hagen-Poiseuille law for laminar flow in pipes. In this case a parabolic velocity profile is the result of fully developed flow in circular pipes where entrance effects are insignificant. This flow configuration is relevant to capillary methods that will also be described in Section 2.2.2.

### 2.2.1 Theoretical Determination of Viscosity

The Andrade formula is often used to predict the viscosity of melts at their melting point [48]. The model is based on momentum of atomic vibration. The formulation produces the following relationship:

$$\eta_m = LT_m^{1/2} M^{-1/6} \rho_m^{2/3} \quad (45)$$

Where  $\eta_m$  is the viscosity at the melting point,  $T_m$  is the liquidus temperature,  $M$  is the molecular weight of the metal,  $\rho_m$  is the density at the melting point, and  $L$  is a constant determined from viscosities of metals at their melting points. By plotting the known viscosities of certain metals at their melting points versus  $T_m^{1/2} M^{-1/6} \rho_m^{2/3}$ , the constant,  $L$ , is determined from the slope. Hirai [3] quoted the magnitude of  $L$  to be  $1.7 \times 10^{-7}$  (correlation coefficient of 0.95). In terms of varying composition and temperature, Hirai, provided an analysis of estimating the viscosity of liquid alloys. For superheats that are not excessive in relation to the liquidus temperature of the alloy, there appears to be a linear relation between  $\ln \eta$  and  $1/T$  [3]. The Arrhenius' formula is thus used to determine the temperature dependence of viscosity:

$$\eta = A \exp(B / RT) \quad (46)$$

where A, and B are constants. A plot of  $\ln\eta$  versus  $1/T$  yields the slope  $B/R$ , which changes in relation to the composition of the alloy. By experimentally determining the value of B for a variety of melts, Hirai plotted B versus  $T_m$  and proposed the following:

$$B = 2.65T_m^{1.27} \quad (47)$$

The correlation coefficient for Equation (47) is 0.96. By substituting Equations (47), and (45) into Equation (46), an expression for Constant A is determined:

$$A = \frac{1.7 \times 10^{-7} \rho_m^{2/3} T_m^{1/2} M^{-1/6}}{\exp\left(\frac{2.65T_m^{1.27}}{R}\right)} \quad (48)$$

As outlined by Hirai [3], in terms of multi-component systems,  $\rho_m$  and M, are determined by taking the weighted average of the pure metals. For binary systems, the liquidus temperature can be determined from a binary phase diagram [49].

### 2.2.2 Techniques to Measure Viscosity

There are a variety of techniques used to measure the viscosity of liquids. However, due to constraints of working at high temperatures, the methods applicable to molten metals are limited. The definition of viscosity by Equation (44) only holds for laminar flow. The techniques to measure viscosity that are described in this section all rely on this fundamental concept [2]. Some conventional methods for measuring viscosity are the following:

- a) Capillary Method,
- b) The Oscillating–Vessel Method,
- c) Rotational Method, and

d) The Oscillating Plate Method.

These techniques will be qualitatively explained; however, formulations and the procedural approaches are available from Iida and Guthrie [2].

*Capillary Method*

The capillary method measures the efflux time for liquid to flow through a capillary under a given pressure. The time required to discharge a certain volume of fluid depends on the viscosity of the liquid. A simple relationship used to relate the efflux time with the kinematic viscosity is the following:

$$\nu = \frac{\eta}{\rho} = C_1 t - \frac{C_2}{t} \quad (49)$$

Where  $t$  is the efflux time and  $C_1$  and  $C_2$  are constants that are related to the dimensions of the capillary. By using fluids of known properties, the constants are determined by calibration. Visual observation is typically made through the viscometer to determine the time required for the volume to be completely discharged. The material is thus constructed of heat resisting glass and quartz glass meaning that only low melting point elements (Pb, Sn, Cd, etc.) are typically measured using this technique. The kinematic viscosities of molten metals are much lower than those of organic liquids due to the fact that density is of greater magnitude. It is thus necessary to construct a capillary of a suitably small radius so that the efflux time can be measured over a sufficiently long period of time. The cleanliness of the metal is an important issue since even minute inclusions would have a drastic impact on the efflux of the small capillary. Cleanliness in this case refers to solid inclusions and not impurities in solution.

### *Oscillating Vessel Method*

The principle behind this technique is monitoring the motion of a vessel or crucible that contains the liquid and is set in vertical oscillations by a suspension rod. Due to viscous dissipation in the vessel, the viscosity can be determined by measuring the decrease in the period of oscillation. This technique has been applied extensively for high temperature applications due to the relatively simple design and ease of implementation. Unfortunately, there is no definitive analytical formula that relates the viscosity to the period of oscillation. A number of equations have been formulated from different sources and have been frequently used [50,51].

### *Rotational Method*

This method makes use of a rotating vessel or crucible containing the liquid, and a cylinder that is placed in the center of the vessel. The vessel is rotated at a constant angular velocity, which, due to the viscous nature of the liquid, exerts a torque on the cylinder. The torque is registered by measuring the angular rotation of a suspension fiber. The mathematics is relatively simple in this case. However, for non-viscous fluids (typical of molten metals), the gap between the vessel and the inner cylinder must be small enough such that the cylinder experiences sufficient torque. This puts a difficult constraint on the design capabilities, particularly at high temperatures.

### *Oscillating Plate Method*

The principle behind this technique is viscous dissipation monitored by a flat plate immersed in the liquid that experiences oscillations. If the oscillations are operating at constant force, the amplitude of the oscillations is a direct function of the viscosity of the liquid. A simplified version of the formulation is:

$$\rho\eta = Y \left( \frac{Am_1}{Am_2} - 1 \right)^2 \quad (50)$$

where  $Am_1$  and  $Am_2$  are the resonant amplitudes of the plate in air and in the liquid respectively.  $Y$  is an apparatus constant which is determined through calibration methods. The oscillating plate method is attractive from the point of view of equipment design and the simplicity of measurement. The product  $\rho\eta$  can be determined over a large temperature range because the amplitudes can be monitored as the liquid is heated. The technique is unsuitable, however, for low viscosity fluids because a very large plate would be required, which often presents serious experimental difficulties.

### 2.2.3 Experimental Data

Often, experimental viscosities are of different magnitudes than the theoretical formulation derived in Equations (46-48). Theoretically, the Andrade approach is based on a molecular basis (momentum of atomic vibrations). Dissimilarly, the experimental approach is based on bulk flow in the laminar regime that produces shear stress exerted by a surface on the fluid flowing in one direction (refer to Equation (44) and Figure 2.18). Experimentally, however, the effect of temperature on viscosity, is often described by Arrhenius' equation (Equation (46)).

Despite the numerous measurements for many liquid metals that have been performed in the past one hundred years, there exist discrepancies in the data reported for certain metals, including aluminum, iron, and zinc [2]. The high reactivity of these elements and the difficulties of taking measurements at high temperatures are considered



to be among the main reasons for these discrepancies. Oxide contaminated aluminum has been quoted to have a viscosity 8% higher than melts that are nearly oxide free [52]. Figure 2.19 presents the results from a number of studies in measuring the viscosity of aluminum. Both Jones and Bartlett [53] and Kisun'ko et al. [56] used the principle of the rotational method. Both Rothwell [55] and Yao and Kondic [54] used a modified version of the oscillating plate method by incorporating a sphere rather than a flat plate. The most recent results published by Kisun'ko et al., and Rothwell are within the closest agreement compared with other researchers. Assuming that recent technological advances have improved the accuracy of the measurements, it is assumed that results published from these researchers are more reliable, and that the viscosity is much lower than what was determined from previous analyses. It is most interesting to note the results of Yao and Kondic that indicate a difference in purity between 99.96% and 99.9935% results in a dramatic difference in viscosity. The importance of providing conditions of minimal contamination is illustrated from these results.

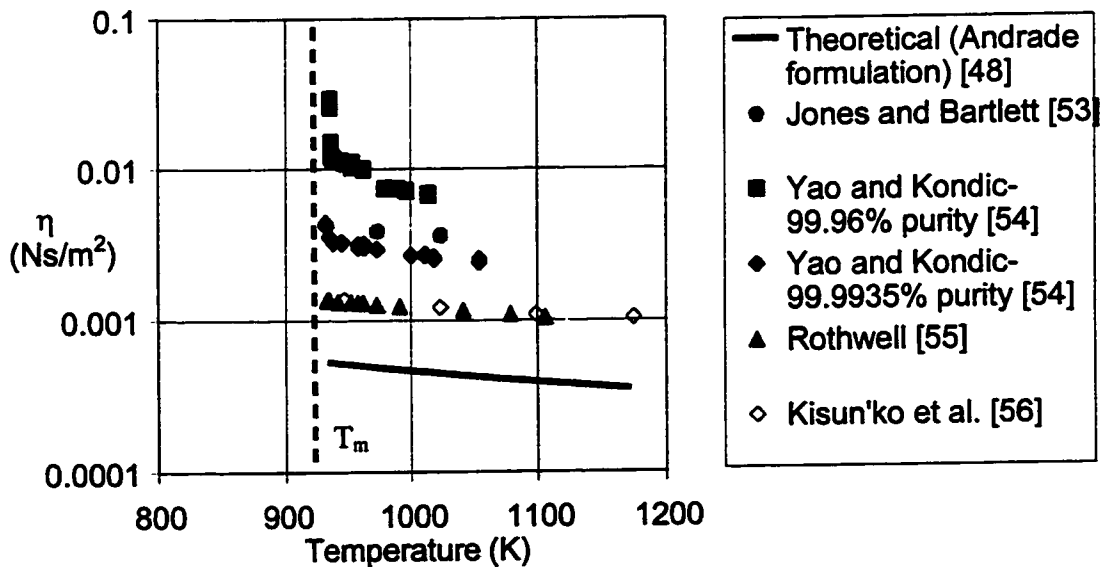


**Figure 2.19: Experimental viscosity of molten aluminum as a function of temperature from different sources.**

The viscosity of a wide range of pure metals is available from “The Viscosity of Liquid Metals” from Liquid Metals [52]. The data are presented in the form of the Arrhenius formula with constants A, and B included. Smithells Metals Reference Book [17] directly quotes the values obtained from this study. The Physical Properties of Liquid Metals [2] does not include the variation of viscosity with temperature and is not included in this study. Table 2.4 summarizes data for aluminum and magnesium. The viscosities of aluminum and magnesium using these constants are illustrated in Figure 2.20 as a function of temperature. At the respective melting points, the viscosities of both metals are similar; however, the viscosity of magnesium appears to decrease with temperature at a greater rate.

**Table 2.4: Viscosity of aluminum and magnesium from sources in the literature [17,52].**

Source	Metal	Viscosity at melting point, $\eta_m$ (Nsm <sup>-2</sup> )	Constants for Arrhenius' Formulation A (Nsm <sup>-2</sup> ) B (J/mol)
1. <u>Smithells Metals Reference Book</u> [17] 2. “The Viscosity of Liquid Metals” from <u>Liquid Metals</u> [52]	Aluminum	$1.25 \times 10^{-3}$	A = $1.49 \times 10^{-4}$ B = 16500
	Magnesium	$1.22 \times 10^{-3}$	A = $2.4 \times 10^{-5}$ B = 30500

Recall  $\eta = Ae^{B/RT}$

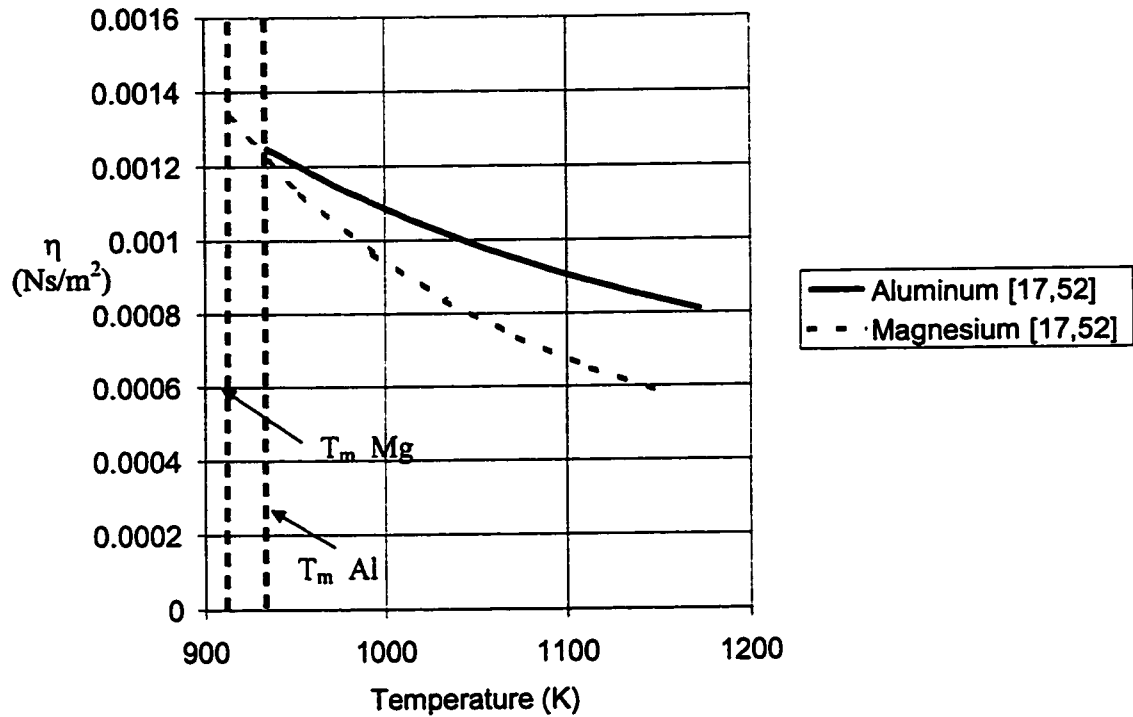


**Figure 2.20: Viscosity of aluminum and magnesium quoted in the literature [17,52]**

### 2.3 Density of Molten Metals

Density is a physical property of fundamental importance. There have been extensive data published in the literature on the density of pure metals; however, more data is needed for high melting point metals and alloys. Nonetheless, in relation to viscosity and surface tension, there is generally more information available for the density of molten metals. In terms of alloy systems, it has often been found that the atomic volumes of each alloying element is additive, indicating that the following relation is of use [2]:

$$v = \sum_i x_i v_i \quad (51)$$

The terms “ $v_i$ ” and “ $x_i$ ” refers to the atomic volume ( $\text{m}^3/\text{mole}$ ) and mole fraction of the alloying elements respectively. The density is determined by dividing the molecular weight by the atomic volume of the liquid ( $\rho = M/v$ ). Equation (51) indicates that metallic mixtures may behave as ideal solutions. This concept will be tested in Chapter 6 when Al-Mg-Zn-Mn alloys will be discussed.

There appears, in most cases, to be a linear dependence of density with temperature. It has been found that density can be represented by:

$$\rho = \rho_m + \frac{d\rho}{dT}(T - T_m) \quad (52)$$

Where  $\rho_m$  is the density at the melting point, and  $d\rho/dT$  is the linear temperature coefficient of the metal.

### 2.3.1 Techniques to Measure Density

Constraints, including contamination and reactivity as well as the difficulties in operating at high temperature are also pertinent in measuring density as they were for surface tension and viscosity measurements. There are a variety of methods used to measure the density of molten metals. Some are more advantageous than others depending on the particular systems that are to be measured. Five techniques will be briefly described.

- a) Archimedian Method,
- b) Pycnometric Method,

- c) Dilatometric Method,
- d) Manometric Method, and
- e) Maximum Bubble Pressure Method.

A full discussion of each is available in Iida and Guthrie [2]. A brief summary will be given below.

#### *Archimedean Method*

When a solid body of known weight is immersed in a liquid specimen, a new apparent weight is observed. This is due to the buoyant effect the liquid has on the solid object. The difference between the two weights is used to calculate the density of the liquid, using:

$$\rho = \frac{\Delta w_{ob}}{gV_{ob}} \quad (53)$$

where,  $\Delta w_{ob}$  is the difference of the weight of the object before and after being submerged in the liquid, and  $V_{ob}$  is the volume of the object. The apparent weight is measured by hanging the object from a wire that is attached to the arm of a weighing balance. This technique is attractive due to its relative simplicity; however it has been observed that there are surface tension effects between the wire and the liquid that often must be quantified in the analysis. Also the apparatus must be corrected for thermal expansion if accurate measurements are to be made. Although metals are frequently used for the suspension wire, problems of reactivity between the liquid metals and wire material, as well as the immersed object, are frequently encountered.

#### *Pycnometric Method*

The basic concept of this technique is simple. The density is determined by filling the liquid metal in a vessel of known volume and the mass is measured following

solidification. The volume must be known with a great deal of confidence if this technique is to provide reliable data. The apparatus must be machined to appropriate tolerances, and there must be no reaction between the walls of the vessel and the liquid metal. Finally, the apparatus material must have a defined coefficient of thermal expansion so that any modified volume from heating can be accounted for. Despite these issues, accurate measurements have been made using this method. It is worth noting, however, that the temperature dependence of density is not practically measured using this method since only one measurement can be made at one temperature. This is because the material is solidified after performing one test made at one particular temperature.

#### *Dilatometric Method*

This technique has been widely used to measure the density of many molten systems. It consists of a vessel of known volume that is fitted with a long narrow neck of known dimensions. A finite mass of material is added to the apparatus where it is melted. The height of the meniscus of the melt is monitored in the neck portion to determine the precise volume of that particular mass of liquid. This technique is useful in that it is considered to be quite accurate and it requires very little material. This technique can only be used for low melting point metals, however, since Pyrex or quartz must be used if the level is to be visually ascertained. Height measurements have been made, however, using electrical contact methods with non-transparent materials.

#### *Manometric Method*

If a pressure of known magnitude is applied to one of the columns of a u-tube monometer containing a liquid metal, a height differential will be established between the

columns of the u-tube. By measuring the difference in height, the density can be calculated as follows:

$$\rho = \frac{P_g}{g\Delta h} \quad (54)$$

Where  $P_g$  is the gage pressure applied to one of the columns and  $\Delta h$  is the resulting height differential. Like the dilatometric method, visual observation can only be made if the material is constructed of Pyrex or quartz.

#### *Maximum Bubble Pressure Method*

The final technique that will be discussed in this section is identical to the technique of the same name that measures surface tension in section 2.1.4. It was stated that from analysis of Equation (34) that it is possible to measure both surface tension and density by varying the depth that the capillary tube is submerged in the liquid. The slope of maximum pressure versus depth yields the density of the liquid.

### **2.3.2 Experimental Data**

The density of molten metals is available from a variety of sources. Table 2.5 summarizes the density of aluminum and magnesium as a function of temperature represented by  $dp/dT$ . The references used here are quoted from The Physical Properties of Liquid Metals [2] as well as Smithells Metals Reference Book [17].

**Table 2.5: Density of aluminum and magnesium from sources in the literature [2,17].**

Source	Metal	Density at melting point, $\rho_m$ (kg/m <sup>3</sup> )	Temperature dependence of density, $d\rho/dT$ (kgm <sup>-3</sup> K <sup>-1</sup> )
<u>Physical Properties of Liquid Metals</u> [2], 1988	Aluminum	2380	-0.35
	Magnesium	1590	-0.260
<u>Smithells Metals Reference Book</u> [17], 1998	Aluminum	2385	-0.26
	Magnesium	1590	-0.264

## 2.4 The Saybolt Viscometer

A standard that measures viscosity deserving of considerable attention is the Saybolt viscometer [65-78]. The formulations and experiments performed in this thesis have striking similarities with this device. By measuring the efflux time of a liquid from a vessel through an orifice of specific dimensions, it is expected that viscosity can be determined since it is a function of the efflux time. In Chapters 4 and 5, it will be shown that flow through the orifice is induced from the hydrostatic pressure of the liquid head above the orifice much like it is in the Saybolt viscometer. This section will provide the theoretical basis behind the Saybolt viscometer. Of particular relevance to this thesis are the effects of surface tension at the orifice tip. It is of interest to determine if surface tension has played a role in the development of this device; and more importantly, if surface tension has been properly quantified in the formulation.



There are a variety of techniques that consist of orifice-type viscometers. Among them are the Redwood, Engler and Saybolt viscometers. The Saybolt viscometer is used predominately in the petroleum industry and is most widely referenced when researching this type of viscometer. All devices follow the same principle in that the efflux time taken to drain a given volume of liquid can be expressed as a relative viscosity measurement. For instance, the unit “Engler degrees” is the unit measure of viscosity for the Engler device. This unit is the ratio of efflux time for the liquid being tested to the time taken for water at 20°C. The Saybolt viscometer simply takes the efflux time and quotes units of Saybolt Universal seconds (SUS) or Saybolt Furol seconds (SFS). The Saybolt Universal second is the measurement made through a calibrated Universal orifice under specified conditions. The Saybolt Furol second is the measurement made through a calibrated Furol orifice, which should be used if the Saybolt Universal second is greater than 1000s as specified by ASTM standard D 88 – 94 [77].

The Saybolt viscometer was originally published in the Annual Book of ASTM Standards in 1923 as ASTM D 88 – 21. Before this date, the device was accepted as a standard from an initiative of G. M. Saybolt (the inventor of the device) and the Bureau of Standards in 1917 [66]. To comprehend the theoretical basis of the Saybolt viscometer, it is necessary to understand the work published at this time.

The principle of these viscometers is similar to the capillary viscometers discussed in Section 2.2.2 except that Hagen-Poiseuille flow is certainly not established within the short section of the orifice length. For this flow to be established, the length to diameter ratio of the orifice must be greater than 10 [76]. This ratio for the Saybolt

viscometer is approximately 7.0 [65,66]. For fully developed flow, the following equation applies [65,66]:

$$\frac{V_d}{t} = \frac{\pi \Delta P d_{cap}^4}{128 \eta l_{cap}} \quad (55)$$

For flow in capillary tubes, the time a certain volume takes to discharge ( $V_d$ ) depends on a difference in pressure, the diameter of the capillary ( $d_{cap}$ ) and the length of the capillary ( $l_{cap}$ ). The viscosity,  $\eta$ , is calculated by quantifying each of the terms in Equation (55). This relationship has successfully been used to model viscous flow in capillaries; however it has been observed that results have not agreed with this law when the velocity was very high in the shortest of capillaries [65]. A correction factor has been proposed that accounts for part of the pressure that is in reality expended in setting the liquid in motion and not in overcoming viscous resistance [65,66]. A “kinetic energy correction factor”, represented by the symbol  $\xi$ , is deducted from the pressure difference to account for this phenomenon. Another term that accounts for “end effects” for a specified length of tube is the “Couette correction factor”, represented by the symbol  $\psi$  [65,66]. A modified form of Equation (55) that accounts for these terms is the following written in terms of kinematic viscosity:

$$\nu = \frac{\eta}{\rho} = \frac{\pi g d^4 t d_{cap}^4}{128 V_d (l_{cap} - \psi)} \left( \hat{h} - \frac{\xi \hat{u}^2}{g} \right) \quad (56)$$

The average velocity in the tube is represented by  $\hat{u}$ . Equation (56) states that hydrostatic pressure of the liquid above the orifice induces the flow. Hence, the gravitational constant, density, and the “average head”, symbolized by  $\hat{h}$ , is introduced in the

formulation. The average head is considered a constant and is determined using the following relationship [66]:

$$\hat{h} = \frac{h_1 - h_2}{\log_e \left( \frac{h_1}{h_2} \right)} \quad (57)$$

The head before draining is  $h_1$  and head after discharge is  $h_2$ . Using the dimensions of the device, most of the terms in Equation (56) can be substituted with the exception of values related to kinetic energy and Couette correction factors [66]. Table 2.6 gives the dimensions of the first standard Saybolt Universal viscometer in 1917. These dimensions are the same today as outlined in ASTM D 88 – 94 [77]. Refer to Figure 2.21 for a representation of the Saybolt Universal viscometer. The Saybolt Furol orifice is different than the Saybolt Universal orifice in that  $d_{\text{cap}} = 3.150 \pm 0.002 \text{m}$  and  $d_{\text{tube}} = 4.3 \pm 0.2 \text{m}$  [77].

Herschel rewrote equation (56) in terms of kinematic viscosity, efflux time, and two constants determined empirically since the kinetic energy and Couette correction factors are unknown [65,66]:

$$\nu = \frac{\eta}{\rho} = \dot{C}_1 t - \frac{\dot{C}_2}{t} \quad (58)$$

Note that Equation (58) is of the same form as Equation (49), used in capillary measuring methods. This is not surprising since this device is modelled from principles of Hagen-Poiseuille flow. The constants  $\dot{C}_1$  and  $\dot{C}_2$  must be determined through calibration using fluids of known viscosities. Using a number of fluids of varying viscosities, the constants can be graphically determined. Dividing the left and right hand side of equation (58) by  $t$ :

$$\frac{\nu}{t} = \frac{\eta}{\rho t} = \dot{C}_1 - \frac{\dot{C}_2}{t^2} \quad (59)$$

Plotting  $\eta/(\rho t)$  versus  $1/t^2$  for a variety of liquids yields an intercept value of  $\dot{C}_1$  while the slope of the linear relationship determines the value of  $\dot{C}_2$ . This approach conducted by Herschel in the standardization of the Saybolt viscometer was performed with a variety of liquids that are referenced in [66]. It was determined that water was an unsuitable calibration fluid because a departure from linearity was observed for low kinematic viscosities associated with water. This is attributed to turbulent flow, which is an indication that Equation (56) no longer applies since this relationship describes laminar-viscous flow in a capillary only [65]. It has been observed from experimental results that when Reynolds numbers are in excess of 1500 the Saybolt Universal viscometer is unsuitable for testing [65,66]. Glycerol solutions were also determined to be inapplicable as calibration fluids due to issues concerning evaporation during the draining of the liquid [66]. Sucrose solutions were also scrutinized for calibration purposes due to the high surface tension of these liquids compared with other calibration liquids. For the standardization of the Saybolt viscometer, Herschel described tests with sucrose solutions that were consistent with one another, but produced lower positions of the calibration curve than tests obtained with alcohol solutions. He directly attributed this difference to the effects of surface tension, and stated that calibration liquids must be selected with surface tensions most nearly equal to that of oils, since Saybolt viscometers are mainly used for testing oils [66]. Although Herschel confirmed the influence of surface tension effects on the dynamics of the Saybolt instrument in 1917, there was no attempt in quantifying this effect. In the literature, there has been no further reference made in pursuing this matter [65-78].

The standardization of the Saybolt viscometer in 1917 determined that kinematic viscosity could be converted from Saybolt Universal seconds as follows:

$$\nu = \frac{\eta}{\rho} = (2.220 \pm 0.14) \times 10^{-3} t - \frac{1.80 \pm 0.02}{t} \quad (60)$$

Presently, the form this equation assumes is similar. For example, in The Measurement, Instrumentation, and Sensors Handbook [76],  $\dot{C}_1$  and  $\dot{C}_2$  are said to equal  $2.226 \times 10^{-3}$  and 1.95 respectively. An ASTM standard exists today that publishes tables that convert Saybolt Universal and Furol seconds to kinematic viscosity values [78].

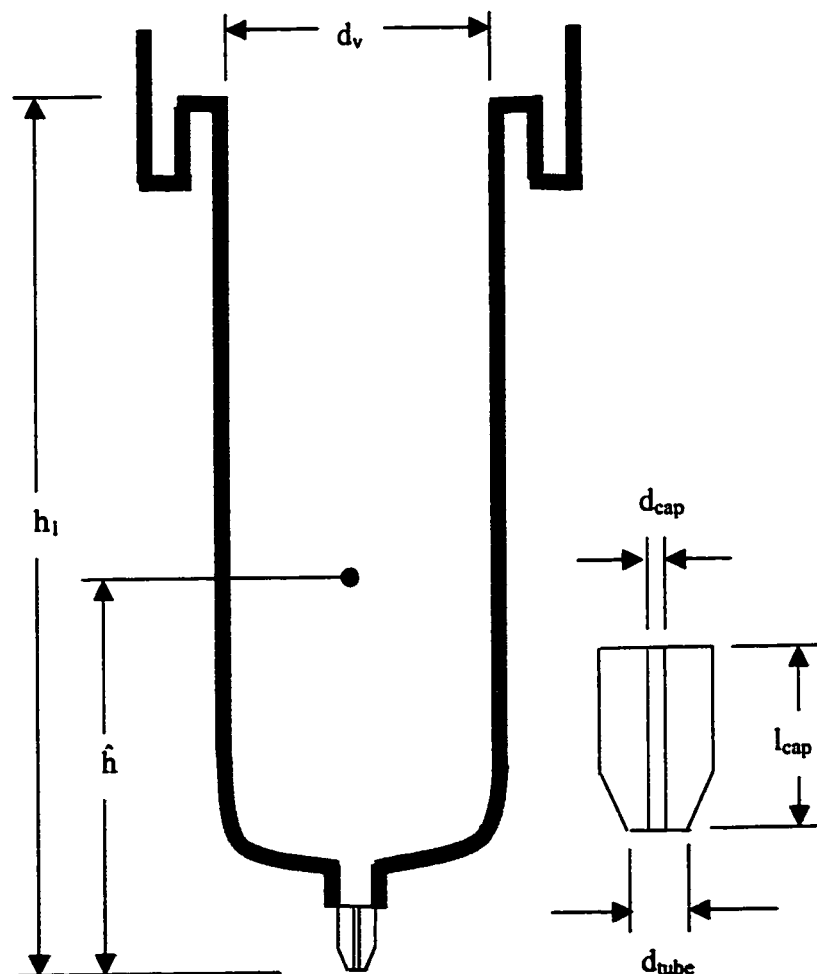


**Figure 2.21: Dimensions of the Saybolt viscometer.**

**Table 2.6: Standard dimensions of the Saybolt Universal viscometer.**

Dimension	Min (m)	Normal (m)	Max (m)
Length of outlet tube (capillary), $l_{cap}$	$1.750 \times 10^{-3}$	$1.765 \times 10^{-3}$	$1.780 \times 10^{-3}$
Diameter of outlet tube (capillary), $d_{cap}$	$1.215 \times 10^{-2}$	$1.225 \times 10^{-2}$	$1.235 \times 10^{-2}$
Outlet diameter of tube, $d_{tube}$	$2.8 \times 10^{-3}$	$3.0 \times 10^{-3}$	$3.2 \times 10^{-2}$
Height of overflow rim above outlet tube, $h_l$	$1.240 \times 10^{-1}$	$1.250 \times 10^{-1}$	$1.260 \times 10^{-1}$
Diameter of vessel, $d_v$	$2.955 \times 10^{-2}$	$2.975 \times 10^{-2}$	$2.995 \times 10^{-2}$
Average head, $\bar{h}$	$7.16 \times 10^{-2}$	$7.36 \times 10^{-2}$	$7.56 \times 10^{-2}$

## 2.5 Conclusions

Operating at high temperatures in particularly reactive environments, (i.e. in the presence of oxygen), poses many challenges in experimentally determining the physical properties of molten metals. Techniques used for low temperature work (i.e. organic liquids), do not apply in many cases due to such challenges. This will be clearly demonstrated in the next chapter where a new apparatus for measuring the physical properties of molten metals will be described. It will be compared with another apparatus based on similar principles, but operating at lower temperatures. This will illustrate the challenges in operating at high temperatures in a very practical manner.

Attempts to understand the sensitivity of surface tension, viscosity and density to temperature and composition have been made throughout the literature. Surface tension and density are assumed to vary linearly with temperature [2,7]. Viscosity, however, is assumed to vary with temperature according to the Arrhenius formulation [3].

Theoretical determination using the Andrade formulation for viscosity is much lower than experimental results for aluminum. For molten aluminum, the magnitude of the surface tension is a strong function of the amount of oxide that covers the surface of the melt [8]. The surface tension of multi-component systems is often a complex issue; however, the Gibbs adsorption equation has explained the results for a number of studies [5,15,16]. Finally, it has also been shown that the surface energy in molten systems is much higher than systems of organic liquids. In fluid dynamic applications of metallurgical processes, surface energy must be accounted for more often, and the scarcity of accurate information is problematic. Such a situation will be explored in subsequent chapters where the problem of free jets from small orifice tanks will be discussed. These tests differ from the Saybolt instrument in that the principle experimental variables are head and flow rate, and not simply the efflux time. There have been numerous studies in the literature addressing this issue for low temperature liquids, and throughput has traditionally been characterized by quantifying potential, inertial and viscous energies in the system [59,60]. This system will be re-examined for molten metals systems to determine if it is necessary to account for surface energy; and if so, under what conditions.

## **CHAPTER 3:        EXPERIMENTAL**

This chapter will describe the equipment used in generating controlled flow through an orifice such that head and flow rate, the two principle variables, can be accurately measured. There are two purposes to this discussion. First, this exercise will provide a better understanding of the system and the limitations of the experiment. Secondly, the difficulties intrinsic to high temperature applications will be clearly demonstrated by discussing the apparatus used in both low-temperature and high-temperature work. Issues dealing with heat supply and atmospheric control, relevant to melts, will be addressed in this chapter. A full description of the experimental procedure will be presented as well as the specifications of metal purity and quality of the gases.

### **3.1     Low Temperature Apparatus**

The apparatus for low temperature applications is illustrated in Figure 3.1. A rectangular Pyrex draining vessel (0.035m x 0.075m x 0.250m) was constructed so that visual observations can be made of fluid head. The fluid drains through the orifice plate and is collected into a 1 litre beaker that is placed no less than 0.03m below the orifice plate. The orifice plate and vessel are held together using a system of threaded rods. The beaker is mounted on the loadcell as shown.



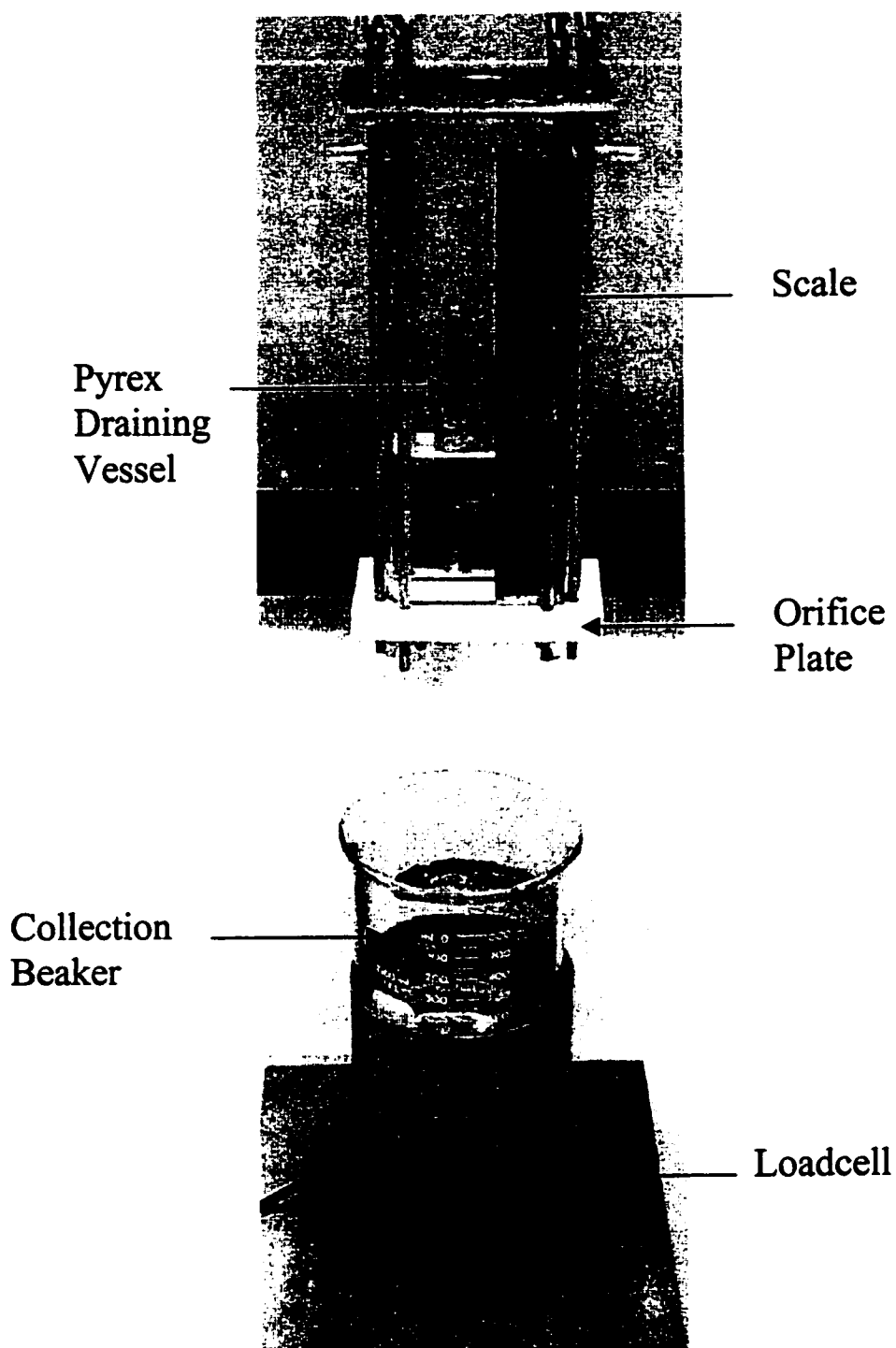


**Figure 3.1: Low temperature apparatus.**

The loadcell (LCCA-25 supplied by Omega) is used to measure flow rate by measuring the mass poured through the orifice with time. It generates a voltage signal that is detected by the data acquisition system described in section 3.2.6. Using an excitation of 10 Vdc, and outputting  $3\text{mV/V} \pm 0.0075\text{mV/V}$  (obtained from Omega), the loadcell registers up to 11 kg of mass. It is important that the collection beaker is placed as close as possible to the orifice plate so that the stream does not break-up before impact. If this precaution is overlooked, an erratic signal will be registered by the loadcell, directly resulting in scatter in data collection. The erratic signal is due to discrete droplets formed after breakup that impact the loadcell at irregular intervals. The result is a highly variable detection of strain. A second order polynomial is fitted to the cumulative mass that is plotted as a function of time. This relation is differentiated, which results in a new function describing flow rate as a function of time. This will be discussed further in sections 3.1.2 and 3.2.8.

The head of the fluid is measured in two ways. Visual observation through the draining vessel can be made and recorded using a video camera. A Sony color video CCD camera (DXC-151) is used with a 35mm lens approximately 1 m away to record the experiment onto a VHS videotape. The head is also calculated through careful calibration of the draining vessel geometry. Prior to experimentation, water samples of known volume are related to head measured in the draining vessel. The volume is measured indirectly by measuring the weight of the water, using an Ohaus GT 8000 scale. Temperature is measured so that the volume can be calculated using reliable density data [61]. The scale used for visual observations as well as for the calibration of the crucible is accurate to 0.0005m (500 $\mu\text{m}$ ).

### 3.1.1 Orifice Plates

Refer to Figure 3.2 for dimensions of the orifice plate. Teflon was used to construct a 0.016m thick plate with a 0.003m orifice hole in the center where the fluid drains through. The entrance of the orifice is chamfered so that entrance effects will be lower than in the case of a square entrance. The holes for the threaded rods are also indicated.

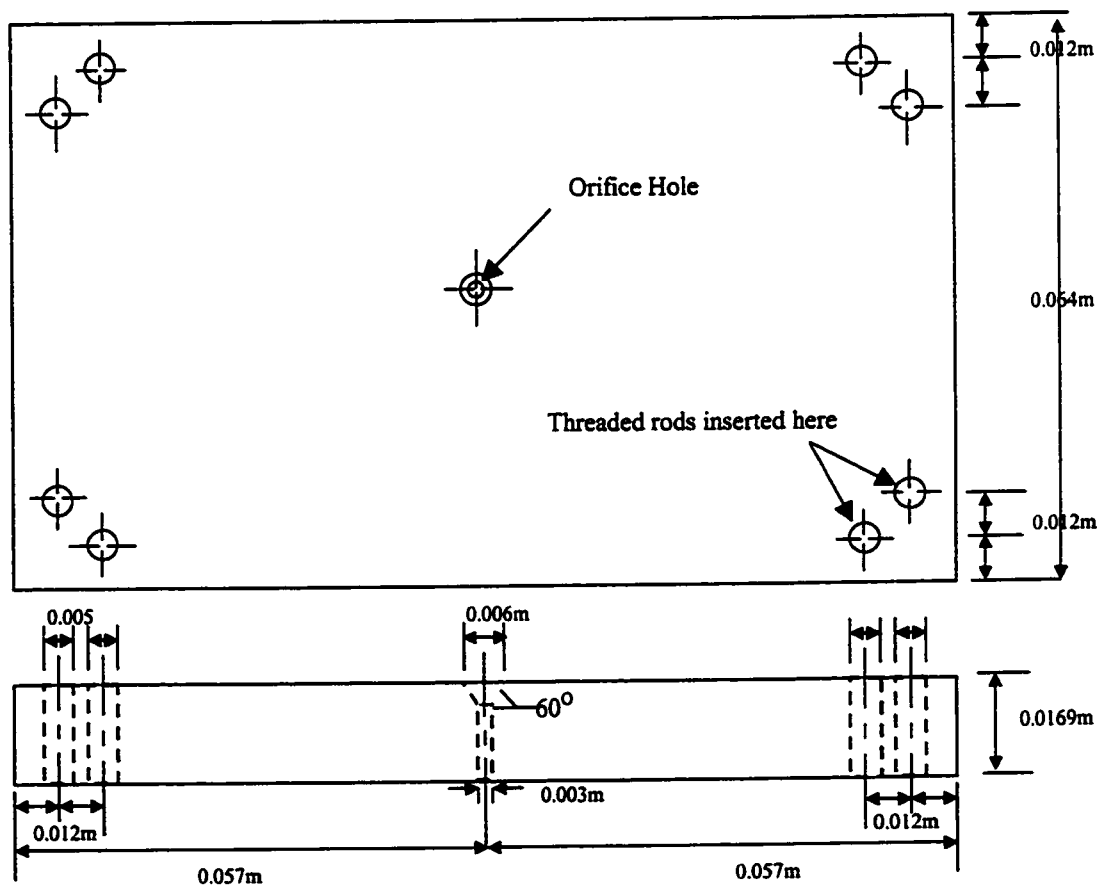


**Figure 3.2: Orifice plate design for low temperature apparatus.**

### **3.1.2 Procedure for Low Temperature Experiments**

1. The thermocouple is inserted through the top and placed approximately 0.005m from the orifice inlet. The thermocouple is positioned at this distance to measure the temperature at the orifice without interfering with the dynamics of the experiment.
2. A stopper is placed through the orifice outlet to ensure that the fluid does not begin pouring out once it is added to the draining vessel.
3. The draining vessel is filled to a head no greater than 0.19m registered on the adjacent scale.
4. Once it is determined that the fluid appears still and the experiment is ready to proceed, the stopper is removed and the fluid is allowed to flow into the beaker placed on top of the loadcell.
5. The loadcell and temperature data are registered and recorded on the data acquisition system and saved onto a floppy disk. A sample rate of 5Hz (0.2s per data point) is selected.
6. The data is imported into Excel (Microsoft corporation) where a polynomial is fitted to the cumulative mass curve versus time data. This function is differentiated to obtain the experimental flow rate at the respective head heights taken every 0.2s.
7. For an initial head height of 0.17m, the time taken to drain through the 0.003m orifice is approximately 70s for water and ethylene glycol between 293K and 353K.

## 3.2 Overview of High Temperature Apparatus

There are a variety of design and implementation challenges in measuring the physical properties of molten metals. Besides providing equipment that measures head and flow rate accurately, an apparatus is required that provides sufficient heat to melt the material and that can be closely monitored and controlled. Material selection becomes less trivial under these circumstances. As discussed in Chapter 2, since molten metals are often susceptible to surface oxidation, conditions must be provided to ensure that oxygen is kept at sufficiently low levels.

Refer to Figure 3.3 for a schematic of the high temperature apparatus. The material to be melted is placed in the crucible that rests on a bottom plate, 0.6m in diameter and 0.04m thick. The rest of the frame consists of a smaller plate that rests on top of the crucible that provides a level and rigid surface. The frame is contained within a stainless steel shell that contains the atmosphere. Air in the shell is evacuated using a vacuum pump (Speedivac supplied by Edward High Vacuum Ltd. Manor Royal, Crawley, Sussex, U.K.).

Once air is removed, gas enters the shell and exerts an overpressure of approximately 34000 Pa (5psig). The gas is purged out of the shell through a valve and is replaced by fresh gas from cylinders located near the unit. A sample of the purging gas is analyzed using an oxygen sensor and monitored. A safety release valve is located on the top of the tower and ensures that the pressure in the unit never exceeds 103000 Pa (15psig). The material is heated using an induction furnace. Induction leads enter the

tower and connect to the coil that is wrapped around the crucible. The temperature in the crucible is monitored using two k-type thermocouples, 0.0012 m in diameter.

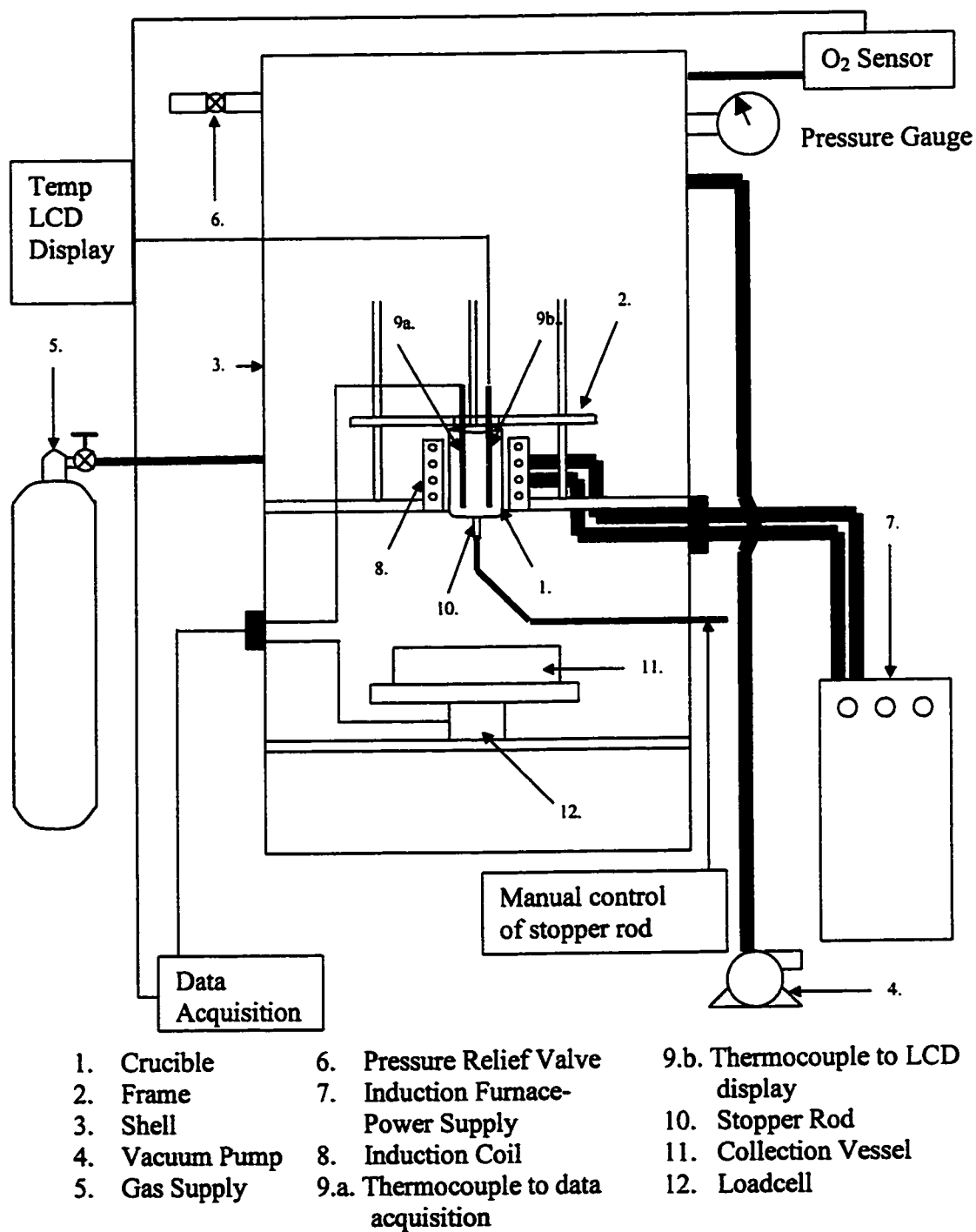


**Figure 3.3: High temperature apparatus.**

Before heating, the oxygen level that is obtained from the oxygen sensor must reach 20ppm. It is not possible to obtain oxygen levels below this level before heating using the existing apparatus. Once the material is molten and the oxygen content in the unit has reached equilibrium, the material is poured through the orifice plate and onto the loadcell (same as the low temperature work). During heating, a stopper rod is placed through the bottom of the orifice and released when the experiment is ready to proceed at a specified temperature and oxygen content. The loadcell supplier recommends that the loadcell never exceed 363 K. To ensure it is kept sufficiently cool, the melt is captured onto a stainless steel pan 0.30 m in diameter and 0.10 m high. For tests with aluminum, the pan contains SiO<sub>2</sub> (sand) for the purpose of dissipating heat. Also, the sand makes it possible to remove the material from the pan after it has solidified. For experiments with AZ91D alloy, MgO replaces SiO<sub>2</sub> due to concerns that magnesium may reduce SiO<sub>2</sub> resulting in an exothermic reaction. Insulation is placed between the loadcell and the pan for further protection.

Similar to the low temperature work, the head of the melt is determined using precise knowledge of the vessel geometry. Since a crucible is used, it is not possible to make visual observations of the head during the course of an experiment.

### **3.2.1 Orifice Plates**

AI16 graphite, supplied by Speer Canada Inc. (Kitchener, Ontario), is used because of its durability and strength to machine orifices. The frictional characteristics of the orifice may change if the material is brittle and susceptible to wear. It has been

observed in practice that Al16 graphite is suitable for repeated use under these conditions. Refer to Figure 3.4 for a schematic of the orifice plate design. Larger holes are required with molten metals than if low temperature liquids are used because of the high surface energy these systems exhibit relative to low temperature systems. Since small orifice sizes result in higher surface effects, the stream may break-up before impacting the loadcell resulting in the erratic signal discussed in Section 3.1. If surface effects are too high, a continuous stream is not formed at all and dripping ensues.

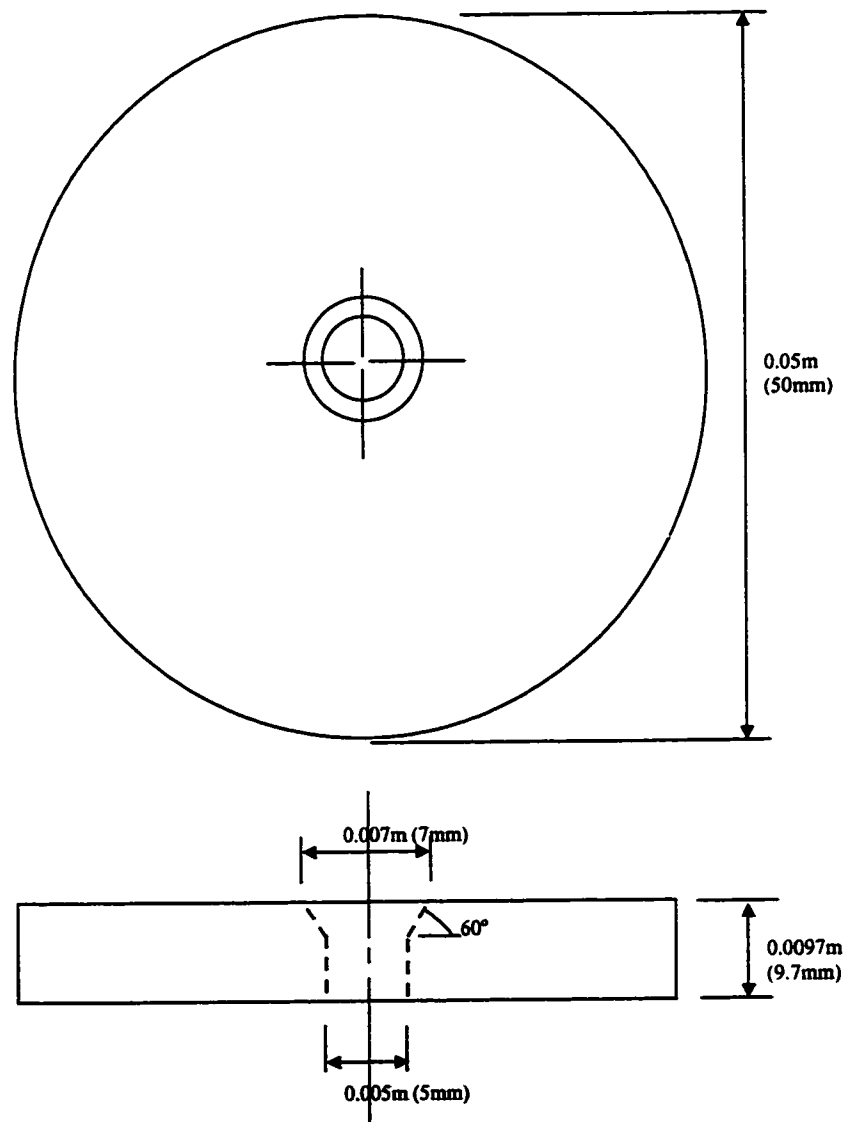


**Figure 3.4: Orifice plate dimensions for aluminum and AZ91D experiments.**



### **3.2.2 Crucibles**

For molten aluminum and AZ91D, clay graphite crucibles were supplied by Morganite Crucible Inc (Berkshire, U.K). Graphite is a suitable material for many high temperature applications because of its ability to withstand high temperatures and its inert characteristics with respect to aluminum and magnesium alloys. The dimensions of the crucibles are illustrated in Figure 3.5. The crucible will provide a capacity of approximately 0.9 litres of melt. A hole is machined through the bottom of the crucible with a depression in which the orifice plate is inserted. The orifice plates are cemented to the bottom of the crucible and cured at 366 K for 2 hours using "Graphi-Bond", a product used for graphite materials available from Aremco Products Inc.

### **3.2.3 Induction Furnace**

An Inducto 20 model furnace from Inductotherm Corp. was used for melting. The coil was wrapped around the crucible nine times, providing sufficient coupling to the crucible. Water is run through the copper coil so that excessive heat that is generated within the coil itself is removed. It is possible to monitor the lag/lead of the current and voltage signals to the coil so that an appropriate capacitance can be selected to ensure that power is being transferred efficiently. Insulation is placed between the coil and the crucible to ensure no direct contact is established that would result in a short circuit. Table 3.1 indicates the amount of power the furnace generates in order to reach a specific temperature.

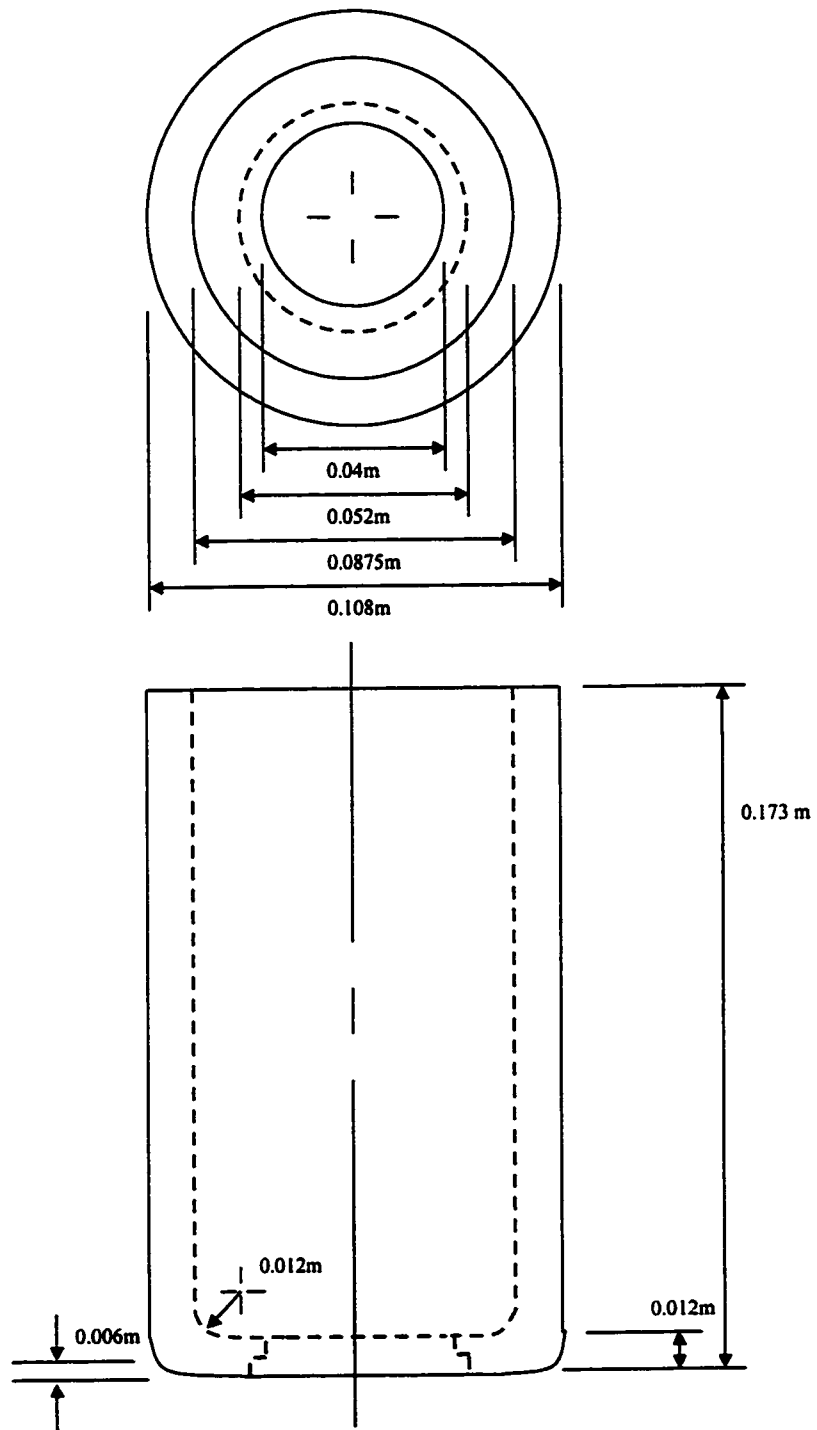


**Figure 3.5: Schematic of clay graphite crucible used for aluminum and AZ91D experiments.**

**Table 3.1: Power requirements of induction furnace.**

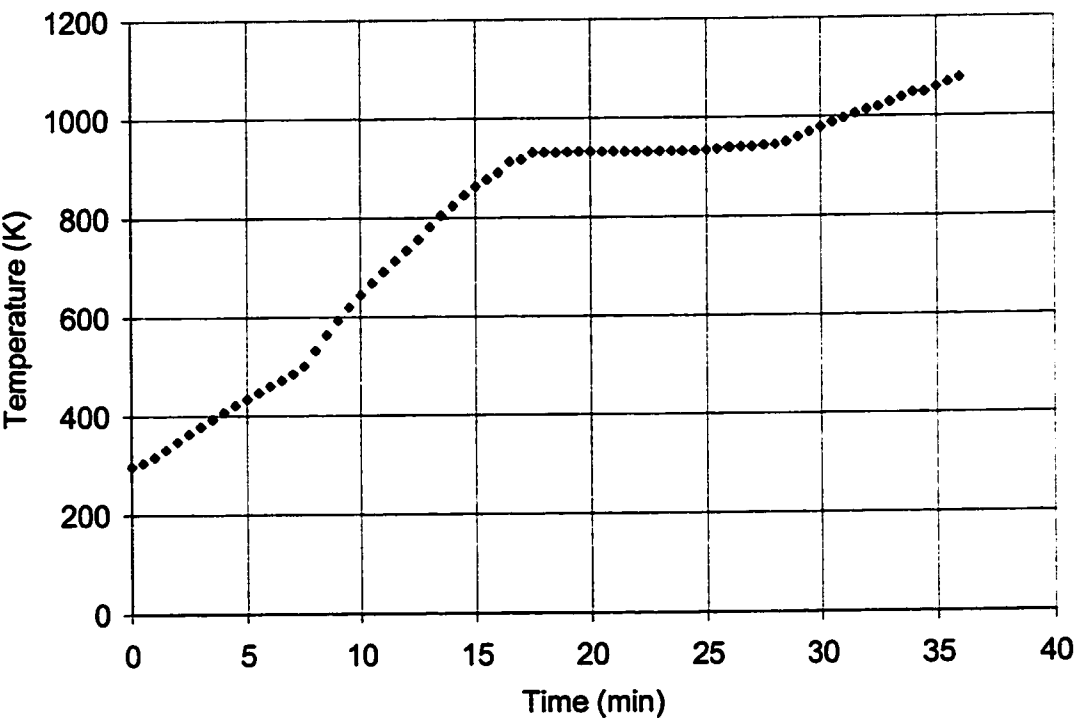
<b>Material</b>	<b>Temperature (K)</b>	<b>Power to Furnace (kW)</b>
1275g - 99.9% Aluminum	923	4
1275g – 99.9% Aluminum	1073	4.5
1275g – 99.9% Aluminum	1173	6
650g-AZ91D alloy	903	3.5
620g-AZ91D alloy	1073	5
660g-AZ91D alloy	1173	5.5

Figure 3.6a represents the time it takes to heat up aluminum to 1173 K. The melting point at 933K can be seen as that location on the curve where latent heat is being added with no change in temperature. The time required to heat AZ91D to 1073 K is represented in Figure 3.6b. The liquidus temperature of 903 K for this alloy is observed as that location on the curve where there is no change in temperature during heating.

#### **3.2.4 Purging Gas**

The gas used during these experiments was argon supplied by Praxair. The purity of this gas is of importance since surface tension depends strongly on the degree to which the atmosphere is contaminated. The grade of argon used is “pre-purified” which specifies a purity of 99.998%. The maximum amounts of oxygen and water present are both 5ppm. The maximum amounts of oxygen, water, carbon dioxide, THC and methane

do not exceed 20ppm. During the course of one experiment, one cylinder (49 litres) is typically consumed containing 19MPa (2640 psig) of gas.



**Figure 3.6a: Time required to heat 1.275 kg Aluminum to 1173 K.  
Aluminum Test# 29.**

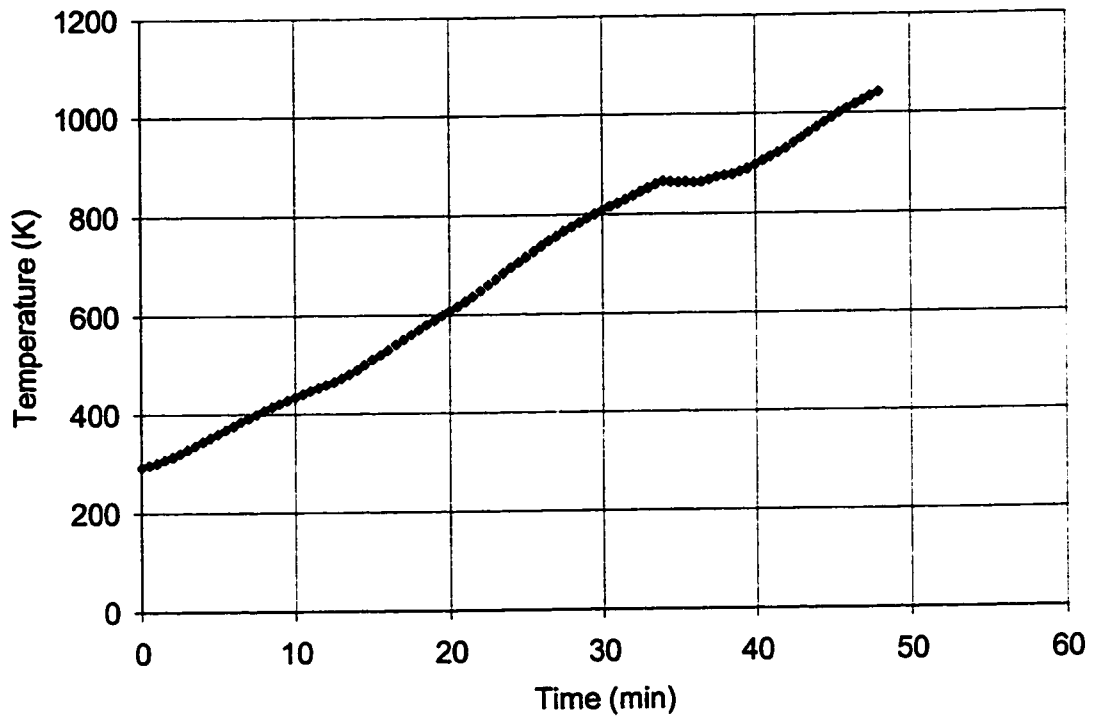


**Figure 3.6b: Time required to heat 0.620 kg AZ91D to 1023 K.  
AZ91D Test# 4.**

### 3.2.5 Metal Selection

The aluminum used in these experiments is supplied by Alfa Aesar and takes the form of 8-12mm granules. The surface tension is a strong function of the amount of impurities present in the melt, a number of which are presented in Table 3.2. Aluminum, Manganese, and Zinc are the principle alloying elements present in AZ91D. Silicon, copper, nickel and iron are elements commonly present as impurities [9]. Refer to Table 3.3.

**Table 3.2: Percent of elements found as impurities present in aluminum [62].**

<b>Element</b>	<b>Percentage-metals basis (wt %)</b>
Aluminum	99.93
Copper	0.001
Iron	0.0038
Lead	0.001
Nickel	0.001
Silicon	0.037
Zinc	0.001
Vanadium	0.003

**Table 3.3: Percent of elements added to or contained within AZ91D alloy [9].**

<b>Element</b>	<b>Percentage-metals basis (wt %)</b>
Aluminum	8.3-9.7
Manganese (min)	0.15
Zinc	0.35-1.0
Silicon (max)	0.1
Copper (max)	0.03
Nickel (max)	0.002
Iron (max)	0.005
Magnesium (balance)	~91

### 3.2.6 Data Acquisition System

Voltages from the loadcell, thermocouple, and oxygen analyzer are recorded using Instrunet, a data acquisition system supplied by GW Instruments Inc. (Somerville MA). Figure 3.9 illustrates how the system is connected. A network device box (0.10m x 0.12m x 0.25m) is connected to the controller board (inserted into PCI Slot of laptop computer) where devices are installed (loadcell, thermocouple, and oxygen analyzer). Instrunet software is displayed on the laptop monitor and data is saved on a floppy disk as text files. The laptop system is NEC Versa P series, 75 MHz CPU, 8MB standard RAM, 16 KB cache RAM (internal), 256 KB cache RAM (external), 256 KB ROM.

The loadcell requires an excitation voltage that is supplied directly from the network control box from the  $V_{out}$  terminal. The strain is registered between the  $V_{in}^-$  and  $V_{in}^+$  terminals. By selecting the strain gage option in the program, Instrunet recognizes the application and outputs units of strain. By manually measuring the mass that is collected following the experiment and comparing that value to the strain on the loadcell, a calibration constant is determined by taking the ratio of these two quantities. This constant is used to convert strain into mass. The output on the loadcell is linear and facilitates this calculation. The accuracy of the loadcell, as quoted from the supplier, is 0.037% full scale.

Temperature is measured directly by measuring the difference in voltage between the  $V_{in}^-$  and  $V_{in}^+$  terminals. By selecting k-thermocouple in the hardware menu, voltage is directly converted to degrees celcius.

The oxygen sensor does not output units of concentration. A voltage is also measured between the  $V_{in}^-$  and  $V_{in}^+$  terminal; however, this quantity must be converted to concentration independently of the DAS. The conversion is explained in section 3.2.7.

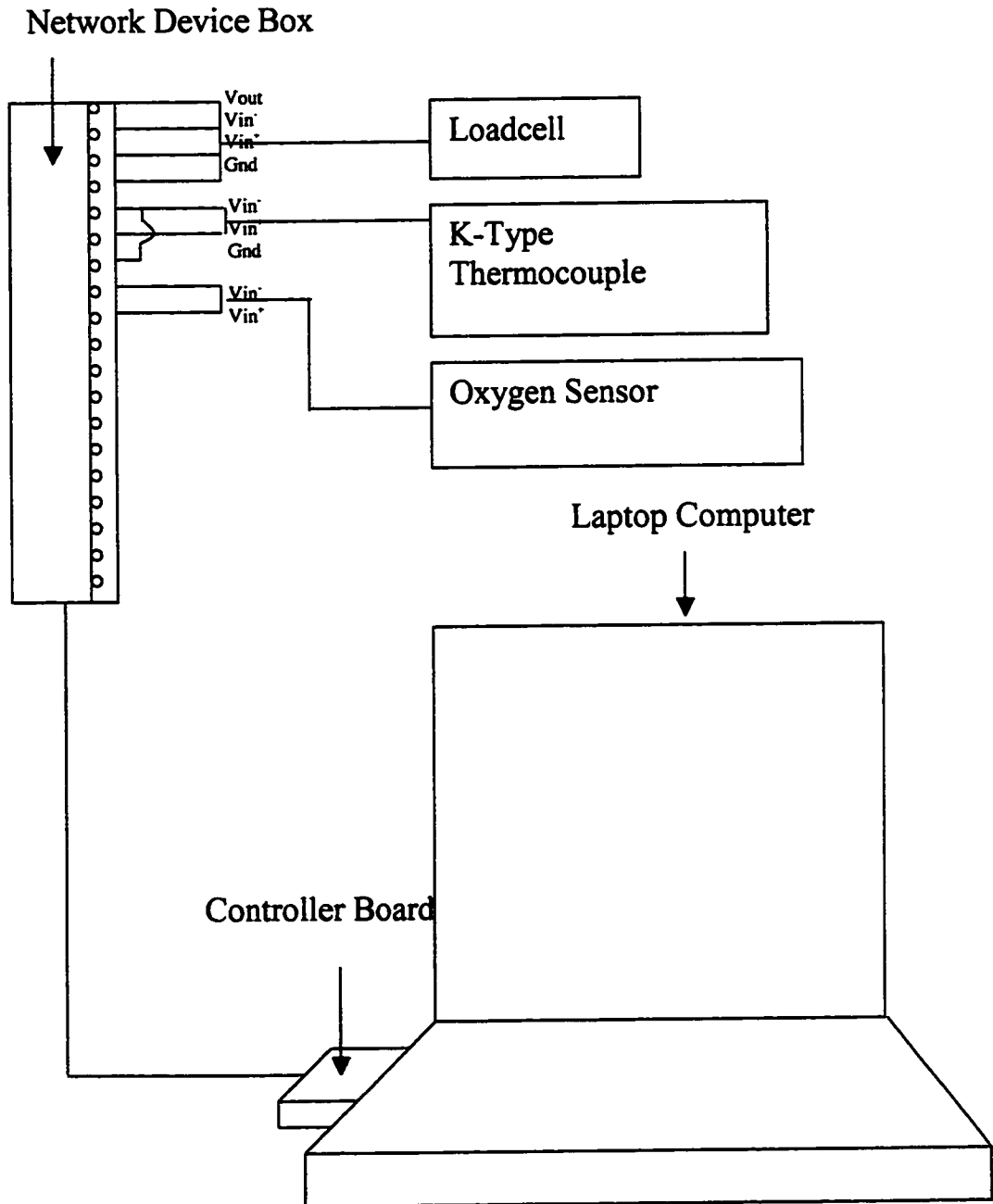


**Figure 3.7: Data acquisition system used to acquire loadcell, thermocouple, and oxygen sensor data.**



### 3.2.7 Oxygen Analyzer

The oxygen sensor used is model 2D-220 supplied by Centorr Vacuum Industries. The principle behind the sensor is a voltaic cell that measures oxygen concentration. The ratio of the oxygen partial pressures at the two electrodes dictates the magnitude of the cell voltage. The electrolyte in the cell is solid yttria stabilized Zirconium dioxide operated at 800°C, which ensures high mobility of oxygen. The concentration of oxygen in air establishes the potential for the reference electrode, while the concentration in the sample establishes the potential in the second electrode. The difference in potential of these two electrodes is the cell voltage. There is an LCD display that indicates the amount of oxygen in the gas stream by converting the voltage into parts per million units. The quantity of oxygen is determined from the voltage by applying the Nernst Equation.

$$E = \frac{RT}{4F} \log_e \frac{(PO_2 \text{ Air})}{(PO_2 \text{ Sample})} = 0.0496 T \log_{10} \frac{(PO_2 \text{ Air})}{(PO_2 \text{ Sample})} \quad (61)$$

Where E is the voltage in milli-volts, T is temperature in degrees Kelvin and 0.0496 is a constant expressed in millivolts/K. Because the amount of oxygen in the sample is inversely related to the cell voltage, an increase in oxygen content results in a lower voltage in the cell. The oxygen content for each experiment is typically less than 20ppm, corresponding to an output > 150 millivolts. The cell voltage is connected to the data acquisition system and recorded.

### **3.2.8 Procedure for High Temperature Experiments**

1. The crucible is mounted into the frame of the apparatus, where two thermocouples are inserted. From one thermocouple, the temperature is displayed on an LCD display and from the other the temperature is recorded to the data acquisition system. The material to be melted is added to the crucible. The top portion of the shell is bolted to the plate that the crucible rests on.
2. The pan containing  $\text{SiO}_2$  for aluminum and  $\text{MgO}$  for AZ91D alloy rests on the loadcell. The bottom portion of the shell is bolted to the plate. The stopper rod is positioned at the bottom of the orifice plate.
3. Air is evacuated from the unit using the vacuum pump.
4. The vacuum is turned off and argon is pumped into the apparatus until a pressure of 34000 Pa (5psig) is registered.
5. Steps 3 and 4 are repeated to ensure more complete oxygen removal.
6. Once 34000 Pa of argon is exerted on the unit, the purge valve is turned on. The gas flow rate is regulated such that the pressure is held constant despite the presence of a continuous purge.
7. The oxygen content in the unit is monitored until 20ppm is registered on the oxygen sensor. This information is recorded on the data acquisition system every 30 s.
8. Once the oxygen content reaches 20ppm, the induction furnace is turned on. Recall that 20ppm is the minimal oxygen content that the existing apparatus can achieve. Approximately 1 kilowatt ( $\text{Power} = \text{Voltage} \times \text{Current in induction coil}$ )

is applied to the crucible for every 100 °C until the desired temperature is reached. This information is also recorded every 30 s.

9. When the material approaches the desired temperature, the induction power is turned down until the temperature remains steady. The conditions are held for 20 minutes to ensure that the system is stabilized in terms of temperature and oxygen content.
10. When the melt is ready to pour through the orifice, the furnace is turned off. This is important because it eliminates induction stirring that may seriously affect the dynamics of the experiment.
11. Within approximately 10s, the stopper rod is removed and the melt flows from the orifice onto the pan.
12. The loadcell, thermocouple, and oxygen sensor are recorded by the data acquisition system at a sample rate of 5Hz (0.2s). The data is saved to a floppy disk.
13. The data is imported into Excel (Microsoft corporation) where a 2<sup>nd</sup> order polynomial is fitted to the cumulative mass curve versus time data. This function is differentiated to obtain the experimental flow rate at the respective head heights taken every 0.2s.
14. For an initial head height of 0.11m, the time taken to drain through a 0.005m (5mm) orifice is approximately 35 s for molten aluminum (973K-1165K) and AZ91D alloy (921K-1169K).

### **3.3 Conclusions**

Both the low temperature and high temperature equipment is designed to provide conditions where head and flow rate are measured with a minimal amount of uncertainty. The high temperature apparatus efficiently provides heat and atmospheric control, a necessity for such experimentation. By making use of the equipment and procedures, it is possible to calculate the frictional characteristics of the orifice using measurements for head, flow rate, and sound knowledge of the physical properties of melts. This is discussed in detail in Chapter 4. Chapter 5 illustrates how measurements for head, flow rate, and knowledge of the frictional characteristics of the orifice, make it possible to measure the physical properties of a melt.

## **CHAPTER 4: CHARACTERIZATION OF FRICTIONAL LOSSES**

This chapter will present the Bernoulli approach to analyze the fluid dynamics of a stream draining from a vessel. Two models will be presented. The first model under consideration will not include surface tension in the formulation. A second model will account for the surface energy of a stream exiting an orifice. Non-dimensional numbers will be introduced that provide insight into the relative magnitude of forces, a useful analysis in designing similar dynamic systems.

### **4.1 Flow From a Draining Vessel: Neglecting Surface Tension**

For a vessel having an orifice in the bottom, it is assumed that a free jet will form when the vessel is filled with a fluid, and that flow rate is dependent on the head of the fluid. To predict the flow rate, the Bernoulli formulation will be applied. This approach is considered to be macroscopic meaning that exact solutions obtained from these methods are correct “on the average” [80]. The assumptions made in the derivation will be clearly outlined.

#### **4.1.1 Formulation**

Refer to Figure 4.1 for an illustration of unsteady flow through an orifice. The two reference locations under consideration are defined at points 1 and 2.

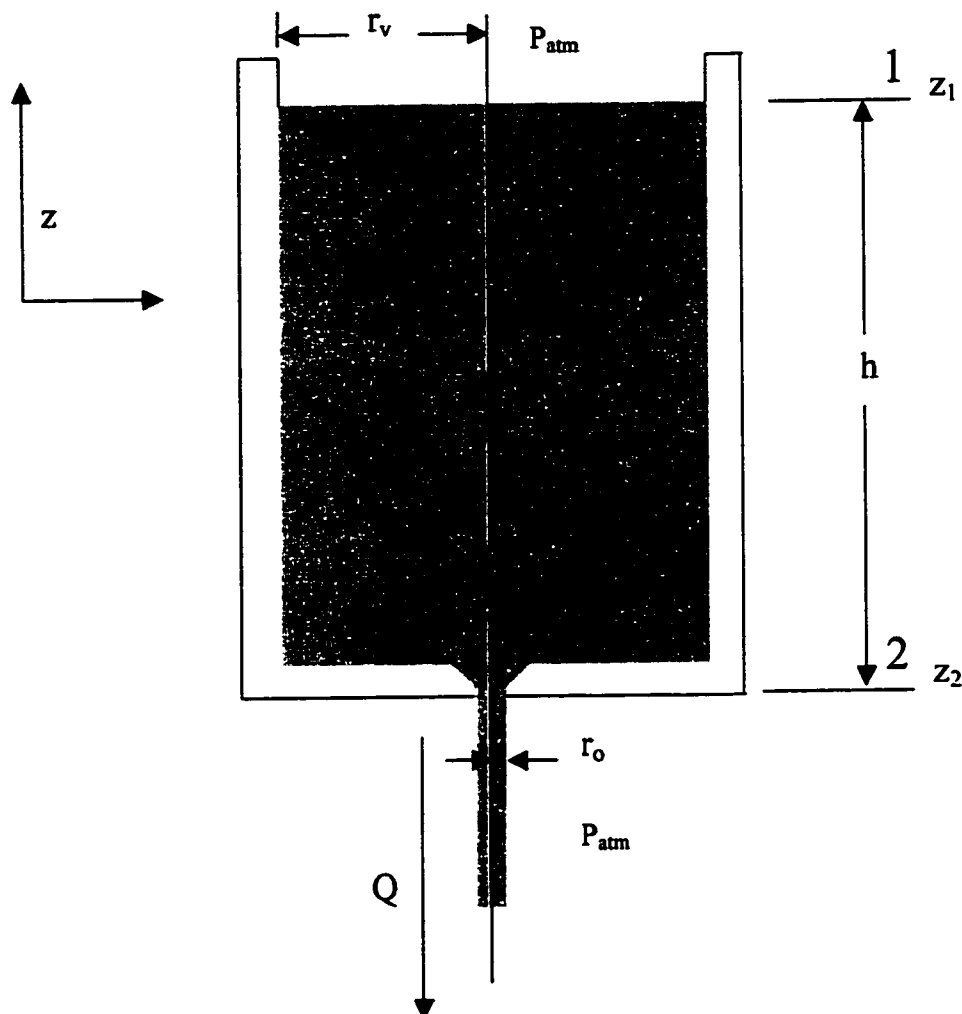


**Figure 4.1: Schematic of draining vessel system depicting flow rate of a fluid through an orifice placed at the bottom.**

### *Bernoulli Approach*

Referring to Figure 4.2, frictionless unsteady flow can be considered along a streamline. Unsteady flow conditions can be considered using this method; however, the moving boundary located at reference point 1 is not considered in this analysis. The forces acting on the small cylindrical element of fluid that acts in the direction of the streamline will be applied along with Newton's second law (i.e.  $F_o = d(mu)/dt$ ). This

formulation is outlined in Daugherty et al. [79]. The Bernoulli equation applied specifically to a draining vessel system has been formulated in Whitaker [80]; however, transient terms were neglected.

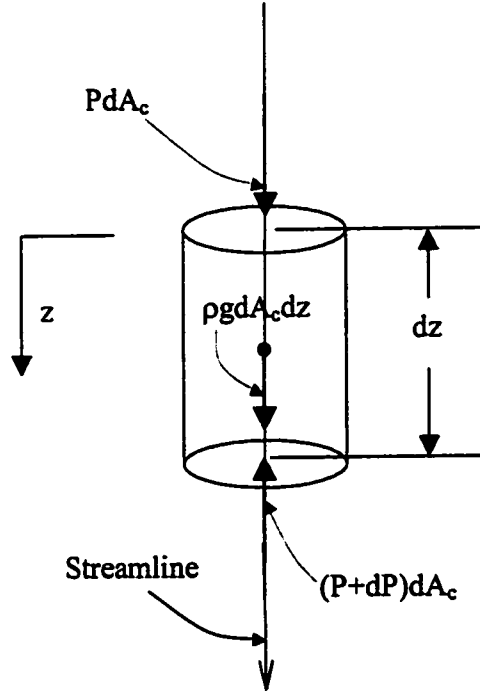


**Figure 4.2: Control element on streamline neglecting frictional losses.**

The forces tending to accelerate the fluid mass are the pressure forces at the ends of the element:

$$PdA_c - (P + dP)dA_c = dPdA_c \quad (62)$$

Where  $P$  is the pressure exerted at the inlet of the element,  $dP$  is the change in pressure across the element and  $A_c$  is the cross sectional area of the element.

The weight of the element in the direction of motion is:

$$mg = \rho g dA_c dz \quad (63)$$

The sum of the forces expressed by Equations (62) and (63) equal the change in momentum of the control element:

$$-dPdA_c + \rho g dA_c dz = \frac{d(mu)}{dt} \quad (64)$$

Daugherty et al. [79] considered the case of unsteady flow (velocity as a function of both position and time). The following relationship is obtained:

$$-dPdA_c + \rho g dA_c dz = m \left( u \frac{\partial u}{\partial z} + \frac{\partial u}{\partial t} \right) \quad (65)$$

Equation (65) can be expressed as:

$$-dPdA_c + \rho g dA_c dz = \rho dA_c dz \left( u \frac{\partial u}{\partial z} + \frac{\partial u}{\partial t} \right) \quad (66)$$

Dividing by  $\rho dA_c$ :

$$\frac{dP}{\rho} - g dz = -dz \left( u \frac{\partial u}{\partial z} + \frac{\partial u}{\partial t} \right) \quad (67a)$$

$$\frac{dP}{\rho} - g dz = -u du - dz \left( \frac{\partial u}{\partial t} \right) \quad (67b)$$

$$\int_1^2 \frac{dP}{\rho} - g \int_1^2 dz + \int_1^2 u du = - \left( \frac{\partial u}{\partial t} \right) \int_1^2 dz \quad (68)$$

The term  $\partial u / \partial t$  is considered to be constant since the relation between velocity and time at reference points 1 and 2 is essentially linear. Refer to Figure A.1 in Appendix A for validation of the linear assumption. Integrating Equation (68) between points 1 and 2 yields:

$$\frac{(P_2 - P_1)}{\rho} - g(z_2 - z_1) + \frac{(u_2^2 - u_1^2)}{2} = - (z_2 - z_1) \left( \frac{\partial u}{\partial t} \right) \quad (69)$$



Note that the formulation has thus far neglected viscosity effects in the derivation. The balance is therefore considered to be valid for inviscid flow only. The frictional effects will be characterized by the discharge coefficient that will be introduced later in this section. The term  $(z_2 - z_1)$  is the head of fluid above the exit of the orifice,  $h$ , as indicated by Figure 4.1. The velocity at point 1 can be expressed as the velocity at point 2 (continuity):

$$u_1 = \frac{r_o^2}{r_v^2} u_2 \quad (70)$$

An assumption is made at this point in the formulation. Since  $r_v \gg r_o$ ,  $u_1 \approx 0$  [79].

Rearranging in terms of outlet velocity,  $u_2$ , yields:

$$u_2 = \sqrt{2g \left( h - \frac{(P_2 - P_1)}{\rho g} - \frac{h}{g} \left( \frac{\partial u}{\partial t} \right) \right)} \quad (71)$$

The term  $h/g(\partial u/\partial t)$  represents the accelerative head term within the vessel [79]. This term is neglected in the final form of the equation. The assumption that the accelerative head term is negligible is validated in Appendix A. Another assumption will be presented at this point. It is assumed that there is no pressure difference between points 1 and 2 (atmospheric pressure at the free surface and orifice tip). In section 4.2, a new formulation will be presented, which states that there is in fact a pressure exerted at point 2 due to the effects of surface tension. Equation (71) becomes:

$$u_2 = \sqrt{2gh} \quad (72)$$

This is the classical expression that relates velocity with head. Since friction is neglected in the formulation,  $u_2$  is considered to be the theoretical maximum velocity at the exit of the orifice.

$$u_{theo} = \sqrt{2gh} \quad (73)$$

Or in terms of maximum theoretical flow rate:

$$Q_{theo} = \pi r_o^2 \sqrt{2gh} \quad (74)$$

A summary of the assumptions made in this formulation are the following:

- 1) The flow is quasi-steady state (validated in Appendix A).
- 2) Viscous dissipation is neglected.
- 3) The velocity at reference point 1,  $u_1$ , is small compared with  $u_2$ .
- 4) The velocity profile at the orifice exit is flat.
- 5) The pressure at the inlet and outlet is atmospheric pressure only (i.e.  $P_1 = P_2$ ).

Equation (74) can be expressed in dimensionless form by introducing the Froude number:

$$Fr = \frac{\text{Inertial Forces}}{\text{Potential Forces}} = \frac{u_{theo}^2}{2gh} = \frac{\left( \frac{Q_{theo}}{\pi r_o^2} \right)^2}{2gh} = 1 \quad (75)$$

The Froude number is always equal to unity in this analysis since viscous losses are neglected.

Next, the discharge coefficient is used to characterize the friction losses in the orifice, and is defined as the ratio between experimental flow rate and theoretical flow rate:

$$C_d = \frac{Q_{exp}}{\pi r_o^2 \sqrt{2gh}} \quad (76)$$

$Q_{exp}$  is defined as the experimental flow rate in units of  $m^3/s$ . Clearly,  $C_d$  must always be less than unity since viscous losses in the orifice result in flow rates less than what is

computed ideally from Equation (74). Note that Equation (76) is dimensionless. The physical significance of the inertial and viscous forces will now be discussed.

The Reynolds number (Re) is introduced to characterize the inertial and viscous forces at the orifice.

$$Re_{exp} = \frac{\text{Inertial Forces}}{\text{Viscous Forces}} = \frac{\rho u_{exp} 2r_o}{\eta} = \frac{2\rho Q_{exp}}{\pi r_o \eta} \quad (77)$$

Where  $\rho$  and  $\eta$  are the density and viscosity of the fluid respectively, and  $u_{exp}$  is experimental fluid velocity.

The next section will calculate the discharge coefficient expressed in Equation (76) for water and ethylene glycol at different temperatures. This quantity will be plotted against Reynolds number so that frictional characteristics in the orifice can be determined.

#### 4.1.2 Results

Ethylene Glycol and Water were used to test the formulation presented in this section using a 0.003m diameter Teflon orifice. The viscosity of these fluids is a strong function of temperature and makes it possible to explore a wide range Reynolds numbers [61]. Refer to section 3.1 for an overview of the methodology for low temperature experimentation. The flow rate was determined from the cumulative mass measured with time by the digital scale (Ohaus GT-8000) and a stopwatch. A video camera recorded the mass and time that was displayed by the instrumentation. The flow rate was calculated by differentiating the cumulative mass curve that was generated. Refer to Figure 4.3 for the cumulative mass of water at 293 K for this system. The 3<sup>rd</sup> order polynomial used to

describe the curve is included on the chart. It was determined that a 3<sup>rd</sup> order polynomial fit sufficiently describes the data and that an increasing polynomial order does not improve accuracy.

The function takes the form:

$$C_{m,poly} = 3.442 \times 10^{-8}(t)^3 - 6.315 \times 10^{-5}(t)^2 + 1.113 \times 10^{-2}(t) + 9.842 \times 10^{-3} \text{ kg} \quad (78)$$

The standard deviation between the data points depicted in Figure 4.3 and the polynomial curve is calculated as follows:

$$\delta C_m = \sqrt{\frac{\sum (C_{m,poly} - C_{m,exp})^2}{n - 4}} = 1.018 \times 10^{-8} \text{ kg} \quad (79)$$

The number of data points, n, is 75.

Equation (78) is differentiated to yield the flow rate on a mass basis, i.e.:

$$\frac{d(C_{m,poly})}{dt} = 3(3.442 \times 10^{-8})(t)^2 - 2(6.315 \times 10^{-5})(t) + 1.113 \times 10^{-2} \text{ kg/s} \quad (80)$$

Head was determined through visual observation and recorded on video as well. Flow rate and head were used in Equation (76) to calculate the discharge coefficient. Head is illustrated as a function of time in Figure 4.4. The scale used for visual observations is accurate to 0.0005m.

Results from this analysis are represented in Figure 4.5. Each liquid exhibits different frictional characteristics, as Figure 4.5 indicates. The formulation presented in the last section is reinvestigated in the next section to explain this behavior. By accounting for other forces such as surface tension effects, it will be observed that a different relationship is generated for the discharge coefficient and Reynolds number analysis.

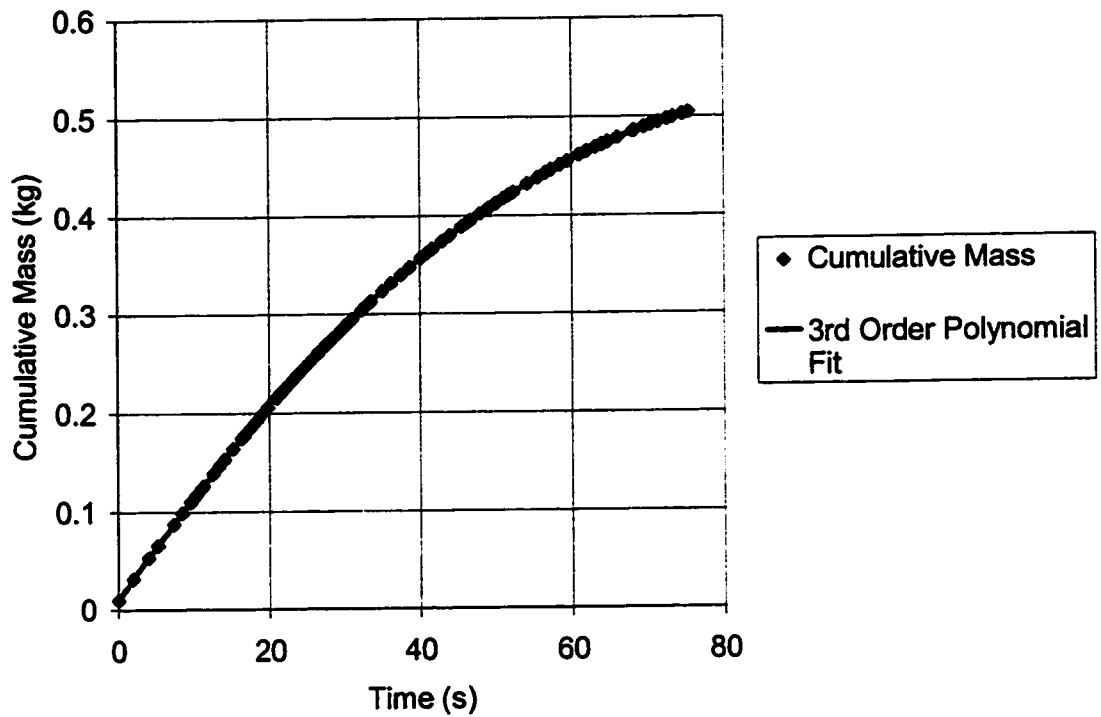


**Figure 4.3: Cumulative mass versus time for water at 293 K through 0.003m Teflon orifice plate from an initial head of approximately 0.17m.**

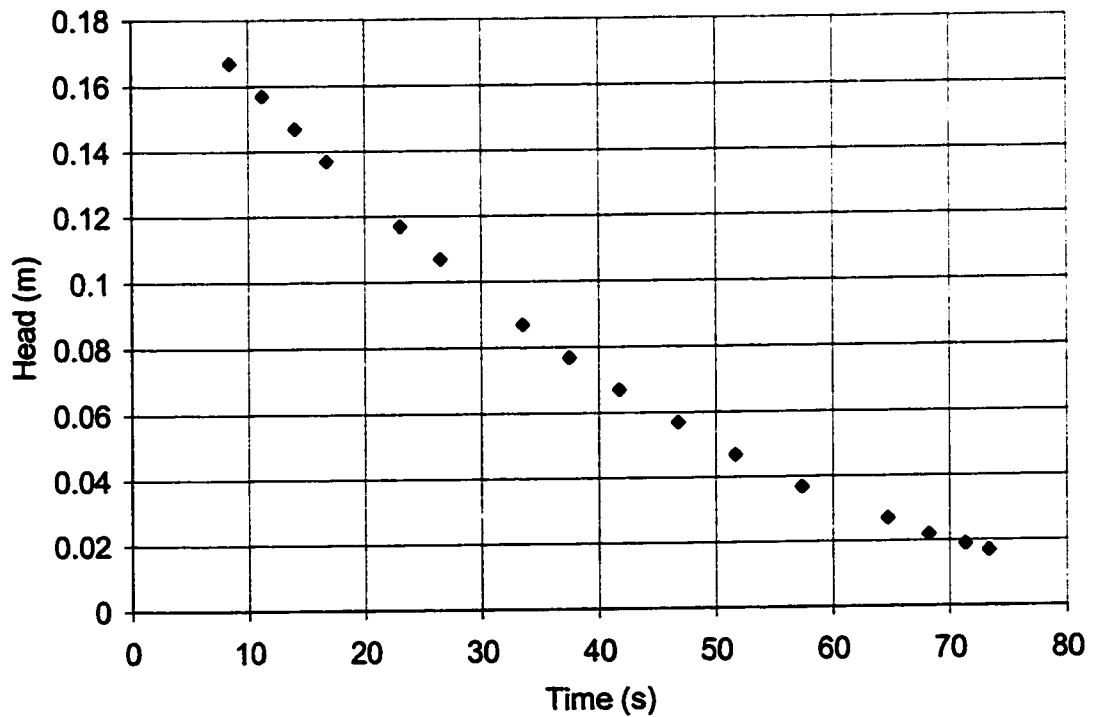


**Figure 4.4: Head versus time for water at 293 K through a 0.003m Teflon orifice plate from an initial head of approximately 0.17m.**

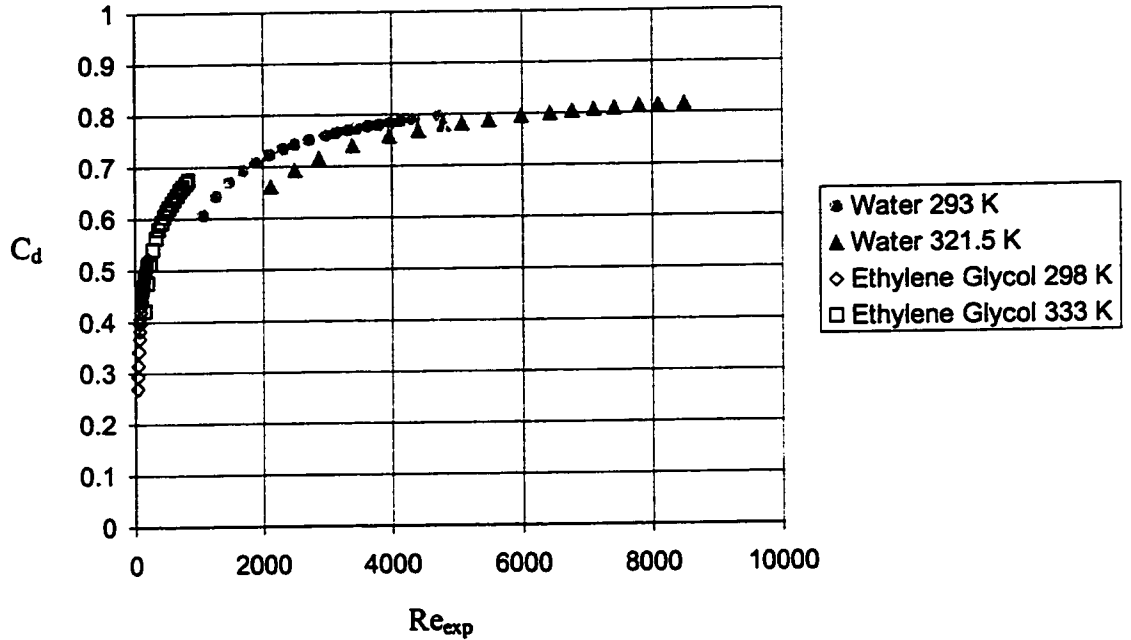


**Figure 4.5:**  $C_d$  versus  $Re_{exp}$ , calculated using Equation (76) for a 0.003m diameter orifice draining under the influence of gravity. Ethylene glycol and water are presented at different temperatures.

## 4.2 Flow From a Draining Vessel: A New Approach

The formulation presented in section 4.1 did not consider pressure effects at reference points 1 and 2 in Figure 4.1. The same system will be considered in this discussion; however, pressures induced from the effects of surface tension will be considered as well. The new formulation will be tested and validated using the discharge coefficient versus Reynolds number characterization using the same experimental data that was used to generate Figure 4.5. Finally, a new dimensionless number will be defined called the Bond number that indicates the magnitude of surface forces in the

system. This quantity assists in outlining the experimental set of conditions that result in significant effects due to surface tension.

#### 4.2.1 Formulation

Pressure that is induced by surface tension occurs at curved interface separating the liquid from the atmosphere. This occurs just below reference point 2 on Figure 4.1. The Laplace equation relates the pressure difference across a curved interface to the radii of curvature:

$$\Delta P = \sigma \left( \frac{1}{R_{\text{curve}^a}} + \frac{1}{R_{\text{curve}^b}} \right) \quad (81)$$

$\Delta P$  is the pressure difference across the liquid/gas interface, and  $R_{\text{curve}^a}$  and  $R_{\text{curve}^b}$  represent the radii of curvature that describes the shape of the surface. If there is a planar surface,  $R \rightarrow \infty$ , and there is no pressure induced as Equation (81) indicates.

At reference point 1 (top of the liquid in the vessel), it is assumed that the pressure induced is negligible since the interface is considered to be planar ( $R_{\text{curve}^a}$  and  $R_{\text{curve}^b}$  approach infinity).

Directly below reference point 2 (orifice tip), the stream exiting the orifice is essentially cylindrical with the curvatures illustrated in Figure 4.6. At a location just below the orifice (where the stream is first in contact with the atmosphere),  $R_{\text{curve}^a}$  is taken to be the radius of the orifice,  $r_o$ . The second radius of curvature,  $R_{\text{curve}^b}$  is assumed to be infinity since the stream is assumed to be a perfect cylinder at this location.

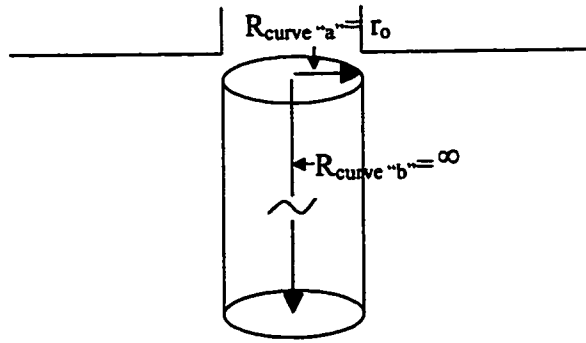


**Figure 4.6: Radius of curvature defining the gas-liquid interface of a free jet.**

From the Laplace equation, the pressure induced due to the effects of surface tension directly below the orifice is:

$$\Delta P = \sigma \left( \frac{1}{r_o} \right) \quad (82)$$

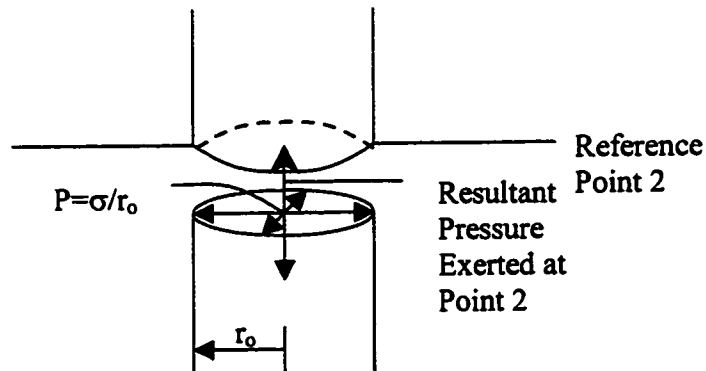


**Figure 4.7: Pressure acting at orifice tip for a stream of liquid exposed to the atmosphere.**

Considering Equation (71), and assuming quasi-steady state conditions, an added pressure at reference point 2 is included in the formulation that corresponds to a magnitude of  $\sigma / r_o$ .



$$u_2 = \sqrt{2g \left( h - \frac{(P_2 - P_1)}{\rho g} \right)} = \sqrt{2g \left( h - \frac{\left( \frac{\sigma}{r_o} + P_{atm} - P_{atm} \right)}{\rho g} \right)} = \sqrt{2g \left( h - \frac{\sigma}{\rho g r_o} \right)} \quad (83)$$

$P_1$  is taken to be atmospheric pressure only because the free surface is considered to be planar, which indicates no effects of surface tension. Equation (83) is considered to represent the theoretical maximum velocity since frictional losses are not considered at this point.

$$u_{theo} = \sqrt{2g \left( h - \frac{\sigma}{\rho g r_o} \right)} \quad (84)$$

Or in terms of maximum theoretical flow rate:

$$Q_{theo} = \pi r_o^2 \sqrt{2g \left( h - \frac{\sigma}{\rho g r_o} \right)} \quad (85)$$

By rearranging Equation (85), it is possible to obtain the relative magnitudes of the inertial, gravitational, and surface forces in a dimensionless format. This is useful in determining the relative magnitude of these forces.

$$\frac{\left( \frac{Q_{theo}}{\pi r_o^2} \right)^2}{2gh} = 1 - \frac{\sigma}{\rho g r_o h} \quad (86)$$

$$\frac{u_{theo}^2}{2gh} = 1 - \frac{\sigma}{\rho g r_o h} \quad (87)$$

The Froude number appears on the left hand side of Equation (87). We now define the Bond number as:

$$Bo = \frac{\text{Potential Forces}}{\text{Surface Forces}} = \frac{\rho g r h}{\sigma} \quad (88)$$

Equation (87) can be expressed as the summation of the Froude number and reciprocal of the Bond number:

$$Fr + 1/Bo = 1 \quad (89)$$

Similar to the analysis in section 4.1, the discharge coefficient is calculated using Equation (85) and the experimental flow rate.

$$C_d = \frac{Q_{exp}}{\pi r_o^2 \sqrt{2g \left( h - \frac{\sigma}{\rho g r_o} \right)}} \quad (90)$$

Similar to Section 4.1.2, in the next section will calculate the discharge coefficient expressed in Equation (90) will be calculated for water and ethylene glycol at different temperatures. Equation (90) will be plotted against Reynolds number so that the frictional characteristics in the orifice can be determined.

#### 4.2.2 Results

The surface tension of ethylene glycol and water was required for this analysis [61,63]. The results are presented in Figure 4.8. The trends of each liquid appear to follow, more consistently, a dependence on Reynolds number. There is a transition zone that is estimated to be approximately between  $300 < Re < 3000$ . Laminar flow is likely characterized by the portion that approaches the origin on the y-axis. The turbulent regime ( $Re > 2000$ ) appears to have a slight slope. Chapter 6 will provide further insight into the turbulent regime in the discussion of experimental viscosity results.

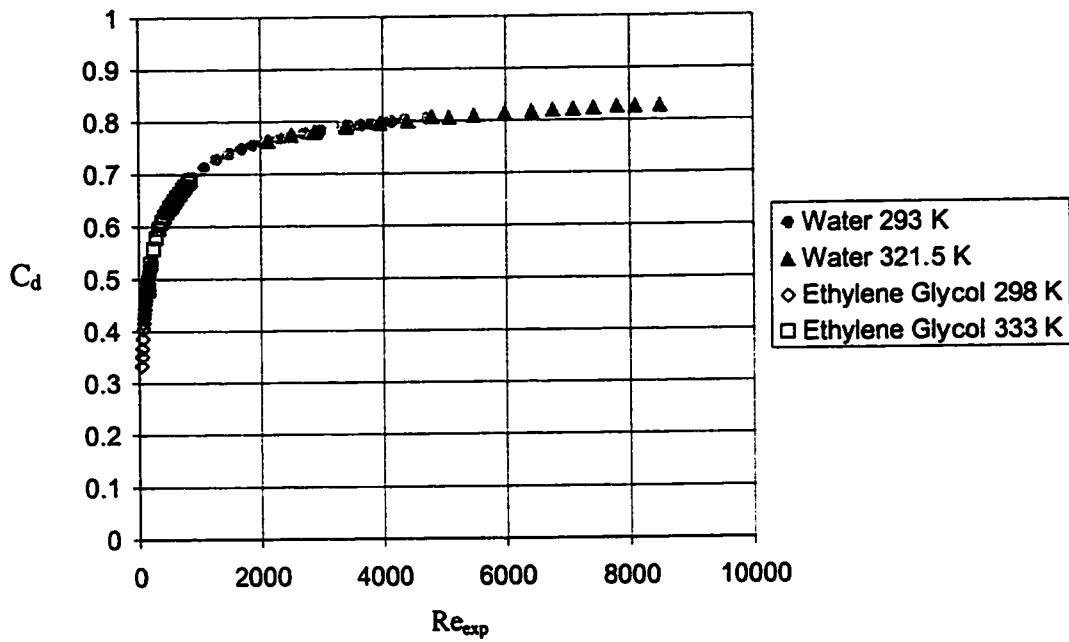


**Figure 4.8:  $C_d$  versus  $Re_{exp}$ , calculated using Equation (90) for a 0.003m diameter orifice draining under the influence of gravity. Ethylene glycol and water are presented at different temperatures.**

### 4.3 Considerations for High Temperature Fluids

In quantifying surface energy in the momentum balance, the use of dimensionless numbers can be insightful in terms of identifying for which systems and under what conditions this new formulation should be considered. Inspection of Equation (89) indicates that as reciprocal of the Bond numbers increases, the Froude number must decrease since the sum of these numbers must equal unity. A small Bond number is indicative of a system where surface energy is playing a significant role. The following criterion is proposed concerning this issue:

- 1) As  $1/Bo \rightarrow 0$  for a particular system,  $Fr \rightarrow 1$ . By inspection of Equations (75) and (89), flow rate and the frictional characteristics can be reasonably approximated using the classic approach outlined in section 4.1.
- 2) When  $1/Bo \rightarrow 1$ , then  $Fr \rightarrow 0$ . This result confirms the necessity to account for surface tension using the newly developed approach outlined in section 4.2.
- 3) When  $1/Bo > 1$ ,  $Fr < 0$  meaning that continuous flow has stopped and that a different formulation is required to describe throughput (i.e. dripping supplied by capillary action).

Through proper examination of the Bond number, it is possible to determine when surface energy is expected to play a significant role for a particular system. For instance, fluids with a relatively large surface tension to density ratio exhibit fluid dynamic behavior in which surface forces are significant because surface tension appears in the denominator and density appears in the numerator. Also, surface tension is expected to exhibit greater influence on the system when a relatively small orifice is used. Finally, and during the course of an experiment as head conditions get lower, surface forces increase in relative magnitude since head appears in the numerator as well.

Densities of molten metals are known to be higher than those of fluids such as water and a variety of organic fluids. Also, molten metals have considerably higher surface tension values than low temperature fluids such as water and organic liquids. This has been discussed in Chapter 2. The influence of the density-surface tension ratio on the magnitude of the Bond number is obvious when comparing water and aluminum systems. Data collected for these systems is presented in Figure 4.9 for a 0.005m diameter orifice design. It is immediately evident that the aluminum system is influenced

to a greater extent by surface forces. This is due to the fact that aluminum's density-surface tension ratio is 5.5 times less than it is for water ( $\rho_{H_2O} = 988 \text{ kg/m}^3$ ,  $\sigma_{H_2O} = 0.069 \text{ N/m}$  at 313 K [61];  $\rho_{Al} = 2300 \text{ kg/m}^3$  [2],  $\sigma = 0.83 \text{ N/m}$  [7] at 1173 K). Head conditions corresponding to the water data vary between 0.13 and 0.01m. For aluminum the conditions varied between 0.12 and 0.02m.

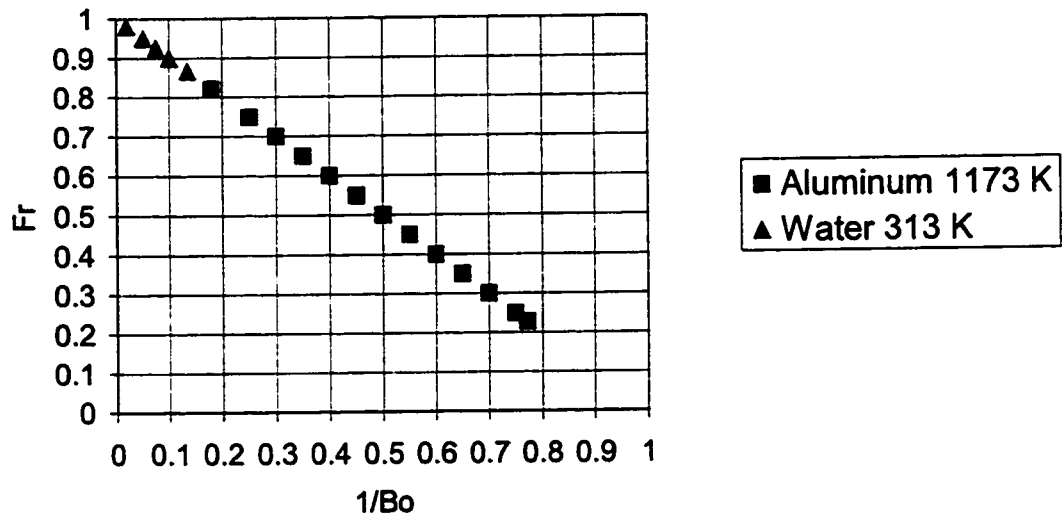


**Figure 4.9: Dependence of the Bond and Froude relation on the density-surface tension ratio.**

Figure 4.10 illustrates the magnitude of the Bond number for a variety of fluids. The head and orifice radius were hypothetically chosen at 0.01m and 0.004m respectively because these design parameters realistically ensure that a full scale Fr vs. Bo curve is observed. Molten systems point to the fact that Bond numbers vary significantly depending on the metal that is used. Mercury and lead are the only metals on this chart that are within the same range as water and other organic fluids. Note that for other values of head and orifice areas, only the magnitude of Fr and Bo will vary along the same line shown in Figure 4.10.

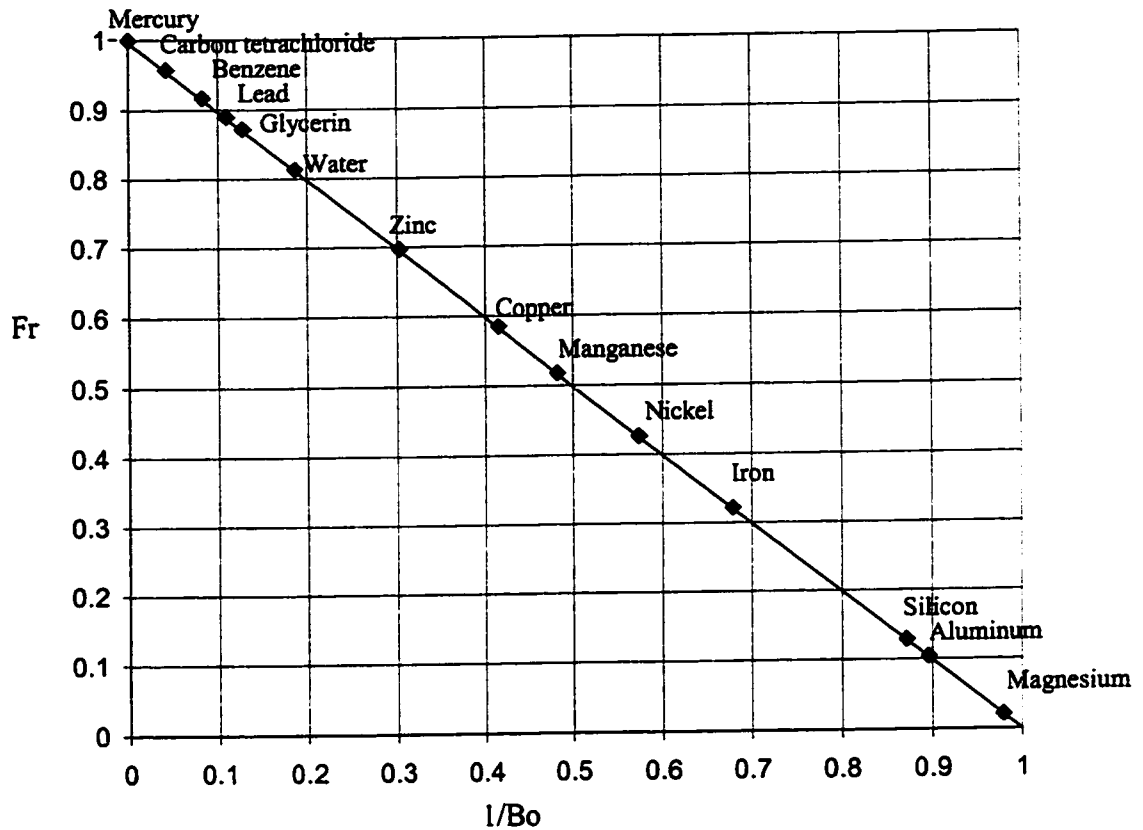


**Figure 4.10: Relative magnitude of Bond numbers for a variety of liquids. Density and surface tension are obtained from Iida and Guthrie [2].**

From a design perspective, the following formulation can be very useful. By taking the ratio of Equations (84) and (73), Equation (91) is obtained:

$$\left( \frac{u_{theo,\sigma}}{u_{theo,no\sigma}} \right) = \frac{\sqrt{2g \left( h - \frac{\sigma}{\rho g r_o} \right)}}{\sqrt{2gh}} = \frac{\sqrt{2gh} \sqrt{1 - 1/Bo}}{\sqrt{2gh}} = \sqrt{1 - 1/Bo} \quad (91)$$

For any processing condition, and if reliable property data is available, one can determine the flow regime that would be appropriate to consider before experiments are performed, thus enabling the appropriate formulation to be utilized. The value computed from Equation (91) is an indication of the discrepancy if the effect of surface tension on

pressure at the outlet is neglected in the formulation. If Equation (91) approaches unity, it is more reasonable to neglect surface energy in the formulation. Figures 4.11, 4.12, and 4.13 illustrate the discrepancies for head conditions between 0.1 and 0.01m for water, iron and aluminum systems respectively. These conditions are based on constant head operation. The properties of water were taken at 293 K [61] and those of molten aluminum and iron at the melting points [2,7]. The results confirm the significant dependency on surface energy many melts exhibit relative to low temperature fluids such as water. For instance, if a head of 0.05m (50cm) is utilized with a specified discrepancy of 0.90, Figures 4.12 and 4.13 indicate that the radius must be in excess of 0.0030m (3.0mm) and 0.004 (4.0mm) for iron and aluminum respectively. When water is considered, the orifice radius must only be in excess of 0.0007m (0.7mm). For the same experimental conditions, molten metals have a higher value of  $1/Bo$  than low temperature organic liquids. Unfortunately, the density and surface tension of these liquids are often unknown.

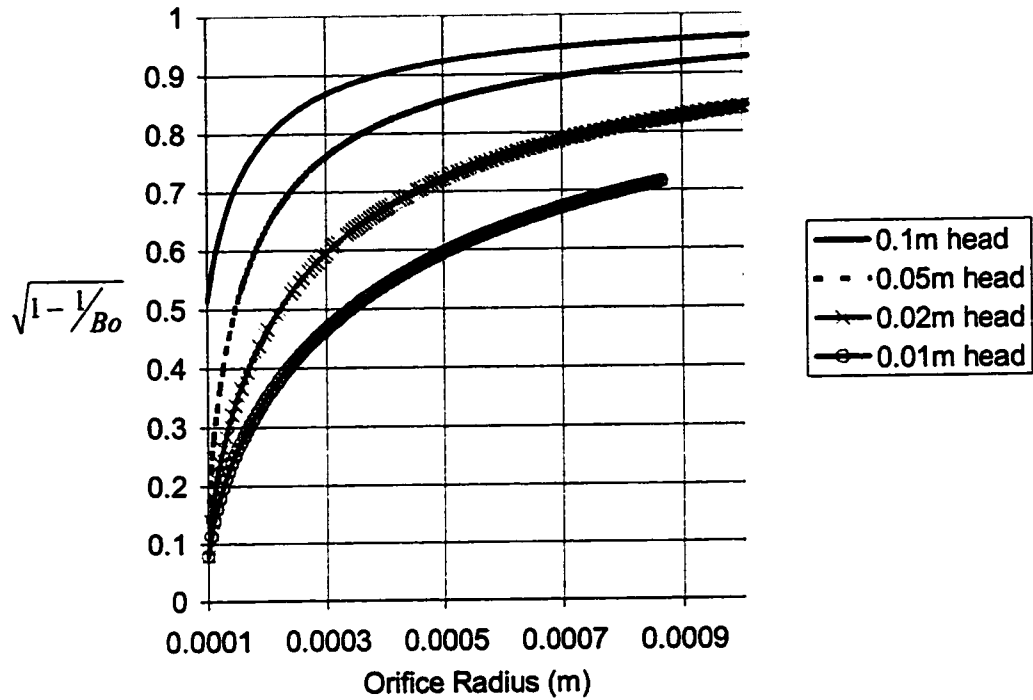


**Figure 4.11: Water: Accuracy in neglecting surface energy for variable orifice design for heads ranging from 0.1m to 0.01m.**

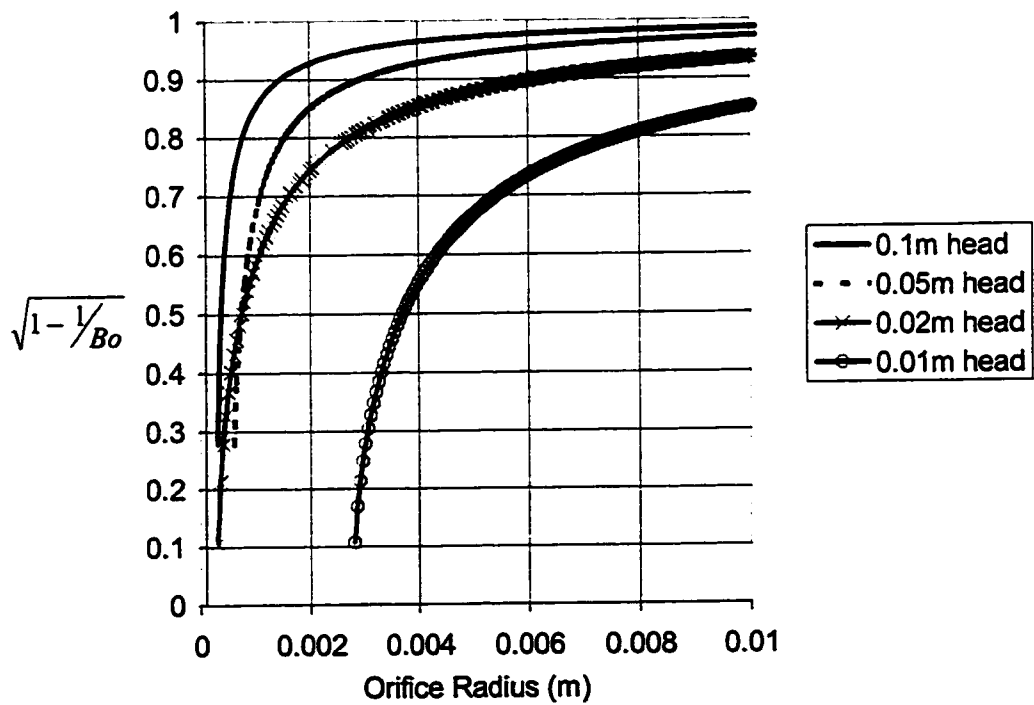


**Figure 4.12: Molten iron: Accuracy in neglecting surface energy for variable orifice design for heads ranging from 0.1m to 0.01m.**



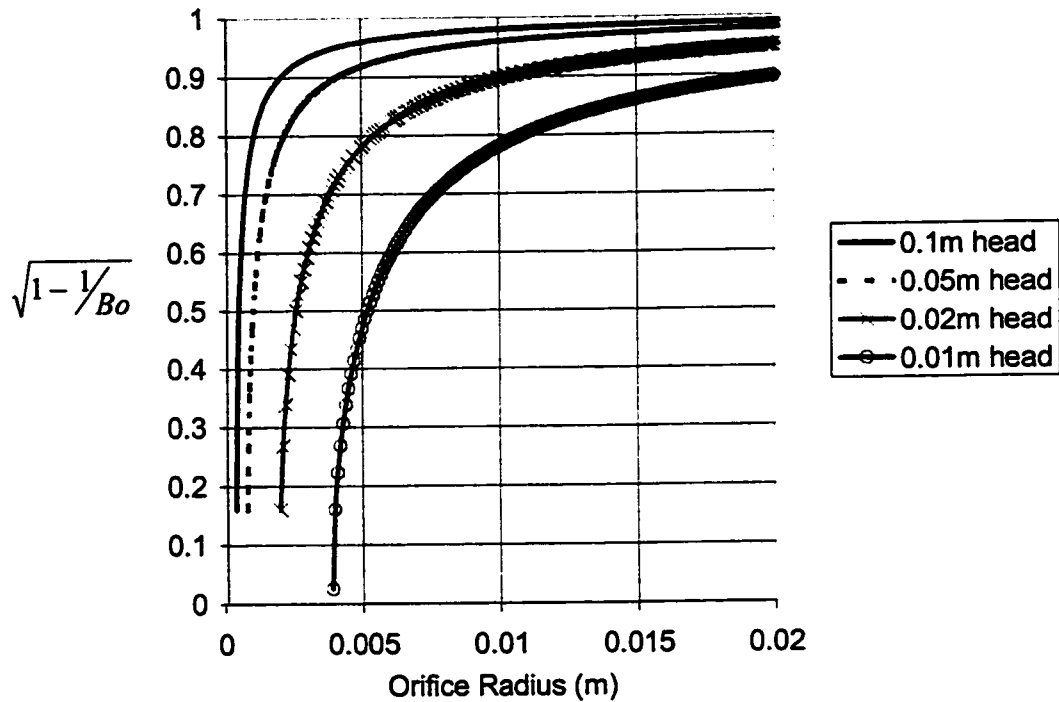


**Figure 4.13: Molten aluminum: Accuracy in neglecting surface energy for variable orifice design for heads ranging from 0.1m to 0.01m.**

#### 4.4 Conclusions

The case of a fluid draining through an orifice is not a trivial problem that is solved by accounting only for potential and inertial forces. In order to properly characterize frictional losses in the system, conditions may exist where surface tension must be implemented in the analysis. These conditions exist when, in relative terms, fluid head and orifice radius are small; and surface tension to density ratio is large. These conditions are addressed in the Bond number, which can be useful from a design standpoint in determining whether or not surface tension should be included in the

analysis. This approach is most relevant for molten metal systems where surface forces are known to be significant, and points to yet another example of the necessity to expand the current available data of the liquid properties of high temperature systems. In the next chapter, it will be shown how this formulation can be used to calculate the physical properties such as surface tension, viscosity and density. This is accomplished, however, once the frictional characteristics of the orifice are quantified and calibrated using the analysis described in this chapter. Through proper calibration of the discharge coefficient-Reynolds number relationship, the properties of liquids, in particular melts, can be determined by measuring flow rate and head.

## **CHAPTER 5: FORMULATION OF PHYSICAL PROPERTY MEASUREMENTS**

In this chapter, a formulation will be presented that calculates the physical properties of melts. A calibration relating discharge coefficient with Reynolds number, coupled with experimental flow rate and head measurements, facilitates these measurements because surface tension, viscosity and density are inherently part of the formulation developed in Chapter 4. An approach to measure surface tension for systems where density and viscosity are known will be formulated and validated using systems involving water. This is a useful exercise in analyzing the sensitivity of the calculation when low temperature liquids are used. By implementing non-linear regression techniques it will be illustrated how surface tension, density, and viscosity can be determined simultaneously using data collected from one experiment. This is relevant when dealing with molten systems because it is often encountered that more than one physical property is unknown. Molten aluminum is used in this analysis to validate the model. A rigorous error analysis is performed that identifies various sources of error and predicts the uncertainties expected in the results. This is useful in determining for which fluids, and under what conditions accurate measurements can be performed.

### **5.1 Formulation of Surface Tension Measurements: Fluids with Known Density and Viscosity**

As explained in section 2.1.4, techniques that measure surface tension are typically the product of a force balance in which surface forces play a significant role.

By rearranging Equation (90), an expression for surface tension as a function of experimental flow rate, head, and discharge coefficient is obtained:

$$\sigma = \rho g r_o \left[ h - \frac{1}{2g} \left( \frac{Q_{\text{exp}}}{C_d \pi r_o^2} \right)^2 \right] \quad (92)$$

A draining vessel system offers a distinct advantage compared with other techniques. Conditions of flow rate, head, and discharge coefficient change continuously during the course of one experiment. Consequently, by draining the vessel, a number of measurements can be made due to the variable conditions.

This new method for determining surface tension is based on the calibration of frictional losses in the orifice described by  $C_d$ . This is accomplished using fluids of known properties for which under varying conditions of head and flow, a relationship between discharge coefficient and Reynolds number can be determined. A 3<sup>rd</sup> order polynomial was chosen to describe the discharge coefficient curve.

$$\sigma = \rho g r_o \left[ h - \frac{1}{2g} \left( \frac{Q_{\text{exp}}}{(a \text{ Re}^3 + b \text{ Re}^2 + c \text{ Re} + d) \pi r_o^2} \right)^2 \right] \quad (93)$$

For the work performed with water presented in section 5.1.3, it was determined that an increase in the polynomial order did not result in an improved fit to the experimental data (for  $1000 < \text{Re} < 5500$ ). Refer to Section 3.1.1 for this particular orifice design. For molten aluminum, it will be revealed in section 5.2.2 that a linear approximation sufficiently describes the discharge coefficient for  $4000 < \text{Re} < 13000$  and that constants  $a$  and  $b$  are set to zero. Note that the discharge coefficient-Reynolds number relationship is not considered to be linear. Certain portions of the curve, however, can be approximated to be so. It will be revealed in Section 5.2.1, with the introduction of

multiple non-linear regression analysis, that this approach results in a simple computational technique compared with a higher order polynomial fit. The orifice design for the aluminum work is referenced in Section 3.2.1. Equation (93) can be written in terms of  $Q_{\text{exp}}$ ,  $\rho$ ,  $\eta$  and the polynomial constants, a b, c and d as follows:

$$\sigma = \rho g r_o \left[ h - \frac{1}{2g} \left( \frac{Q_{\text{exp}}}{\left( a \left( \frac{2\rho Q_{\text{exp}}}{\pi r_o \eta} \right)^3 + b \left( \frac{2\rho Q_{\text{exp}}}{\pi r_o \eta} \right)^2 + c \left( \frac{2\rho Q_{\text{exp}}}{\pi r_o \eta} \right) + d \right) \pi r_o^2} \right)^2 \right] \quad (94)$$

### 5.1.1 Error Analysis

Errors in head, flow rate, and discharge coefficient will all contribute to the error in the calculation of surface tension. The propagation of uncertainties is used to determine the effects and is written as follows [64]:

$$\delta\sigma = \sqrt{\left( \frac{\partial\sigma}{\partial h} \right)^2 (\delta h)^2 + \left( \frac{\partial\sigma}{\partial Q_{\text{exp}}} \right)^2 (\delta Q_{\text{exp}})^2 + \left( \frac{\partial\sigma}{\partial C_d} \right)^2 (\delta C_d)^2} \quad (95)$$

The value  $\delta\sigma$  is the expected deviation in surface tension. Quantities,  $\delta h$ ,  $\delta Q_{\text{exp}}$ , and  $\delta C_d$  represent the standard deviations of head, flow rate and discharge coefficient respectively.

The differentials in Equation (95) are determined by taking the derivative of Equation (92) with respect to  $h$ ,  $Q_{\text{exp}}$ , and  $C_d$ . These relationships are represented in Equations (96-98): The derivative of Equation (92) with respect to  $h$  is:

$$\frac{\partial \sigma}{\partial h} = \rho g r_o \quad (96)$$

The derivative of Equation (92) with respect to  $Q_{exp}$  is:

$$\frac{\partial \sigma}{\partial Q_{exp}} = -\frac{\rho r_o}{C_d \pi r_o^2} \left( \frac{Q_{exp}}{C_d \pi r_o^2} \right) = -\frac{\rho r_o u_{theo}}{C_d \pi r_o^2} = -\frac{\rho \sqrt{2ghFr}}{C_d \pi r_o} \quad (97)$$

(Recall from Equation (75) that  $u_{theo} = \sqrt{2ghFr}$ )

The derivative of Equation (92) with respect to  $C_d$  is:

$$\frac{\partial \sigma}{\partial C_d} = \frac{\rho r_o}{C_d} \left( \frac{Q_{exp}}{C_d \pi r_o^2} \right)^2 = \frac{\rho r_o u_{theo}^2}{C_d} = \frac{2\rho g r_o h Fr}{C_d} \quad (98)$$

### *Errors in Head*

Referring to Equation (96), uncertainties in head will produce a deviation in surface tension proportional to the product of  $\rho$ ,  $g$ , and  $r_o$ . This indicates that low-density fluids and small orifice sizes are favorable in terms of accuracy of the surface tension calculation. The derivative is independent of processing variables  $h$ ,  $Q_{exp}$ , and  $C_d$  and indicates the errors in the measurement would be constant for any set of processing conditions.

### *Errors in Flow Rate*

In the presence of errors in flow rate, Equation (97) indicates that decreasing head, results in decreasing error in the calculation. Low-density liquids are preferable, as are large orifice radii. Also, large discharge coefficients are favorable in minimizing the effects of error in flow rate.

### *Errors in Discharge Coefficient*

Similar to errors in flow rate, diminishing head conditions and large discharge coefficients improve the accuracy of the calculation from analysis of Equation (98).

Small orifice designs and low-density liquids are more favorable as well. By rearranging Equation (98), an acceptable deviation with respect to a deviation in discharge coefficient ( $\partial\sigma/\partial C_d$ ) can be imposed such that head never exceeds the following level:

$$h < \left( \frac{\partial\sigma}{\partial C_d} \right) \frac{C_d}{2\rho g r_o Fr} \quad (99)$$

This constraint will be put into practice in Section 5.1.3.

### 5.1.2 Data Analysis

Tests with water at 321.5 K were conducted to assess the feasibility of measuring surface tension. Refer to Section 3.1 in Chapter 3. The 0.003m diameter Teflon orifice plate was used. The cumulative mass was measured using the Ohaus GT-8000 scale and a stopwatch. A video camera was directed at the scale and stopwatch to record the mass and time. The flow rate was determined by differentiating the cumulative mass curve that was generated using a 2<sup>nd</sup> order polynomial fit to the experimental data. Head was determined through visual observation and recorded on video as well. Four calibrations were used to determine the polynomial constants a, b, c, and d required in Equation (93) and (94). This was done using water at room temperature as a calibration fluid. The density and viscosity of water at 293 K are 998 kg/m<sup>3</sup> and 1.002x10<sup>-3</sup> Ns/m<sup>2</sup> respectively [61]. At an elevated temperature of 321.5 K, the density is 988 kg/m<sup>3</sup> and the viscosity is significantly less at 5.86x10<sup>-4</sup> Ns/m<sup>2</sup> [61]. This corresponds to a decrease in viscosity of 41.5% resulting in operation at higher Reynolds numbers. With reliable physical property data and consistent calibrations, the surface tension of water at 321.5 K is to be

calculated at any set of conditions, provided that Equation (92) properly quantifies surface tension.

### *Measuring Head*

Figure 5.1 illustrates head measurements that were taken at the respective times. A 2<sup>nd</sup> order polynomial relation was fitted to the data as illustrated. It was determined that increasing the order of the polynomial fit did not improve the accuracy of the fit. Error in head measurements can be represented by the standard deviation that is calculated between experimental numbers and the mathematical function. The curve takes the following form:

$$h_{poly} = 2.29 \times 10^{-5} (t)^2 - 4.17 \times 10^{-3} (t) + 1.95 \times 10^{-1} \quad (\text{m}) \quad (100)$$

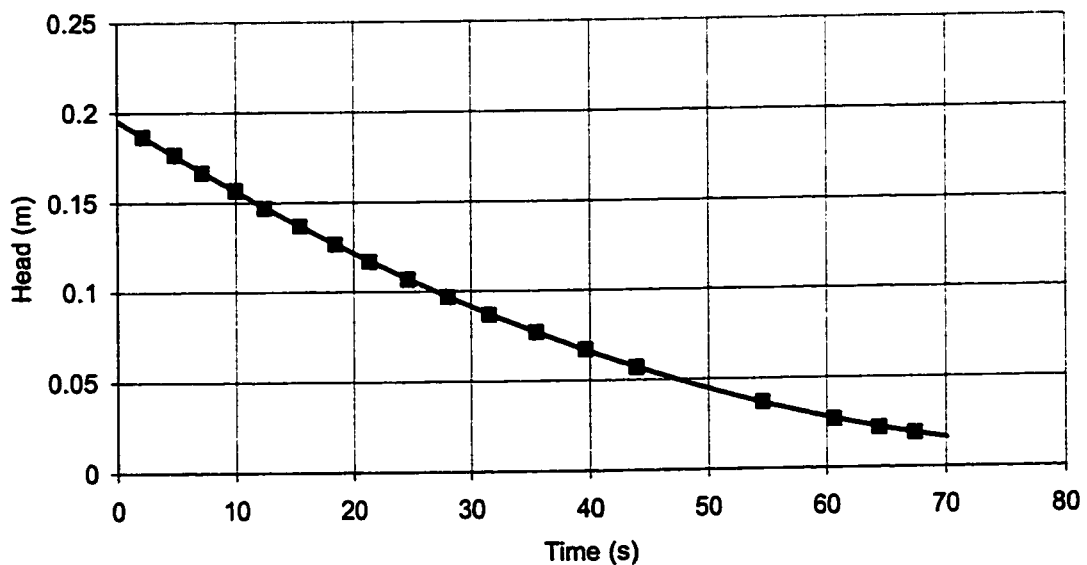


**Figure 5.1: Experimental Head measurements for water at 321.5 K.**

The standard deviation of Equation (100) with respect to the experimental data points presented in figure 5.1 is:



$$\delta h = \sqrt{\frac{\sum (h_{poly} - h_{exp})^2}{n-3}} = 1.53 \times 10^{-4} m \quad (101)$$

The quantity,  $n$ , represents the number of data points. Due to the nature in which head was measured, the error represented by the standard deviation is “random” and means that each experimental data point has an equal possibility of producing either a positive or negative deviation. When measuring head with a linear scale measuring length, random behavior is encountered because values often have to be interpolated. This results in equal possibilities of either underestimating or overestimating the true dimension. Figure 5.2 illustrates the random deviations.

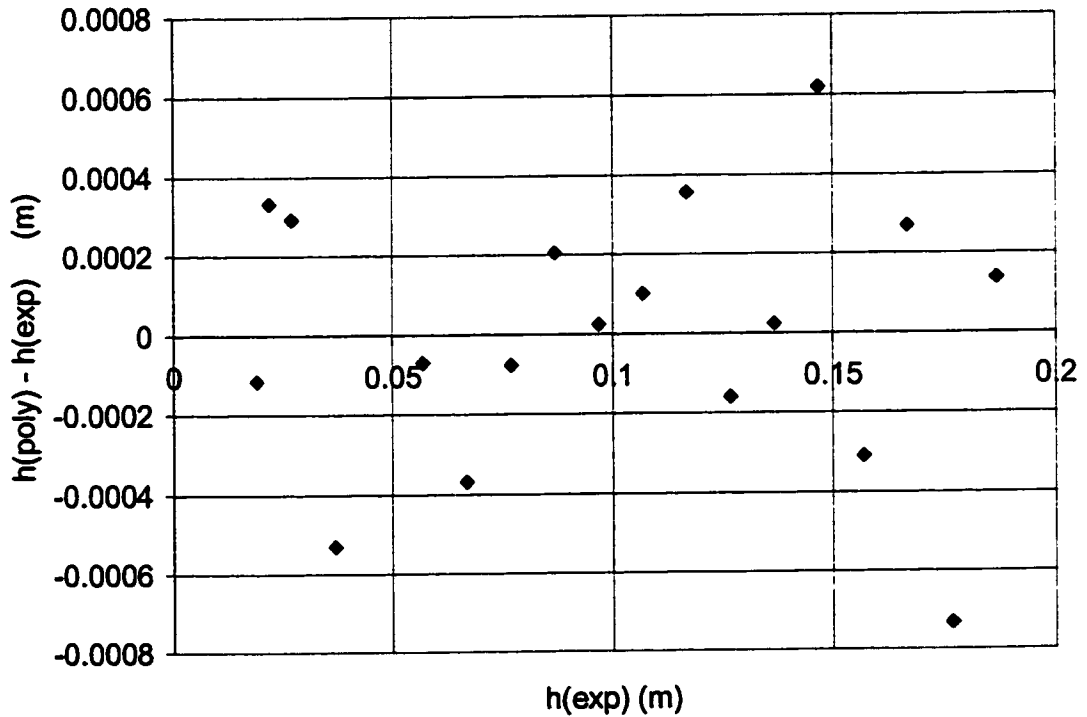


**Figure 5.2: Deviations between experimental head and calculated head for water at 321.5 K.**

### Measuring Flow Rate

The cumulative mass curve is illustrated in Figure 5.3. Unlike relating head with time, the instantaneous flow rate is produced indirectly by analytically differentiating the 2<sup>nd</sup> order polynomial curve that was determined to fit the data reasonably.

$$C_{m,poly} = -6.228 \times 10^{-5}(t)^2 - 1.113 \times 10^{-2}(t) + 1.246 \times 10^{-3} \text{ kg} \quad (102)$$

The standard deviation depicted in Figure 5.3 is:

$$\delta C_m = \sqrt{\frac{\sum (C_{m,poly} - C_{m,exp})^2}{n-3}} = 4.0 \times 10^{-4} \text{ kg} \quad (103)$$

The flow rate is:

$$\frac{dC_{m,poly}}{dt} = -1.246 \times 10^{-4}(t) - 1.113 \times 10^{-2} \text{ kg/s} \quad (104)$$

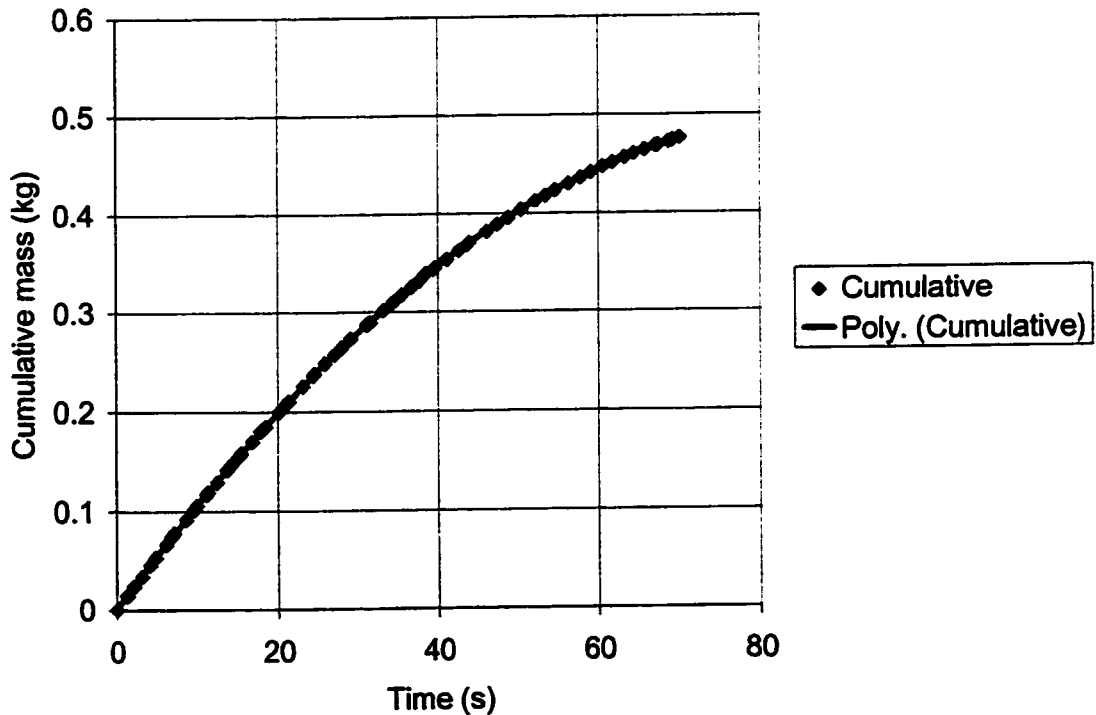


**Figure 5.3: Cumulative mass as a function of time for water at 321.5 K through a 0.003m diameter Teflon orifice.**

Errors associated with flow rate are of a different type than the random errors exhibited in Figure 5.2, since they are considered “systematic” in nature. An analytical expression is used to determine the flow rate, which is an approximation to the actual flow rate. Errors in the formula are systematic because they take the form of entire shifts in magnitude rather than random deviations. Consequently, systematic errors produce erroneous data that is not easily recognized.

### *Measuring Discharge Coefficient*

Figure 5.4 illustrates  $C_d$  as a function of  $Re_{exp}$  determined for four different calibration tests of the orifice.

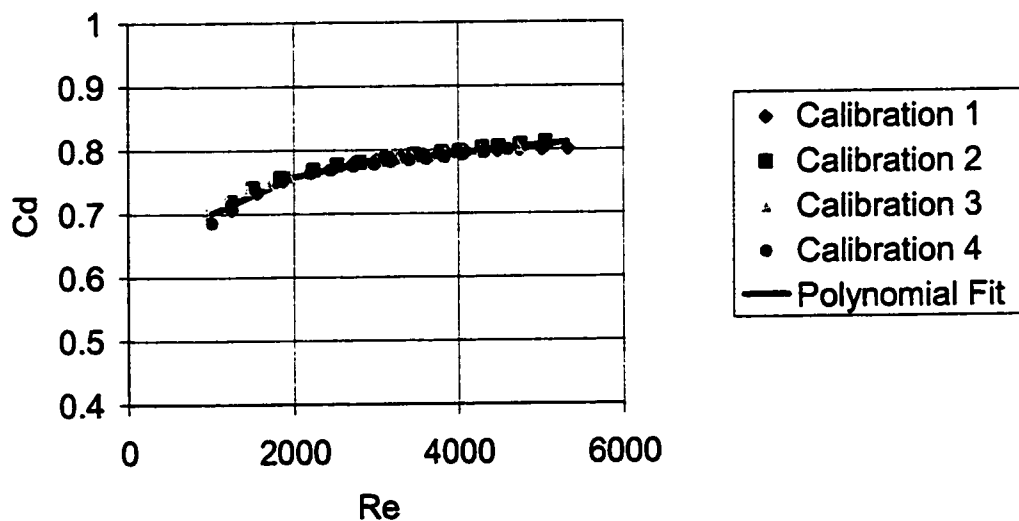


**Figure 5.4: Calibration for a 0.003m diameter orifice hole using water at room temperature.**

It is clear that there is little random scatter, yet there are differences that exist between each calibration, even though they are generated under identical conditions. This is the result of systematic differences that are attributed to errors in the analytical

expressions for flow rate. A 3<sup>rd</sup> order polynomial fit was used on all four data sets together making it possible to determine a standard deviation term for discharge coefficient that represents differences between the four calibrations.

$$C_d = 2.587 \times 10^{-12}(\text{Re})^3 - 3.110 \times 10^{-8}(\text{Re})^2 + 1.326 \times 10^{-4}(\text{Re}) + 5.965 \times 10^{-1} \quad (105)$$

The standard deviation in discharge coefficient was determined using Equation (105) and each experimental data point represented in Figure 5.4.

$$\delta C_d = \sqrt{\frac{\sum (C_{d, \text{poly}} - C_{d, \text{exp}})^2}{n - 4}} = 0.0035 \quad (106)$$

Where n, the number of data points, is equal to 295 for all four calibrations combined.

### 5.1.3 Surface Tension of Water at 321.5 K

The data presented in Figures 5.1, 5.3, and 5.4 for water at 321.5 K were used to test the validity of Equation (92). First, each of the four room temperature calibrations was used independently to analyze the propagation of errors theory. A 3<sup>rd</sup> order polynomial fit was used to describe each of the four calibrations. All four calibrations were also used in combination to produce a more statistically sound function. This function is Equation (105) and is also represented in Table 5.1 as the “combination” data set. The variability between the four relationships is attributed to random errors in head, and systematic errors in flow rate.

**Table 5.1: Polynomial constants that describe the discharge coefficient as a function of Reynolds number.**

Calibration	A	b	c	d
#1	$3.38 \times 10^{-12}$	$-3.80 \times 10^{-8}$	$1.52 \times 10^{-4}$	$5.83 \times 10^{-1}$
#2	$2.92 \times 10^{-12}$	$-3.71 \times 10^{-8}$	$1.61 \times 10^{-4}$	$5.60 \times 10^{-1}$
#3	$2.53 \times 10^{-12}$	$-2.84 \times 10^{-8}$	$1.18 \times 10^{-4}$	$6.18 \times 10^{-1}$
#4	$4.64 \times 10^{-12}$	$-4.84 \times 10^{-8}$	$1.76 \times 10^{-4}$	$5.61 \times 10^{-1}$
Combination	$2.587 \times 10^{-12}$	$-3.110 \times 10^{-8}$	$1.326 \times 10^{-4}$	$5.965 \times 10^{-1}$

Results for the surface tension of water at 321.5 K are presented in Figure 5.5 for each of the four independent calibrations. The average value indicated on the chart represents the average of all points represented in Figure 5.5.

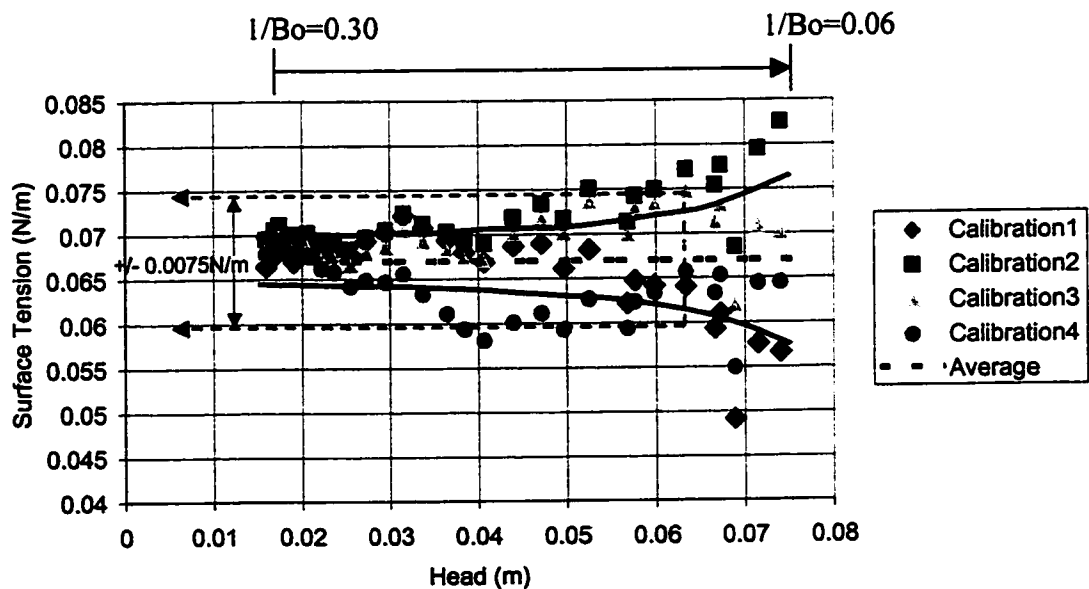


**Figure 5.5: Experimental surface tension as a function of head for water at 321.5 K for four separate calibrations.**

The propagation of errors analysis, explained in section 5.1.1, was used to predict the error in the determination of surface tension. The standard deviation in head and discharge coefficient was used to calculate the expected error, represented by the solid arrow lines in Figure 5.5. The solid lines were determined through application of Equation (95). The partial derivatives with respect to  $h$  and  $C_d$  are Equations (96) and (98) respectively. The standard deviations in  $h$  and  $C_d$  are determined as indicated from Equations (101) and (106) respectively. The deviation with respect to flow rate was not considered in the calculation. The propagation of error analysis reasonably predicts the magnitude of error in surface tension since scatter between the four calibrations follows similar trends to the predicted deviation lines. This confirms, as predicted in section 5.1.1, that errors in surface tension increase with head. Also, there appears to be greater deviations between the four calibrations than is exhibited within each calibration. This indicates that random errors related to head measurements, appear to be insignificant. Thus, errors inherent with the discharge coefficient seem to dominate the accuracy of the surface tension measurement. Applying Equation (99) facilitates the maximum head to be calculated resulting in a maximum amount of error in surface tension. As an example, if the tolerance in the calculation is  $\pm 0.0075$  N/m, then substituting appropriate variables in Equation (99) yields:

$$h < \frac{C_d \left( \frac{\partial \sigma}{\partial C_d} \right)}{2 \rho g r_o Fr} < \frac{(0.8) \left( \frac{0.0075 \text{ N/m}}{0.0035} \right)}{2 (988 \text{ kg/m}^3) (9.81 \text{ m/s}^2) (1.5 \times 10^{-3} \text{ m}) (0.93)} < 0.0636 \text{ m} \quad (99a)$$

Recall that the deviation in discharge coefficient was determined from Equation (106) to be 0.0035. The region indicated by the dashed arrows in Figure 5.5 predicts the range of head conditions deemed acceptable in terms of error in surface tension. The results

represented in Figure 5.5 confirm that for a tolerance of  $\pm 0.0075\text{N/m}$ , the head should be no greater than  $0.0636\text{m}$ . Figure 5.6 represents the maximum head that should be utilized for a variety of hypothetical errors in surface tension for this system.

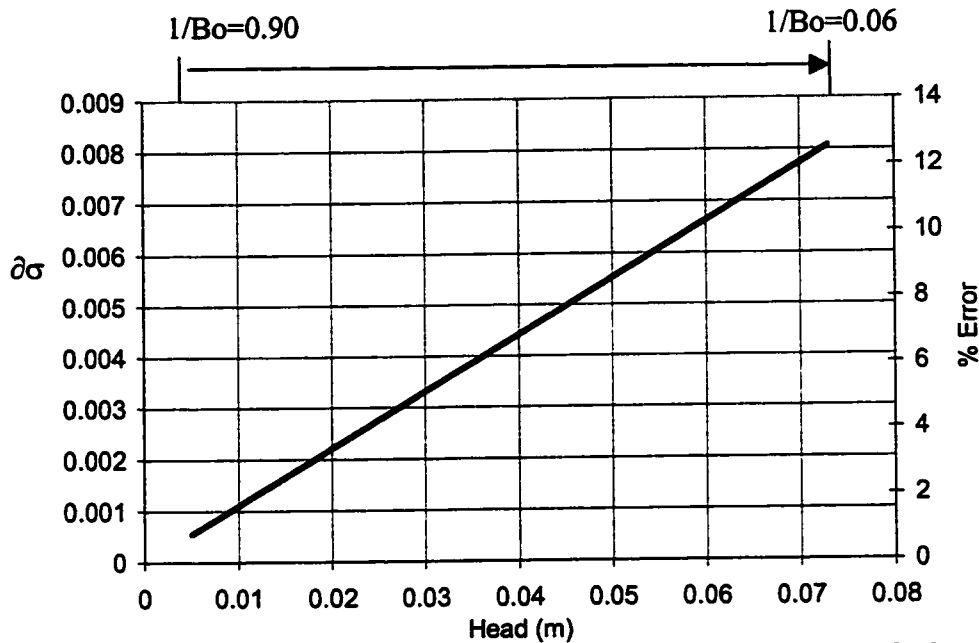


**Figure 5.6: Maximum head height determined for a specified error in surface tension for water draining through a  $0.003\text{m}$  diameter orifice at  $321.5\text{ K}$ .**

Next, the polynomial curve that was fitted to all four calibrations was used to calculate the surface tension (combination that is illustrated in Table 5.1). By doing this, a more statistically sound calibration is used since all four calibrations are considered together and the number of data points used in generating the curve is increased by a factor of four. Figure 5.7 illustrates the results using this relationship. The standard deviation of the data presented in Figure 5.7 is  $0.002\text{ N/m}$ . Results are presented and compared with literature in Table 5.2.

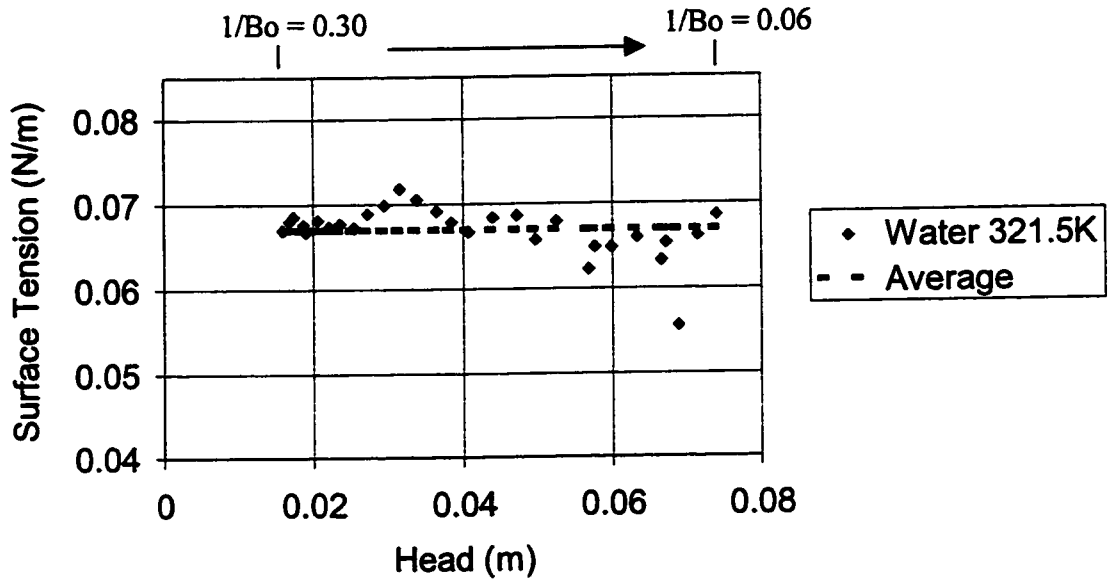


**Figure 5.7: Average surface tension of water at 321.5 K.**

**Table 5.2: Comparison between experimental surface tension and literature value for water at 321.5 K [61].**

Average Experimental Surface Tension (N/m)	CRC Handbook of Chemistry and Physics at 321.5 K (N/m)	Percentage Difference (%)
$0.0670 \pm 0.002$	0.0682	1.75

The validation of the model is confirmed since the average surface tension that is calculated using this approach is in agreement with the accepted literature value at 321.5 K to within the experimental error.

## **5.2 Formulation for Simultaneous Determination of Surface Tension, Viscosity, and Density**

Uncertainties associated with the values of density and viscosity will yield systematic errors that may seriously impact the calculation of surface tension.



Fortunately, the statistical nature of these experiments makes it possible to not only measure surface tension, but density and viscosity as well. The vast amount of data each experiment produces facilitates the simultaneous calculation of all three properties using non-linear regression analysis.

The following discussion outlines the formulation of the Gauss-Newton method. The experimental head,  $h_{i,\text{exp}}$ , can be expressed as a function of experimental flow rate,  $f(Q_{i,\text{exp}})$  with a certain degree of error,  $\delta h_{i,\text{exp}}$ , as follows:

$$h_{i,\text{exp}} = f(Q_{i,\text{exp}}) + \delta h_{i,\text{exp}} \quad (107)$$

Where  $h_{i,\text{exp}}$  and  $Q_{i,\text{exp}}$  are experimental data points that are expressed in vector notation:

$$h_{\text{exp}} = \begin{bmatrix} h_{1,\text{exp}} \\ \cdot \\ \cdot \\ h_{i,\text{exp}} \\ h_{n,\text{exp}} \end{bmatrix} \quad (108)$$

$$Q_{\text{exp}} = \begin{bmatrix} Q_{1,\text{exp}} \\ \cdot \\ \cdot \\ Q_{i,\text{exp}} \\ Q_{n,\text{exp}} \end{bmatrix} \quad (109)$$

Next, the function for surface tension in terms of  $Q_{\text{exp}}$ ,  $h_{\text{exp}}$  and constants  $a$ ,  $b$ ,  $c$ , and  $d$ , described by Equation (94), is to be rearranged in terms of one of the experimental variables. Using the format in Equation (107) the theoretical head is written in terms of  $Q_{\text{exp}}$  as follows:

$$f(Q_{i,\text{exp}}) = \frac{1}{2g} \left( \frac{Q_{i,\text{exp}}}{\left( a \left( \frac{2\rho_o Q_{i,\text{exp}}}{\pi_o^2 \eta} \right)^3 + b \left( \frac{2\rho_o Q_{i,\text{exp}}}{\pi_o^2 \eta} \right)^2 + c \left( \frac{2\rho_o Q_{i,\text{exp}}}{\pi_o^2 \eta} \right) + d \right) \pi_o^2} \right)^2 + \frac{\sigma}{\rho g r_o} \quad (110)$$

Flow rate,  $Q_{\text{exp}}$ , is a volumetric quantity that is determined from mass flow rate data. Consequently, information on density is required so that the mass can be converted to a volumetric quantity. Since density is considered an unknown in this analysis, the flux,  $V_{\text{exp}}$ , can be introduced to replace  $Q_{\text{exp}}$ :

$$V_{\text{exp}} = \frac{\rho Q_{\text{exp}}}{\pi_o^2} \quad (\text{kg/m}^2\text{s}) \quad (111)$$

Equation (110) can now be expressed as follows:

$$f(V_{i,\text{exp}}) = \frac{1}{2g} \left( \frac{V_{i,\text{exp}}}{\rho \left( a \left( \frac{2r_o V_{i,\text{exp}}}{\eta} \right)^3 + b \left( \frac{2r_o V_{i,\text{exp}}}{\eta} \right)^2 + c \left( \frac{2r_o V_{i,\text{exp}}}{\eta} \right) + d \right)} \right)^2 + \frac{\sigma}{\rho g r_o} \quad (112)$$

Equation (107) is now expressed in terms of flux:

$$h_{i,\text{exp}} = f(V_{i,\text{exp}}) + \delta h_{i,\text{exp}} \quad (113)$$

The non-linear model represented in Equation (112) is expanded in a Taylor series around the unknown properties,  $\sigma$ ,  $\eta$ , and  $\rho$ .

$$f(V_{i,\text{exp}})_{j+1} = f(V_{i,\text{exp}})_j + \frac{\partial f(V_{i,\text{exp}})}{\partial \sigma} \Delta \sigma + \frac{\partial f(V_{i,\text{exp}})}{\partial \eta} \Delta \eta + \frac{\partial f(V_{i,\text{exp}})}{\partial \rho} \Delta \rho \quad (114)$$

The subscript  $j$  corresponds to an initial guess, and,  $j+1$  is the result after a single iteration of the algorithm. Substituting Equation (114) into Equation (113) yields:

$$(h_{i,\text{exp}})_{j+1} - f(V_{i,\text{exp}})_j = \frac{\partial f(V_{i,\text{exp}})}{\partial \sigma} \Delta \sigma + \frac{\partial f(V_{i,\text{exp}})}{\partial \eta} \Delta \eta + \frac{\partial f(V_{i,\text{exp}})}{\partial \rho} \Delta \rho + (\delta h_{i,\text{exp}})_{j+1} \quad (115)$$

Equation (115) illustrates how differences between experimental and calculated values for head are minimized. Equation (115) can be represented in matrix notation:

$$\{Y\} = [Z_j] \{\Delta x\} + \{\Delta E\} \quad (116)$$

Where  $[Z_j]$  is a matrix of partial derivatives:

$$[Z]_j = \begin{Bmatrix} \frac{\partial f(V_{1,\text{exp}})}{\partial \sigma} & \frac{\partial f(V_{1,\text{exp}})}{\partial \eta} & \frac{\partial f(V_{1,\text{exp}})}{\partial \rho} \\ \cdot & \cdot & \cdot \\ \frac{\partial f(\dot{V}_{i,\text{exp}})}{\partial \sigma} & \frac{\partial f(\dot{V}_{i,\text{exp}})}{\partial \eta} & \frac{\partial f(\dot{V}_{i,\text{exp}})}{\partial \rho} \\ \frac{\partial f(V_{n,\text{exp}})}{\partial \sigma} & \frac{\partial f(V_{n,\text{exp}})}{\partial \eta} & \frac{\partial f(V_{n,\text{exp}})}{\partial \rho} \end{Bmatrix} \quad (117)$$

The partial derivatives of Equation (112), for substitution into Equation (115), with respect to  $\sigma$ ,  $\eta$ ,  $\rho$  are:

$$\frac{\partial f(V_{i,\text{exp}})}{\partial \sigma} = \frac{1}{\rho g r_o} \quad (118)$$

$$\frac{\partial f(V_{i,\text{exp}})}{\partial \eta} = \frac{V_{i,\text{exp}}^2}{g \rho^2} \left( \frac{1}{\left( a \left( \frac{2r_o V_{i,\text{exp}}}{\eta} \right)^3 + b \left( \frac{2r_o V_{i,\text{exp}}}{\eta} \right)^2 + c \left( \frac{2r_o V_{i,\text{exp}}}{\eta} \right) + d \right)} \right)^3$$

$$\left( \frac{24a(r_o V_{i,\text{exp}})^3}{\eta^4} + \frac{8b(r_o V_{i,\text{exp}})^2}{\eta^3} + \frac{2cr_o V_{i,\text{exp}}}{\eta^2} \right) \quad (119)$$

$$\frac{\partial f(V_{i,\text{exp}})}{\partial \rho} = -\frac{1}{g\rho^3} \left( \frac{V_{i,\text{exp}}}{\left( a\left(\frac{2r_o V_{i,\text{exp}}}{\eta}\right)^3 + b\left(\frac{2r_o V_{i,\text{exp}}}{\eta}\right)^2 + c\left(\frac{2r_o V_{i,\text{exp}}}{\eta}\right) + d \right)} \right)^2 - \frac{\sigma}{\rho^2 g r_o} \quad (120)$$

The vector  $\{Y\}$  corresponds to the difference between experimental and calculated head values:

$$\{Y\} = \begin{bmatrix} h_{1,\text{exp}} - f(V_{1,\text{exp}}) \\ \vdots \\ h_{i,\text{exp}} - f(V_{i,\text{exp}}) \\ h_{n,\text{exp}} - f(V_{n,\text{exp}}) \end{bmatrix} \quad (121)$$

Vector  $\{\Delta x\}$  corresponds to the change in properties:

$$\{\Delta x\} = \begin{bmatrix} \Delta \sigma \\ \Delta \eta \\ \Delta \rho \end{bmatrix} \quad (122)$$

The vector,  $\{\Delta E\}$  is the error associated with the differences between experimental and calculated head values. This quantity decreases as the solution converges. Applying linear least square theory results in the following matrix inverse relationship:

$$\{\Delta x\} = \left( [z]^T [z] \right)^{-1} [z]^T \{Y\} \quad (123)$$

An initial guess is made, and new quantities for  $\sigma$ ,  $\eta$ , and  $\rho$  are determined iteratively using Equations (124a) through (124c).

$$\sigma_{j+1} = \sigma_j + \Delta \sigma; \quad (124a)$$

$$\eta_{j+1} = \eta_j + \Delta \eta \quad (124b)$$

$$\rho_{j+1} = \rho_j + \Delta \rho; \quad (124c)$$

A series of convergence criteria must be met when the solution is stated. Convergence is met once the following quantities are smaller than a chosen tolerance,  $\varepsilon$ . For this study, the tolerance was chosen to be  $1 \times 10^{-6}$ .

$$\varepsilon_{\sigma} \geq \frac{\sigma_{j+1} - \sigma_j}{\sigma_{j+1}} \quad (125a)$$

$$\varepsilon_{\eta} \geq \frac{\eta_{j+1} - \eta_j}{\eta_{j+1}} \quad (125b)$$

$$\varepsilon_{\rho} \geq \frac{\rho_{j+1} - \rho_j}{\rho_{j+1}} \quad (125c)$$

The values  $\varepsilon_{\sigma}$ ,  $\varepsilon_{\eta}$ ,  $\varepsilon_{\rho}$ , correspond to the tolerance of each property. If one of the criteria represented in Equations (125a) through (125c) is not met, the algorithm is performed for an additional iteration using the updated values for  $\sigma$ ,  $\eta$ , and  $\rho$  as the new initial guess. The Matlab program used to perform this computational technique is presented in Appendix B.

### 5.2.1 Error Analysis

The propagation of errors theorem can be used not only to determine the sensitivity of the surface tension calculation, but the sensitivity of the viscosity and density calculation as well.

### 5.2.1.1 Surface Tension

Using non-linear regression, the prediction in uncertainty of surface tension is identical to the approach outlined in section 5.1.1. The issues associated with errors in head, flow rate and discharge coefficient are addressed in Equations (96) through (98).

### 5.2.1.2 Density

The propagation of errors theorem when applied to the calculation of density requires Equation (92) to be rearranged in terms of density:

$$\rho = \frac{\sigma}{gr_o \left( h - \frac{1}{2g} \left( \frac{Q_{\text{exp}}}{C_d \pi r_o^2} \right)^2 \right)} \quad (126)$$

Applying propagation of errors theorem to Equation (126):

$$\delta\rho = \sqrt{\left( \frac{\partial\rho}{\partial h} \right)^2 (\delta h)^2 + \left( \frac{\partial\rho}{\partial Q_{\text{exp}}} \right)^2 (\delta Q_{\text{exp}})^2 + \left( \frac{\partial\rho}{\partial C_d} \right)^2 (\delta C_d)^2} \quad (127)$$

Similar to the error analysis with surface tension, the quantities  $\delta h$ ,  $\delta Q_{\text{exp}}$ , and  $\delta C_d$  refer to the standard deviations in head, flow rate and discharge coefficient. Before proceeding, the following terms will be recalled from Chapter 4:

$$Fr = \frac{1}{2gh} u_{\text{theo}}^2 = \frac{1}{2gh} \left( \frac{Q_{\text{exp}}}{C_d \pi r_o^2} \right)^2 \quad (128)$$

$$1 - Fr = 1/B_o \quad (129)$$

$$1/Bo = \frac{\sigma}{\rho g r_o h} \quad (130)$$

The derivative of Equation (126) with respect to h is:

$$\frac{\partial \rho}{\partial h} = \frac{-\sigma}{gr_o \left( h - \frac{1}{2g} \left( \frac{Q_{exp}}{C_d \pi r_o^2} \right)^2 \right)^2} = \frac{-\sigma}{gr_o h^2 \left( 1 - \frac{1}{2gh} \left( \frac{Q_{exp}}{C_d \pi r_o^2} \right)^2 \right)^2} \quad (131)$$

Substituting equations (128) through (130) into Equation (131) yields:

$$\frac{\partial \rho}{\partial h} = -\frac{\rho^2 g r_o}{\sigma} \quad (132)$$

The derivative of Equation (126) with respect to  $Q_{exp}$  is:

$$\frac{\partial \rho}{\partial Q_{exp}} = \frac{\sigma Q_{exp}}{g^2 C_d^2 \pi^2 r_o^5} \frac{1}{\left[ h - \frac{1}{2g} \left( \frac{Q_{exp}}{C_d \pi r_o^2} \right)^2 \right]^2} = \frac{\sigma Q_{exp}}{g^2 C_d^2 \pi^2 r_o^5 h^2} \frac{1}{\left[ 1 - \frac{1}{2gh} \left( \frac{Q_{exp}}{C_d \pi r_o^2} \right)^2 \right]^2} \quad (133)$$

Substituting Equations (128) through (129) into (133) yields:

$$\frac{\partial \rho}{\partial Q_{exp}} = \frac{\rho^2 Q_{exp}}{C_d^2 \pi^2 r_o^3 \sigma} = \frac{\rho^2 u_{theo}}{C_d \pi r_o \sigma} = \frac{\rho^2 \sqrt{2gh(Fr)}}{C_d \pi r_o \sigma} = \frac{\rho^2 \sqrt{2gh(1 - 1/Bo)}}{C_d \pi r_o \sigma} \quad (134)$$

The derivative of Equation (126) with respect to  $C_d$  is:

$$\begin{aligned} \frac{\partial \rho}{\partial C_d} &= -\frac{\sigma}{C_d g^2 r_o} \left( \frac{Q_{exp}}{C_d \pi r_o^2} \right)^2 \frac{1}{\left[ h - \frac{1}{2g} \left( \frac{Q_{exp}}{C_d \pi r_o^2} \right)^2 \right]^2} \\ &= -\frac{\sigma}{C_d g^2 r_o h^2} \left( \frac{Q_{exp}}{C_d \pi r_o^2} \right)^2 \frac{1}{\left[ 1 - \frac{1}{2gh} \left( \frac{Q_{exp}}{C_d \pi r_o^2} \right)^2 \right]^2} \end{aligned} \quad (135)$$

Substituting (128) through (129) into Equation (135) yields:

$$\begin{aligned}\frac{\partial \rho}{\partial C_d} &= -\frac{\rho^2 Q_{exp}^2}{\sigma \pi^2 r_o^3 C_d^3} = -\frac{\rho^2 r_o u_{theo}^2}{\sigma C_d} = -\frac{\rho^2 2 g r_o h F r}{\sigma C_d} = -\frac{\rho^2 2 g r_o h (1 - 1/Bo)}{\sigma C_d} \\ &= -\frac{2 \rho (1 - 1/Bo)}{C_d (1/Bo)}\end{aligned}\quad (136)$$

### *Errors in Head*

Like surface tension measurements, errors associated with head produce error in density measurements that are independent of the dynamic conditions (head, flow rate and discharge coefficient). Low-density fluids with a high surface tension produce less uncertainty in terms of density calculations as Equation (132) indicates. A small orifice radius is also favorable to larger sizes as are relatively high discharge coefficients.

### *Errors in Flow Rate*

Like surface tension measurements, errors in flow rate produce higher deviations in density measurements when low-density liquids are used that have relatively high surface tensions. This is further reinforced with the presence of the Bond number in Equation (134). Discharge coefficients that approach unity result in favorable conditions as well since discharge coefficient appears in the denominator. Like surface tension, it is best to have larger orifice sizes in the presence of errors in flow rate for more accurate density measurements.

### *Errors in Discharge Coefficient*

In terms of errors in discharge coefficient, Equation (136) indicates that accurate density measurements are facilitated when low-density liquids with relatively high surface tensions are used. The presence of the Bond number indicates that high surface tension is favorable as well as conditions of low head. Again, discharge coefficients that



approach unity are favorable because the discharge coefficient is in the denominator of Equation (136).

### 5.2.1.3 Viscosity

In analyzing the sensitivity of the viscosity calculation, the task is not as trivial as it is when studying surface tension and density. A problem arises when rearranging the function in terms of viscosity because it cannot be solved for directly, as Equation (94) indicates. An assumption is made that  $C_d$  vs.  $Re$  curve is piece wise linear so that the constants  $a$ , and  $b$ , are zero. This assumption is only valid for  $4000 < Re < 13000$ , as will be revealed in Section 5.2.1.

The propagation of errors theorem is applied to Equation (94), which is rearranged in terms of viscosity in this instance. The associated errors are assumed to be head, flow rate, as well as uncertainty in constants  $c$ , and  $d$  that approximate the frictional characteristics of the orifice. Rearranging Equation (94):

$$\eta = \frac{2c\rho_o Q_{exp}}{\left( \frac{Q_{exp}}{\sqrt{2g\left(h - \frac{\sigma}{\rho g r_o}\right)}} - \pi r_o^2 d \right)} \quad (137)$$

Applying propagation of errors theorem:

$$\delta\eta = \sqrt{\left(\frac{\partial\eta}{\partial h}\right)^2 (\delta h)^2 + \left(\frac{\partial\eta}{\partial Q_{exp}}\right)^2 (\delta Q_{exp})^2 + \left(\frac{\partial\eta}{\partial c}\right)^2 (\delta c)^2 + \left(\frac{\partial\eta}{\partial d}\right)^2 (\delta d)^2} \quad (138)$$

The derivative of Equation (137) with respect to  $h$  are derived as follows:

$$\begin{aligned}
\frac{\partial \eta}{\partial h} &= \frac{2c\rho r_o g Q_{\text{exp}}^2}{\left[ \frac{Q_{\text{exp}}}{\sqrt{2g\left(h - \frac{\sigma}{\rho g r_o}\right)}} - \pi r_o^2 d \right]^2 \left[ 2g\left(h - \frac{\sigma}{\rho g r_o}\right) \right]^{\frac{3}{2}}} \\
&= \frac{2c\rho r_o g Q_{\text{exp}}^2}{\left[ \frac{\pi r_o^2}{\pi r_o^2} \frac{Q_{\text{exp}}}{\sqrt{2g\left(h - \frac{\sigma}{\rho g r_o}\right)}} - \pi r_o^2 d \right]^2 2gh\left(1 - \frac{\sigma}{\rho g r_o h}\right) \sqrt{2gh\left(1 - \frac{\sigma}{\rho g r_o h}\right)}}
\end{aligned} \tag{139}$$

Recall from Equations (85) and (90) that:

$$\frac{Q_{\text{exp}}}{\pi r_o^2 \sqrt{2g\left(h - \frac{\sigma}{\rho g r_o}\right)}} = \frac{Q_{\text{exp}}}{Q_{\text{theo}}} = C_d \tag{140}$$

Substitute (140) into (139):

$$\frac{\partial \eta}{\partial h} = \frac{C_d^2}{C_d^2} \frac{2c\rho r_o g Q_{\text{exp}}^2}{\pi^2 r_o^4 [C_d - d]^2 2gh\left(1 - \frac{\sigma}{\rho g r_o h}\right) \sqrt{2gh\left(1 - \frac{\sigma}{\rho g r_o h}\right)}} \tag{141}$$

Recall from Equation (75) that:

$$\left( \frac{Q_{\text{exp}}}{C_d \pi r_o^2} \right)^2 \frac{1}{2gh} = Fr \tag{142}$$

And from Equations (88) and (89) that:

$$\left( 1 - \frac{\sigma}{\rho g r_o h} \right) = \left( 1 - \frac{1}{Bo} \right) = Fr \tag{143}$$

Substituting Equation (142) and (143) into Equation (141):

$$\frac{\partial \eta}{\partial h} = \frac{2c\rho r_o C_d^2 g Fr}{(C_d - d)^2 Fr \sqrt{2gh(Fr)}} = \frac{2c\rho r_o C_d^2 g}{(C_d - d)^2 \sqrt{2gh(1 - 1/B_o)}} \quad (144)$$

In order take derivatives of Equation (137) with respect to  $Q_{\text{exp}}$ , rewrite Equation (137) as follows:

$$\eta = \frac{2c\rho r_o}{\left[ \frac{1}{\sqrt{2g\left(h - \frac{\sigma}{\rho g r_o}\right)}} - \frac{\pi r_o^2 d}{Q_{\text{exp}}} \right]} \quad (145)$$

The derivative of Equation (145) with respect to  $Q_{\text{exp}}$ :

$$\frac{\partial \eta}{\partial Q_{\text{exp}}} = - \frac{2c\rho r_o (\pi r_o^2 d)}{Q_{\text{exp}}^2 \left[ \frac{1}{\sqrt{2g\left(h - \frac{\sigma}{\rho g r_o}\right)}} - \frac{\pi r_o^2 d}{Q_{\text{exp}}} \right]^2} = - \frac{2c\rho r_o (\pi r_o^2 d)}{\left[ \frac{\pi r_o^2}{\pi r_o^2} \frac{Q_{\text{exp}}}{\sqrt{2g\left(h - \frac{\sigma}{\rho g r_o}\right)}} - \pi r_o^2 d \right]^2} \quad (146)$$

Substitute Equation (140) into (146):

$$\frac{\partial \eta}{\partial Q_{\text{exp}}} = - \frac{2c r_o (\pi r_o^2 d)}{\pi^2 r_o^4 [C_d - d]^2} = - \frac{2c \rho d}{\pi r_o (C_d - d)^2} \quad (147)$$

The discharge coefficient,  $C_d$ , may be written in terms of  $Q_{\text{exp}}$ .

$$C_d = c \left( \frac{\rho 2 Q_{\text{exp}}}{\pi r_o \eta} \right) + d \quad (148)$$

Substituting Equation (148) into (147) and applying Equation (142):

$$\begin{aligned}\frac{\partial \eta}{\partial Q_{\text{exp}}} &= -\frac{2c\rho d}{\pi_o \left( c \frac{\rho 2Q_{\text{exp}}}{\pi_o \eta} \right)^2} = -\frac{d\pi_o \eta^2}{2c\rho Q_{\text{exp}}^2} \frac{\pi_o^3 C_d^2}{\pi_o^3 C_d^2} = -\frac{d\eta^2}{4c\rho gh \pi_o^3 C_d^2 Fr} \\ &= -\frac{d\eta^2}{4c\rho gh \pi_o^3 C_d^2 (1 - 1/Bo)}\end{aligned}\quad (149)$$

The derivative of Equation (137) with respect to  $c$  is derived as follows:

$$\frac{\partial \eta}{\partial c} = \frac{2\rho_o Q_{\text{exp}}}{\left[ \frac{Q_{\text{exp}}}{\sqrt{2g\left(h - \frac{\sigma}{\rho g r_o}\right)}} - \pi_o^2 d \right]} = \frac{2\rho_o Q_{\text{exp}}}{\left[ \frac{\pi_o^2}{\pi_o^2} \frac{Q_{\text{exp}}}{\sqrt{2g\left(h - \frac{\sigma}{\rho g r_o}\right)}} - \pi_o^2 d \right]}\quad (150)$$

Substituting Equation (140) into (150) yields:

$$\frac{\partial \eta}{\partial c} = \frac{2\rho_o Q_{\text{exp}}}{\pi_o^2 [C_d - d]}\quad (151)$$

The discharge coefficient,  $C_d$ , may be written in terms of constants  $c$  and  $d$ . Substitute Equation (148) into (151):

$$\frac{\partial \eta}{\partial c} = \frac{2\rho_o Q_{\text{exp}}}{\pi_o^2 c \left( \frac{\rho 2Q_{\text{exp}}}{\pi_o \eta} \right)} = \frac{\eta}{c}\quad (152)$$

The derivative of Equation (137) with respect to  $d$  is derived as follows:

$$\frac{\partial \eta}{\partial d} = \frac{2c\rho_o Q_{\text{exp}} (\pi_o^2)}{\left[ \frac{Q_{\text{exp}}}{\sqrt{2g\left(h - \frac{\sigma}{\rho g r_o}\right)}} - \pi_o^2 d \right]^2} = \frac{2c\rho_o Q_{\text{exp}} (\pi_o^2)}{\left[ \frac{\pi_o^2}{\pi_o^2} \frac{Q_{\text{exp}}}{\sqrt{2g\left(h - \frac{\sigma}{\rho g r_o}\right)}} - \pi_o^2 d \right]^2}\quad (153)$$

Substituting Equation (140) into (153):

$$\frac{\partial \eta}{\partial d} = \frac{2c\rho r_o Q_{\text{exp}} (\pi r_o^2)}{\pi^2 r_o^4 [C_d - d]^2} = \frac{2c\rho r_o Q_{\text{exp}}}{\pi r_o^2 [C_d - d]^2} \quad (154)$$

The discharge coefficient,  $C_d$  may be written in terms of  $c$  and  $d$ . Substituting Equation (148) into (154), and applying Equation (142):

$$\frac{\partial \eta}{\partial d} = \frac{2c\rho r_o Q_{\text{exp}}}{\pi r_o^2 \left[ c \frac{\rho 2 Q_{\text{exp}}}{\pi r_o \eta} \right]^2} = \frac{\pi r_o \eta^2}{2c\rho Q_{\text{exp}}} \quad (155)$$

### *Errors in Head*

Referring to Equation (144), the significance of constants  $c$  and  $d$  can be determined. These constants are an indication as to what shape the discharge coefficient curve exhibits favorable conditions in measuring viscosity. It is clear that when the slope (constant  $c$ ), is shallow, that errors are expected to be minimal. Also, due to the presence of the y-intercept (constant  $d$ ), it can be stated that the discharge coefficient should be relatively low in the presence of errors in head. In short, the frictional characteristics of the orifice should be significant yet exhibit a small dependency on the processing variables (represented by the Reynolds number). Equation (144) indicates as well that increasing head will result in lower errors when calculating viscosity.

### *Errors in Flow Rate*

Unlike the case with the surface tension and density measurements, Equation (149) indicates that errors in flow rate are not as significant in terms of the viscosity calculation if high-density liquids are used. It is also favorable to operate under high head conditions. These concepts are reinforced due to the presence of the Bond number, which indicates in this instance that high potential forces are favorable relative to surface

forces. Large orifice radii are also favorable. The shape of the discharge coefficient curve should have a steep slope (opposite to errors in head) with a small y-intercept. A steep slope indicates that the discharge coefficient exhibits a strong dependence on Reynolds number.

#### *Errors in Constant "c"*

Errors inherent with the slope of the discharge coefficient curve produce deviations in terms of viscosity less significant when the slope is relatively steep (large  $c$ ), as Equation (152) indicates. The discharge coefficient should therefore exhibit a strong dependence on Reynolds number.

#### *Errors in Constant "d"*

Equation (155) indicates that high-density fluids are favorable with small orifice diameters if there are errors associated with the y-intercept of the discharge coefficient curve. High flow rate conditions are favorable as well. A steep slope (large  $c$ ) is favorable as well, indicating that the discharge coefficient should be a strong function of Reynolds number.

### **5.2.1.4 Summary of Propagation of Errors**

The error analysis has provided a useful analysis of the set of conditions necessary in measuring the surface tension, viscosity and density for varying degrees of precision. Consider the presence of both errors in head and flow rate. It has been observed that when calculating surface tension and density conditions are favorable when  $h$  and  $Q_{\text{exp}}$  are relatively small (indicating small potential and inertial energies).

However, in measuring viscosity, the opposite holds true for accuracy in the calculation (high  $h$  and  $Q_{\text{exp}}$  increases accuracy). This is qualitatively illustrated in Figure 5.8 where it is suggested that a balance of conditions should be established to provide a reasonable degree of accuracy for surface tension, density and viscosity. The dashed arrows intersecting the x-axis suggest a range of values for  $h$  or  $Q_{\text{exp}}$  corresponding to a relative error that can be specified on the y-axis.

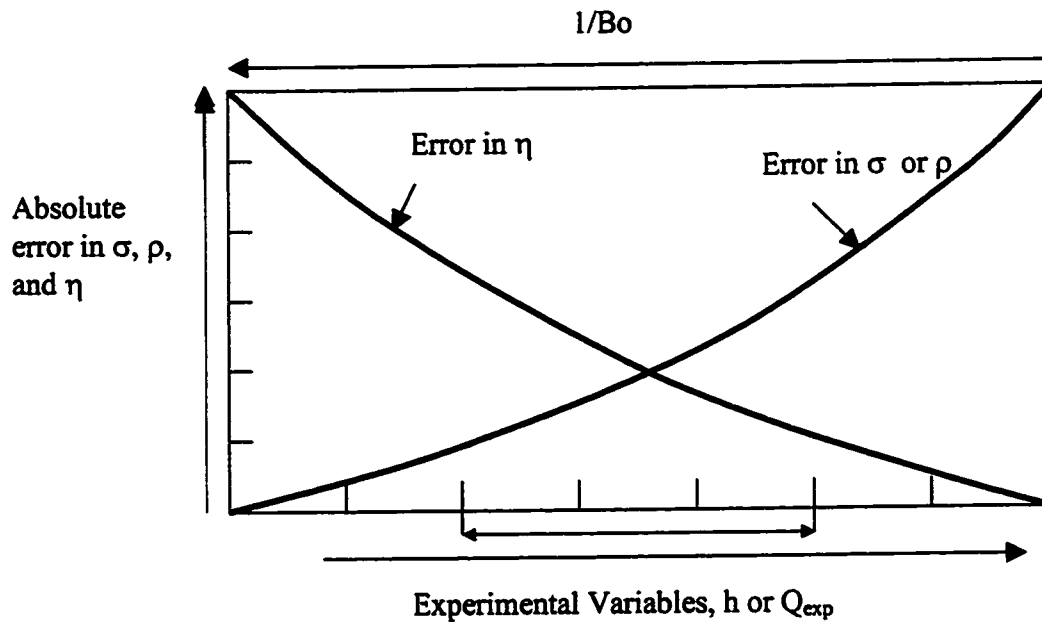


**Figure 5.8: Errors in property measurements as a function of  $h$  and  $Q_{\text{exp}}$ , due to errors in  $Q_{\text{exp}}$  and  $C_d$ .**

The effect of increasing discharge coefficient can be qualitatively illustrated on a chart similar to Figure 5.8. Consider errors in flow rate and discharge coefficient. Figure 5.9 illustrates that a large discharge coefficient (indicative of an orifice design exhibiting low frictional characteristics) is favorable in measuring both surface tension and density.

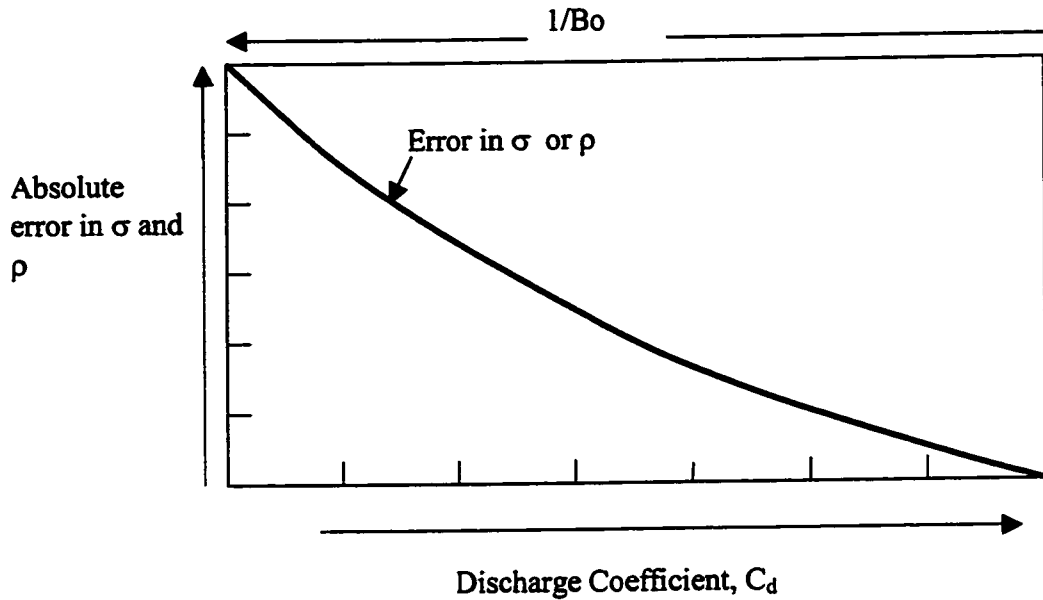


**Figure 5.9: Errors in property measurements as a function of  $C_d$ , due to errors in  $Q_{exp}$  and  $C_d$ .**

Consider the viscosity measurement. In the presence of errors in head, it is desirable to have a low discharge coefficient with a small dependence on Reynolds number (low  $c$  and low  $d$ ). In the presence of errors in flow rate and constants  $c$  and  $d$ , it is desirable for the discharge coefficient to have a strong dependence on Reynolds number. This means that the slope,  $c$ , should be large to improve accuracy.

The orifice radius is considered in Figure 5.10 where errors in head and flow rate are accounted for. Errors in head result in deviations for all three properties in the same direction. Increasing the orifice radius increases the error in surface tension, viscosity and density calculations. Conversely, in the presence of errors in flow rate, increasing the orifice radius results in lower deviations in surface tension, viscosity and density. If the errors inherent with measurements are properly characterized, the appropriate orifice



radius can be determined to improve on the accuracy of all three properties. In the presence of errors in the discharge coefficient, increasing the orifice radius results in increases in error for surface tension and density calculations. Finally, errors in the intercept result in decreasing error in the viscosity calculation as radius is decreased.

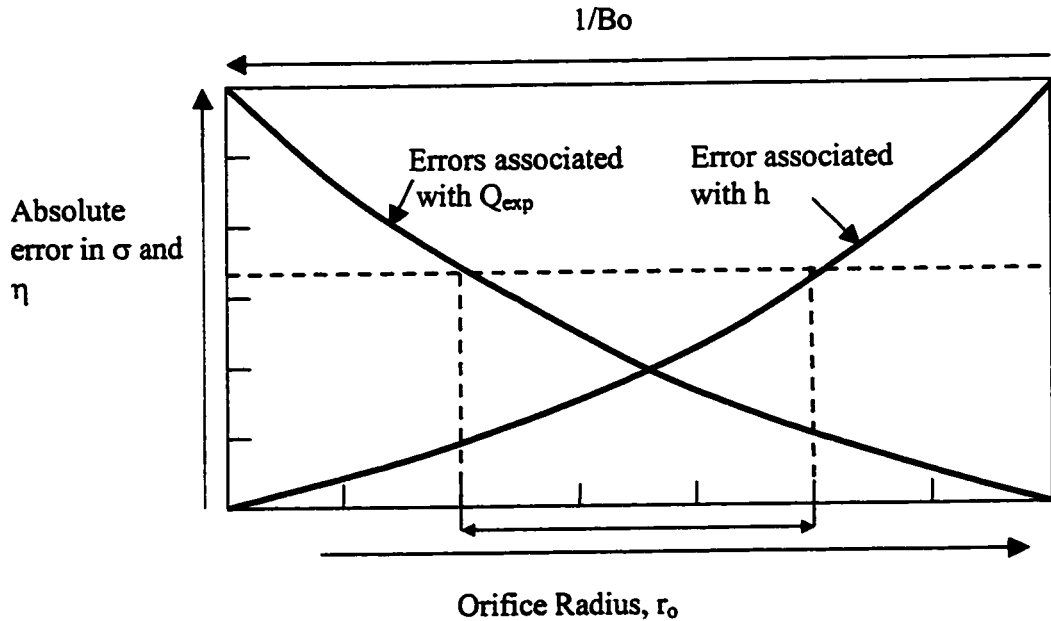


**Figure 5.10: Errors in property measurements as a function of  $r_o$ , due to errors in  $h$  and  $Q_{exp}$ .**

### 5.2.2 Data Analysis

Aluminum was melted using the induction furnace described in Section 3.2.3. The surface tension, viscosity, and density were measured using the formulation presented in this section. The mass of aluminum used was 1.275 kg and it was heated to a temperature of 1073 K, corresponding to 413 K superheat. The 0.005m diameter graphite orifice plate was used. The mass was cumulatively measured as a function of time using the loadcell and data acquisition system. The strain recorded by the loadcell

was converted to mass knowing the weight of aluminum that poured through the orifice and the strain before and after experimentation. Similar to the low temperature tests, flow rate is determined by differentiating the 2<sup>nd</sup> order polynomial function describing the cumulative mass with time. Head was determined in a different manner than it was for low temperature work. Using the cumulative mass data, the volume remaining in the crucible is determined at any time during the test. The crucible was calibrated such that the head can be determined for any volume. The discharge coefficient versus Reynolds number curve was (similarly to the low temperature work) generated using water at various temperatures. The crucible dimensions are given in section 3.2.2. The orifice plate that was used is illustrated in Section 3.2.1.

### *Measuring Head*

The calibration curve used to relate volume left in the crucible with head height is illustrated in Figure 5.11. The density is, therefore, required to determine the volume left in the crucible as the mass is cumulatively measured. Because density is considered an unknown in this analysis, an obvious paradox exists. Density values quoted from Iida and Guthrie [2] were used to calculate the volume and hence the head left in the crucible. This paradox will be addressed in the Section 5.2.3. Figure 5.12 represents the head measurements that were determined from the aluminum experiment. A second order polynomial fit was generated from the data and used to determine the amount of random error by calculating the standard deviation between the data and polynomial curve, which takes the following form:

$$h_{poly} = 6.25 \times 10^{-5} (t)^2 - 5.13 \times 10^{-3} (t) + 1.28 \times 10^{-1} \quad (\text{m}) \quad (156)$$

The standard deviation of Equation (156) with respect to the experimental data points that are represented in Figure 5.12 is determined using the following relationship with  $n=95$ :

$$\delta h = \sqrt{\frac{\sum (h_{poly} - h_{exp})^2}{n-3}} = 5.19 \times 10^{-4} \quad (\text{m}) \quad (157)$$

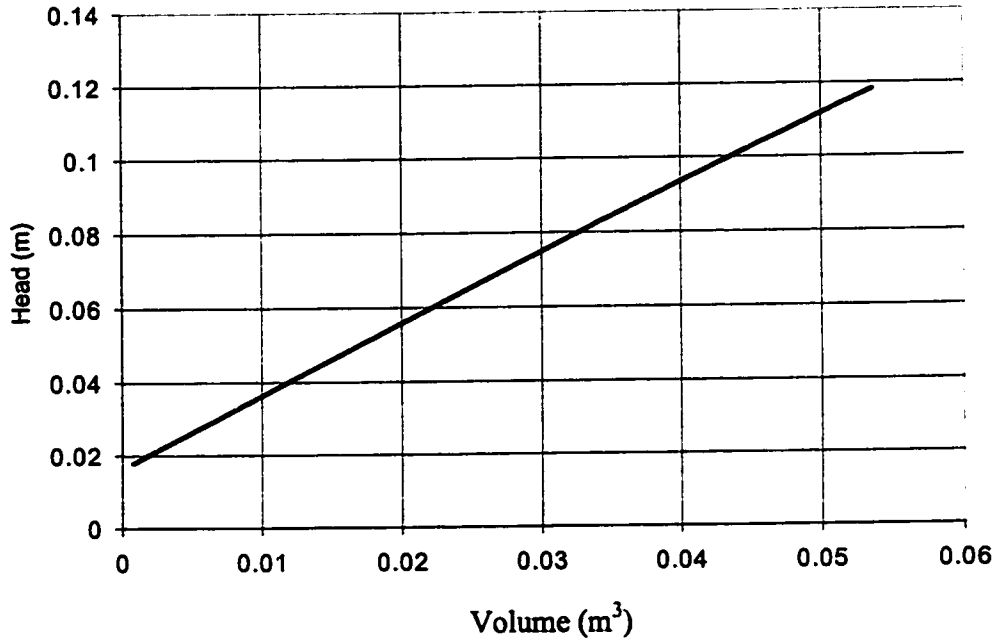


**Figure 5.11: Volume within the crucible corresponding to a particular head height.**

Similar to the low temperature work, the error associated with head measurement is considered to be random. For this case, however, the error is due to scatter registered by the loadcell instead of uncertainties in reading the graduations from a scale. The scatter is primarily due to the turbulent impact of the stream onto the loadcell system.

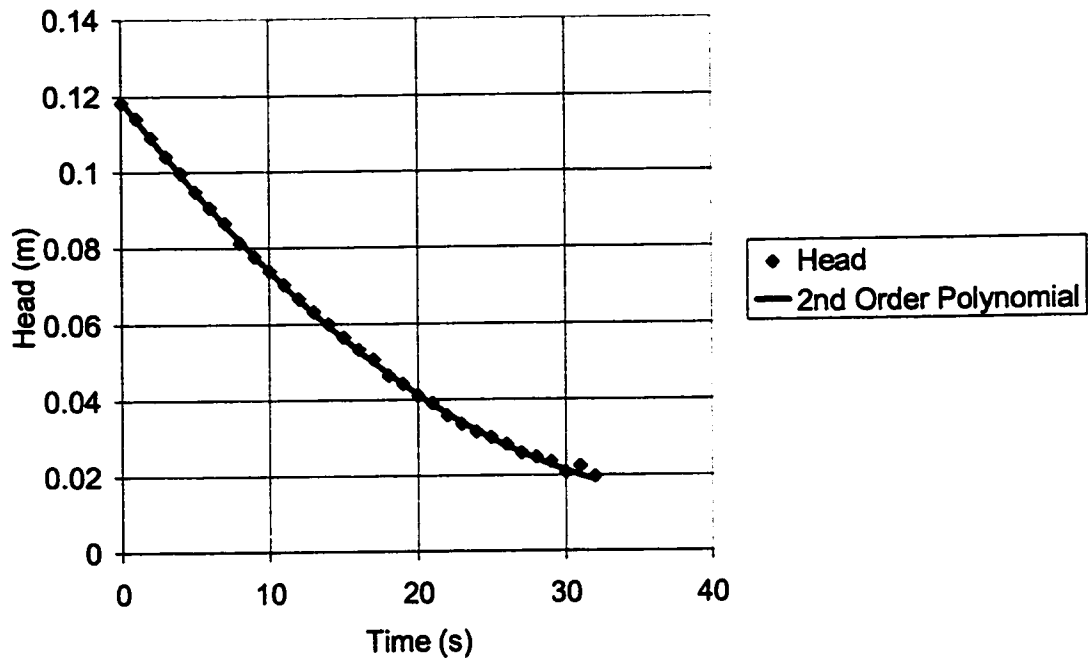


**Figure 5.12: Experimental head measurements for aluminum at 1073 K.  
Aluminum Test #32.**

### *Measuring Flow Rate*

Similar to the low temperature work, the error associated with flow rate is systematic since it is a product of differentiating the analytical expression describing the cumulative mass with time. The mass that was collected is represented in Figure 5.13.

The 2<sup>nd</sup> order polynomial fit of the cumulative mass is represented by Equation (158):

$$C_{m,poly} = -8.356 \times 10^{-4}(t)^2 + 6.491 \times 10^{-2}(t) + 2.212 \times 10^{-2} \quad (\text{kg}) \quad (158)$$

The flow rate is determined by taking the time derivative of Equation (158):

$$\frac{dC_{m,poly}}{dt} = -3.342 \times 10^{-3}(t) + 6.491 \times 10^{-2} \quad (\text{kg/s}) \quad (159)$$

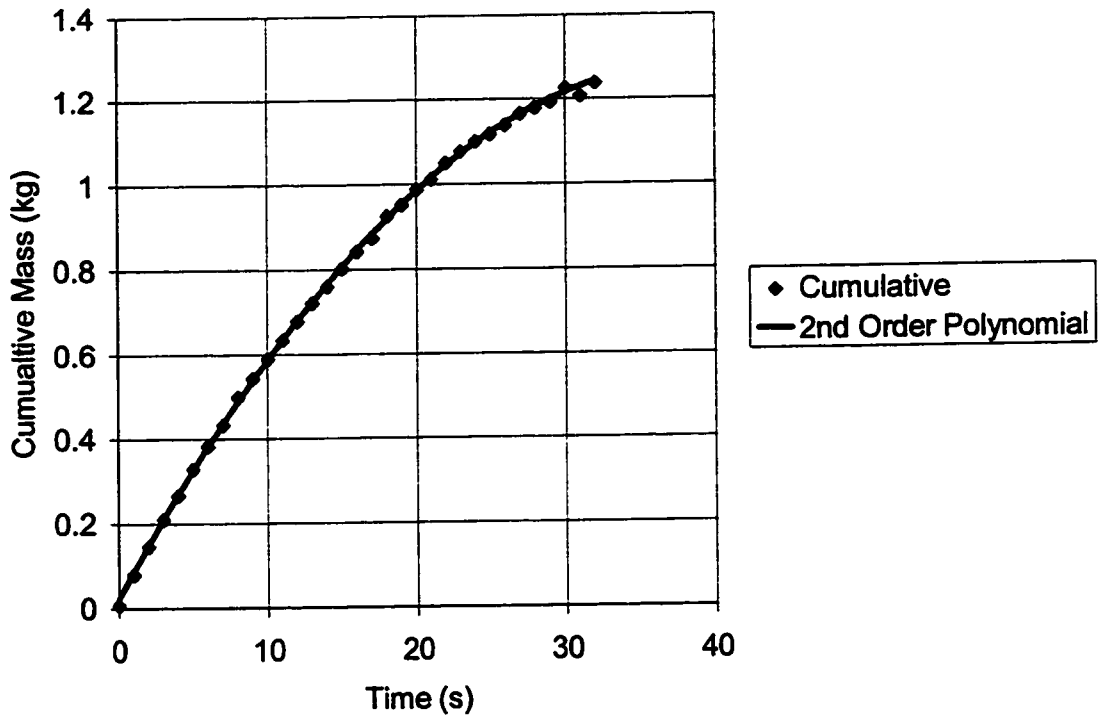


**Figure 5.13: Cumulative mass versus time for aluminum at 1073 K. Aluminum Test #32.**

#### *Measuring Discharge Coefficient*

Water was used as a calibration fluid to determine the frictional characteristics of the graphite orifice used for the aluminum and AZ91D tests. The results for two separate calibrations are presented in Figure 5.14. The aluminum experiments were performed in a regime on the curve that is approximately linear. For  $4000 < Re < 13000$ , a linear model is applied to approximate the frictional characteristics of the orifice.

$$C_{d,poly} = 2.196e^{-6}(Re) + 0.914 \quad (160)$$

This relationship indicates that constants a, and b in Equation (112) are equal to zero, and that c and d are  $2.196 \times 10^{-6}$  and 0.914 respectively. This is valid for  $4000 > Re > 13000$ . The linear model is illustrated in Figure 5.14 over this Reynolds number range. Since the majority of data points are scattered around the function, it is assumed that the linear

approximation is valid for this range of Reynolds numbers. The standard deviation of Equation (160) with respect to the 95 data points is range is:

$$\delta C_d = \sqrt{\frac{\sum (C_{d,poly} - C_{d,exp})^2}{n - 2}} = 0.0023 \quad (161)$$

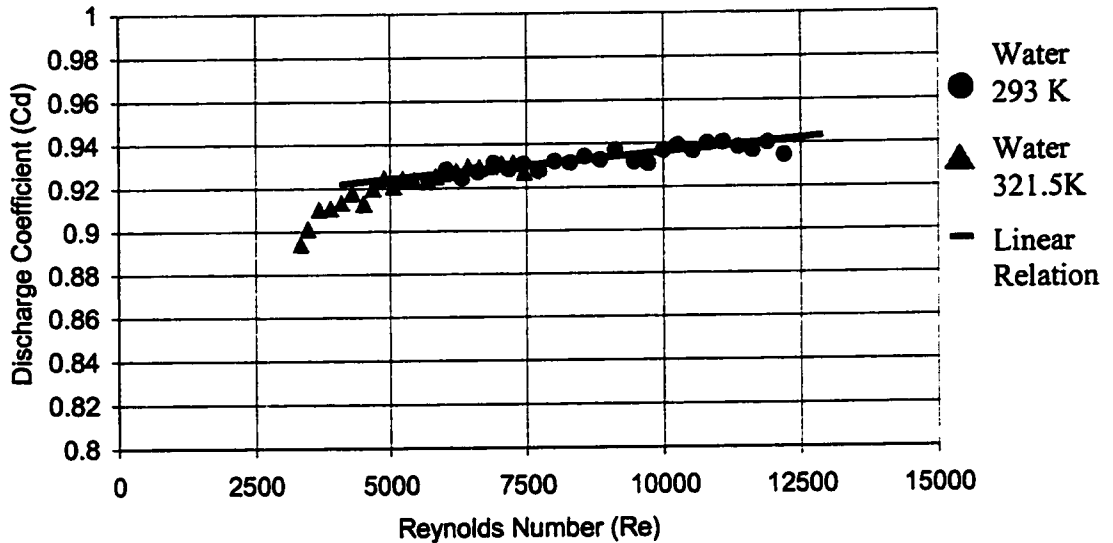


**Figure 5.14: Frictional characteristics of 0.005m orifice used for high temperature experiments.**

### 5.2.3 The Surface Tension, Viscosity and Density of Aluminum at 1073 K

Using the multiple non-linear regression analysis formulation developed in this Chapter, the surface tension, viscosity and density were determined for a system of aluminum at 1073 K. The propagation of errors analysis is also included to determine which experimental errors are relevant in the analysis of aluminum. Density values quoted from Iida and Guthrie [2] were used to estimate the head. The uncertainty in this approach will be discussed with the presentation of the density results.

### *Surface Tension*

The calculated surface tension of aluminum at 1073 K is presented in Figure 5.15. The values indicate an average surface tension of 0.842N/m with a standard deviation of 0.020N/m. The propagation of errors analysis predicts that the error is 0.030N/m. Reynolds numbers of this experiment were between  $4000 < Re < 13000$ , validating the linear assumption of the discharge coefficient. It is believed that the scatter depicted is directly related to error in head measurements. It has been stated in section 5.1.1 that error in head results in random deviations from an average value, while errors in discharge coefficient and flow rate are of a systematic nature and deviate in one direction. It is clear also, that errors are not a function of the processing variables ( $h$ ,  $Q_{exp}$ ,  $C_d$ ). Finally, using propagation of errors, results seem to be confined within the solid lines representing the predicted error in surface tension.

### *Viscosity*

Results for the viscosity in the same experiment are presented in Figure 5.16. The average value is  $5.22 \times 10^{-4} \text{ Ns/m}^2$  with a standard deviation of  $0.35 \times 10^{-4} \text{ Ns/m}^2$ . Again, the random scatter is related to errors in head measurements. The propagation of errors analysis, depicted by the solid lines in Figure 5.12, indicates that results are dependent on processing variables to a certain extent. From theory and experimental evidence, it is clear that as head decreases, that errors become more significant. This confirms the propagation of errors analysis with respect to at least one variable. Equation (144) indicates that large head conditions are favorable to the calculation.

## Density

The experimental density calculation for aluminum at 1073 K is represented in Figure 5.17. The average density is  $2361 \text{ kg/m}^3$  with a standard deviation of  $46 \text{ kg/m}^3$ . Errors associated with head are prevalent from the random scatter of the results. Similar to measuring surface tension, it can be seen that there is no dependency on head as results and propagation of errors indicate. The paradox in using known density information in determining head will now be addressed. An iterative approach is taken to calculate the properties using published or estimated values as an initial guess. The new density value that is obtained from the first iteration is used in repeating the calculation. The iterative process is repeated until density does not change appreciably (i.e. converges). For the purposes of these experiments, the convergence criterion was decided to be less than one percent. The results from this approach are shown in table 5.3. It is clear that properties rapidly converge to the true experimental values. The relative error in density after applying data from Iida and Guthrie [2] is 0.5 %. This is deemed acceptable for all subsequent properties reported in this thesis. Therefore, density data from the literature is used to determine experimental head from the mass that is left in the crucible.

**Table 5.3: Physical properties of aluminum determined by using different density values to calculate head at 1073 K.**

Property	$\rho = 2328 \text{ kg/m}^3$ (Iida and Guthrie [2])	$\rho = 2361 \text{ kg/m}^3$ (2 <sup>nd</sup> iteration)	$\rho = 2371 \text{ kg/m}^3$ (3 <sup>rd</sup> iteration)
Surface tension (N/m)	$0.842 \pm 0.020$	$0.853 \pm 0.016$	$0.850 \pm 0.016$
Viscosity (Ns/m <sup>2</sup> )	$5.22 \times 10^{-4} \pm 0.35 \times 10^{-4}$	$5.26 \times 10^{-4} \pm 0.36 \times 10^{-4}$	$5.18 \times 10^{-4} \pm 0.36 \times 10^{-4}$
Density (kg/m <sup>3</sup> )	$2361 \pm 46$	$2371 \pm 46$	$2370 \pm 46$



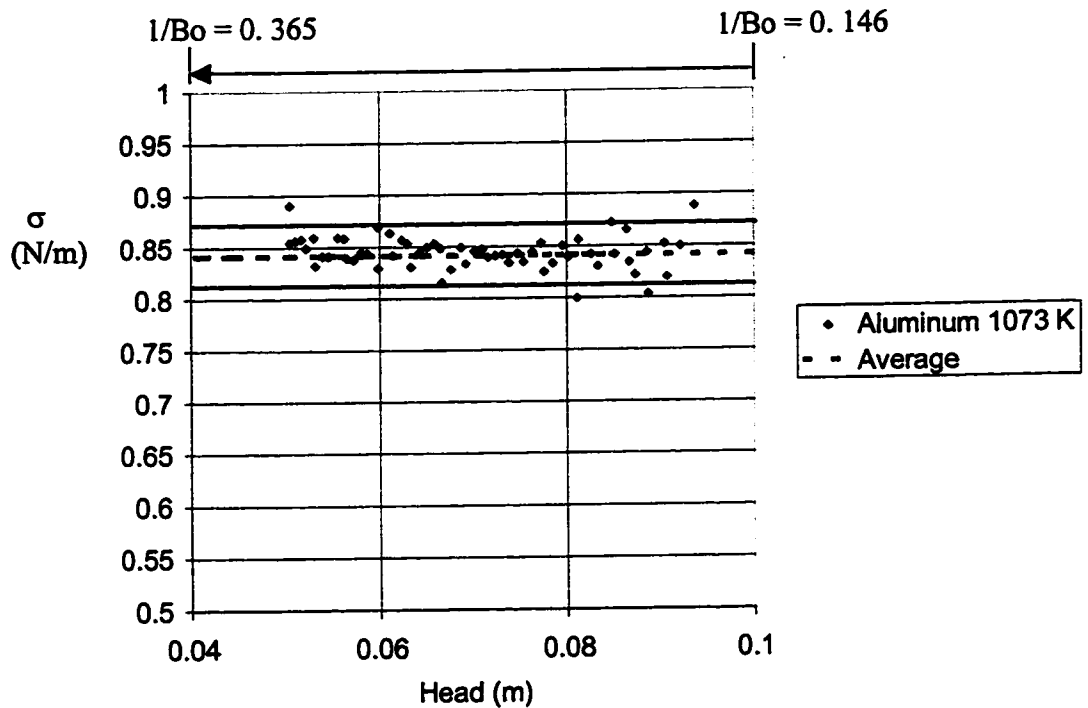


**Figure 5.15: The experimental surface tension determined for aluminum at 1073 K, with expected error represented by the solid bars. Aluminum Test #32.**

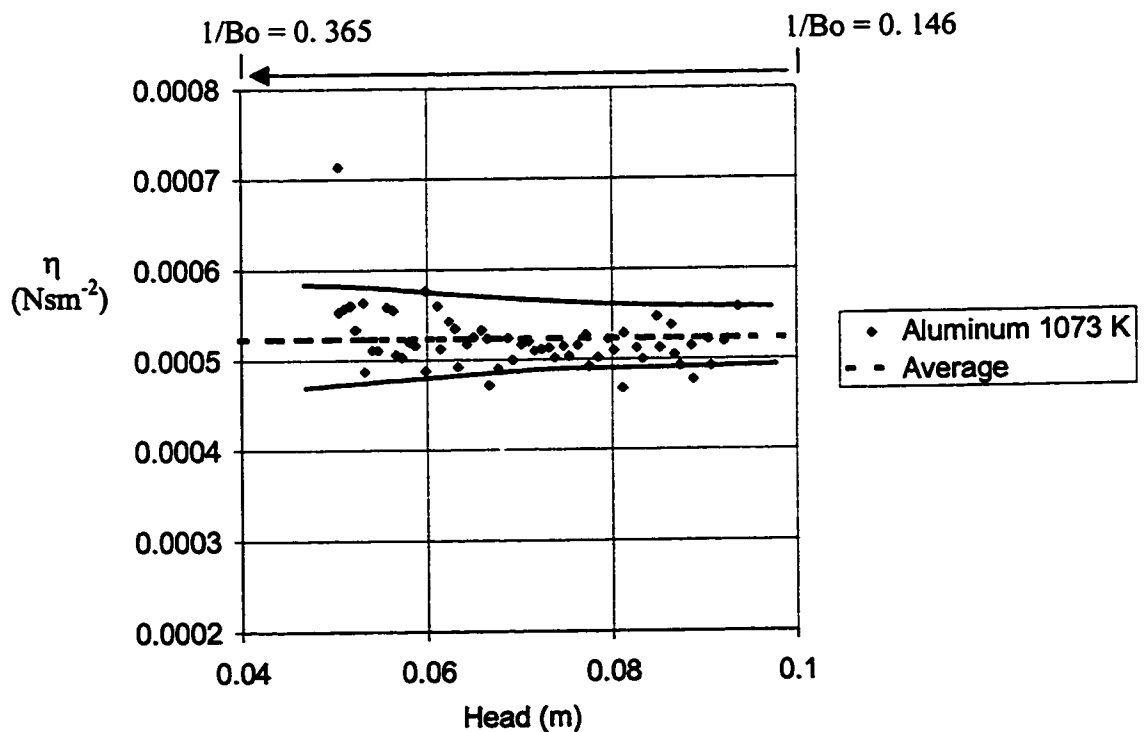


**Figure 5.16: The experimental viscosity determined for aluminum at 1073 K, with expected error represented by the solid bars. Aluminum Test #32.**

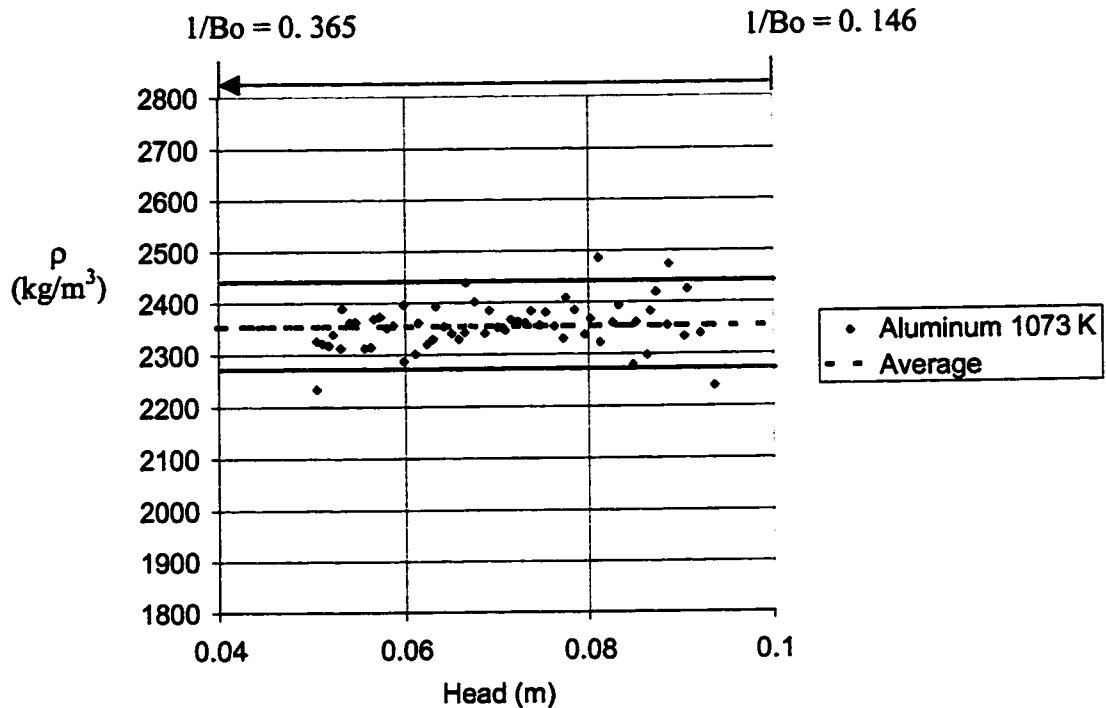


**Figure 5.17: The experimental density determined for aluminum at 1073 K, with expected error represented by the solid bars. Aluminum Test #32.**

### 5.3 Conclusions

The surface tension of water at 321.5 K has been successfully calculated within 2% of the theoretical and accepted value reported in the literature. This is an important validation of the formulation presented in this chapter. It was determined that the method and equipment used in the low temperature work is particularly susceptible to errors associated with the calibration of the discharge coefficient curve. Using propagation of errors analysis, the standard deviation between four independent calibrations was used to successfully predict the deviation in the surface tension measurement. This exercise not only determines appropriate processing conditions, it reinforces the legitimacy of the model as well.

The surface tension, viscosity, and density of 99.95% purity aluminum have been determined at 1073 K. This was accomplished by taking advantage of the fact that voluminous data is collected during the course of an experiment, which facilitates simultaneous measurements to be made on all three properties using multiple non-linear regression analysis. Errors associated with head height were determined to be the predominant source of inaccuracy in the measurement of all three properties. This was determined experimentally, and predicted utilizing propagation of errors theory as well. The physical properties of 99.95% purity aluminum at 1073 K are summarized in Table 5.4 and compared with sources in the literature. Recall that these values are produced by using density values from Iida and Guthrie [2] to determine experimental head from the mass that is left in the crucible.

**Table 5.4: Summary of results for aluminum at 1073 K in comparison to literature quantities.**

Surface Tension (N/m)		Viscosity (Nsm <sup>-2</sup> )		Density (kg/m <sup>3</sup> )	
Keene [7]	This Study	Smithells [17]	This Study	Iida and Guthrie [2]	This Study
0.864	0.842 ± 0.020	1.10x10 <sup>-3</sup>	5.22x10 <sup>-4</sup> ± 0.35x10 <sup>-4</sup>	2328	2361±46
% Diff	2.55%	% Diff	52.5%	% Diff	1.23%

The results for surface tension and density are in reasonable agreement with data quoted from Keene [7] and Iida and Guthrie [2] respectively. However, it is clear that there is a significant difference in the value of the viscosity reported in this work compared to that obtained from Smithells [17]. This is not the first instance that such a discrepancy has been reported when studying the viscosity of melts. In fact, and as was discussed in Chapter 2, a definitive quantity for the viscosity of pure aluminum has not been firmly

established as of yet. This technique provides a unique opportunity to shed light onto these differences as will be shown in the next chapter. The next chapter will also explore results of implementing this formulation for aluminum and AZ91D alloy over a range of temperatures. This is attractive from the point of view of surface tension, since the dynamic nature of the experiment produces an interface that is rapidly replenished. The measurements are thus considered to reflect, more closely, the pure dynamic surface tension that was described in Section 2.1.3 (i.e. no oxygen contamination).

## **CHAPTER 6: DISCUSSION**

The unique approach to measuring the surface tension, viscosity and density, validated in the previous chapter, will now be utilized to determine the temperature dependence of these properties for 99.95% aluminum and AZ91D alloy. There are two purposes of this discussion. The first is to relate results of molten aluminum with data available in the literature. The second is to present results for AZ91D alloy, and to provide an analysis on the effects of metallic alloys on these properties.

### **6.1 Density**

Density was determined through implementing multiple non-linear regression analysis on all three physical properties. Regression was performed using data corresponding to  $4000 < Re < 13000$  (refer to Figure 5.14). The experimental Reynolds numbers were approximated using density and viscosity information from Iida and Guthrie [2] and Smithells [17]. There is undoubtedly uncertainty with respect to  $Re$ ; however, imposing this constraint on the data ensures that the linear portion of the discharge coefficient is used to calculate properties. The values from Iida and Guthrie were also used to determine head from knowledge of cumulative mass data.

### 6.1.1 Density of Aluminum

Tests were conducted with aluminum between 973 K and 1173 K so that the effects of temperature could be determined. The data is shown in Table 6.1 with error bars corresponding to the standard deviation similar to the analysis presented in Figure 5.17.

**Table 6.1: Density of 99.95% aluminum determined experimentally.**

Test	Temperature (K)	$\rho$ (kg/m <sup>3</sup> )
Aluminum #23	983	2352±64
Aluminum #25	1169	2342±74
Aluminum #26	1165	2353±29
Aluminum #28	971	2439±48
Aluminum #30	1070	2380±55
Aluminum #31	973	2362±42
Aluminum #32	1075	2361±59
Aluminum #33	1165	2330±38
Aluminum #34	1019	2374±34
Aluminum #35	1074	2385±51
Aluminum #36	973	2369±50
Aluminum #39	1165	2379±48

The data presented in Table 6.1 is plotted in Figure 6.1. Sources from the literature are included for comparison [2,17].

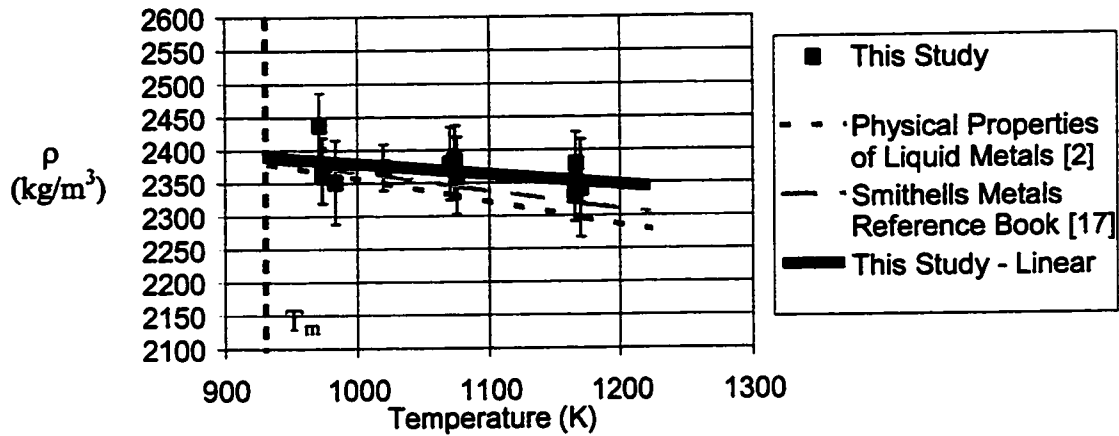


**Figure 6.1: Density of 99.95% aluminum as a function of temperature and compared with sources in the literature [2,17].**

Recall from Chapter 2 (Section 2.1.5) that density is usually expressed as a linear function of temperature. By fitting a linear relationship to the data in Figure 6.1, a new function is produced and illustrated in Table 6.2. Results from this study are in excellent agreement with literature at the melting point. Evidently, this study yields a lower dependence on temperature. At 1173 K; however, variation between the three relationships is no greater than 2.5%. This is an important outcome in terms of validation of this model. By measuring flow rate and head, the density of 99.95% aluminum was successfully determined using concise knowledge of the discharge coefficient curve.

**Table 6.2: Temperature dependence of density determined from experiments and from sources in the literature [2,17].**

Source	Density at melting point, $\rho_m$ ( $\text{kg/m}^3$ )	Temperature dependence of density, $d\rho/dT$ ( $\text{kgm}^{-3}\text{K}^{-1}$ )
Iida and Guthrie [2]	2380	-0.35
Smithells [17]	2385	-0.28
This Study	2390	-0.15

### 6.1.2 Density of AZ91D

The Density of AZ91D was determined between 923 K and 1173 K and the results are presented in Table 6.3.

**Table 6.3: Density of AZ91D alloy determined experimentally.**

Test	Temperature (K)	$\rho$ (kg/m <sup>3</sup> )
AZ91D #2	967	1699±113
AZ91D #4	1067	1621±89
AZ91D #5	1169	1599±84
AZ91D #6	921	1606±55
AZ91D #7	954	1659±54
AZ91D #9	921	1632±57

In order to compare density with literature quantities, the approximation for atomic volumes of metallic mixtures is used. Recall Equation (51) from section 2.3 in Chapter 2:

$$v = \sum_i x_i v_i \quad (51)$$

On the basis of this function, the alloy is predominately made of aluminum (~9 wt%) and magnesium (~91 wt%). Refer to Table 3.3 in section 3.2.5. Since the atomic volume corresponding to Equation (51) is based on a molar basis, the wt% must be converted to a molar fraction. For AZ91D alloy,  $x_{\text{mg}} = 0.90$  and  $x_{\text{al}} = 0.10$ . Manganese and zinc are neglected from this analysis since they are present at low levels relative to magnesium



and aluminum. The values for the density of aluminum and magnesium are referenced from Smithells [17] and are used in Equation (51).

$$\begin{aligned} v_{AZ91D} &= x_{Mg} \left( \frac{M_{Mg}}{\rho_{Mg}} \right) + x_{Al} \left( \frac{M_{Al}}{\rho_{Al}} \right) \\ &= 0.90 \left( \frac{24.31}{(1590 - 0.264(T - 913))} \right) + 0.1 \left( \frac{26.98}{(2385 - 0.26(T - 933))} \right) \end{aligned} \quad (162)$$

Recall the liquidus temperatures for magnesium and aluminum are 913 K and 933 K respectively. The average molecular weight is determined from the following:

$$\frac{1}{M_{AZ91D}} = x_{Mg} \frac{1}{M_{Mg}} + x_{Al} \frac{1}{M_{Al}} = 0.03706 \quad (163)$$

The molecular weight of AZ91D alloy is:

$$M_{AZ91D} = 26.98 \text{ kg/mole} \quad (164)$$

Equation (164) is divided by values obtained from Equation (162) to obtain the density of AZ91D alloy. The following function describes the density as a function of temperature:

$$\rho_{AZ91D} = 1648 - 0.268(T - 903) \quad (165)$$

The liquidus temperature for AZ91D alloy is 903 K and was obtained from a binary aluminum-magnesium phase diagram [49]. Figure 6.2 presents the results obtained in this study. Included is the expression represented in Equation (165) (indicated by the predicted function) and the density of pure magnesium [17].

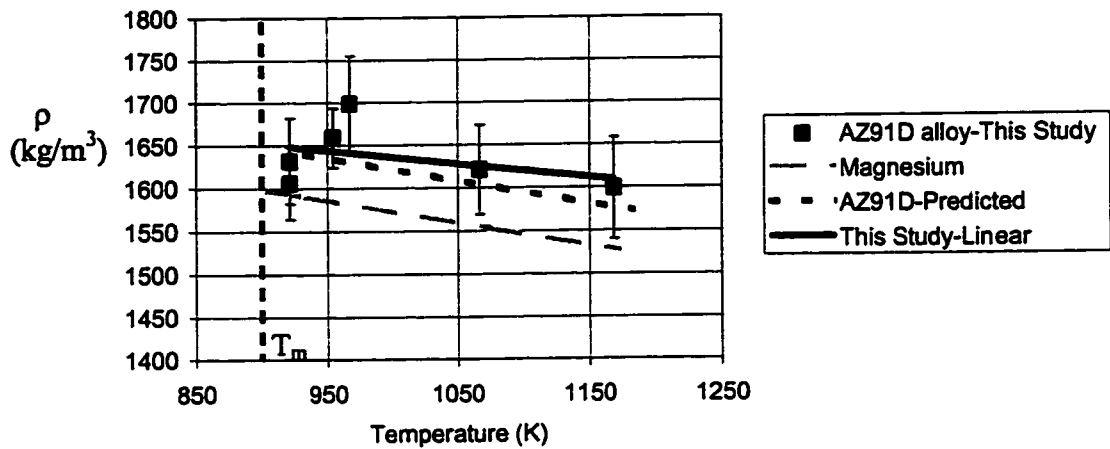


**Figure 6.2: Density of AZ91D alloy as a function of temperature compared with theoretical relations [17].**

The outcome in Figure 6.2 contributes significantly to the merits of this technique. Clearly, the data is within reasonable agreement with the theoretical relation based on the approach represented by Equation (165). There are essentially two key issues related to the density of AZ91D alloy. First, the technique successfully quantifies the addition of an alloying element since density obtained is significantly higher than the density for pure magnesium. This conclusion is important for establishing confidence in the formulation and execution of the technique. Secondly, the results confirm that metallic alloys behave ideally and that densities are additive [2].

A linear relation describing the data is presented in Table 6.4. The theoretical model based on the molar average of the magnesium-aluminum mixture is included for comparison.

**Table 6.4: Temperature dependence of density determined from experiments, and from the average values taken from sources in the literature [17].**

Source	Density at melting point, $\rho_m$ (kg/m <sup>3</sup> )	Temperature dependence of density, $d\rho/dT$ (kgm <sup>-3</sup> K <sup>-1</sup> )
Equation (165) (Theory)	1648	-0.268
This Study (Experimental)	1651	-0.16

Recall:  $\rho = \rho_m + d\rho/dT(T-T_m)$

The results presented in this section used multiple non-linear regression on all three properties. Appendix C presents results for the surface tension and viscosity of aluminum using this regression analysis. Subsequent sections, however, will present results where only surface tension and viscosity are calculated from regression analysis on only two properties. The density relationships developed in this study for both aluminum and AZ91D alloys (Tables 6.2 and 6.4) were implemented in the formulation. Refer to Appendix B for this program. It will be clarified in section 6.3.1 that a more reliable analysis describing  $d\sigma/dT$  is obtained when comparing results in Appendix C with results obtained from regression on only two properties.

## 6.2 Viscosity of Aluminum and AZ91D Alloy

The viscosities for both 99.95% aluminum and AZ91D alloy were determined through multiple non-linear regression analysis on surface tension and viscosity only. This was the procedure defined for data analysis so that errors in the density measurement would not result in systematic differences in the surface tension or viscosity calculations. It is seen in Appendix C, however, that there is little difference between results obtained with regression on all three variables and results obtained in this section.

Theoretical viscosities of aluminum and AZ91D alloy were calculated using the formulation presented in Section 2.2.1. Recall Equations (46-48):

$$\eta = A \exp(B / RT) \quad (46)$$

$$B = 2.65T_m^{1.27} \quad (47)$$

$$A = \frac{1.7 \times 10^{-7} \rho_m^{2/3} T_m^{1/2} M^{-1/6}}{\exp\left(\frac{2.65T_m^{0.27}}{R}\right)} \quad (48)$$

Using the methods outline by Hirai [3], the constants A and B were determined using the molar averages for  $\rho_m$  and M. The alloy is assumed to be predominately made of 10 % aluminum and 90 % magnesium (molar basis).

Results for the viscosity of 99.95% purity aluminum and AZ91D are presented in Table 6.5 and 6.6 respectively.

**Table 6.5: Viscosity of 99.95% aluminum determined experimentally.**

Test	Temperature (K)	$\eta$ (Nsm <sup>-2</sup> )
Aluminum #31	973	(5.10±1.80)x10 <sup>-4</sup>
Aluminum #32	1075	(5.15±0.747)x10 <sup>-4</sup>
Aluminum #33	1165	(5.10±0.340)x10 <sup>-4</sup>
Aluminum #34	1019	(5.03±0.327)x10 <sup>-4</sup>
Aluminum #35	1074	(5.64±2.22)x10 <sup>-4</sup>
Aluminum #36	973	(5.35±1.07)x10 <sup>-4</sup>
Aluminum #38	1020	(4.72±0.5.0)x10 <sup>-4</sup>
Aluminum #39	1165	(5.24±0.411)x10 <sup>-4</sup>

**Table 6.6: Viscosity of AZ91D alloy determined experimentally.**

Test	Temperature (K)	$\eta$ (Nsm <sup>-2</sup> )
AZ91D #2	967	$(2.66 \pm 0.397) \times 10^{-4}$
AZ91D #4	1067	$(2.39 \pm 0.484) \times 10^{-4}$
AZ91D #5	1169	$(2.93 \pm 1.72) \times 10^{-4}$
AZ91D #6	921	$(8.46 \pm 0.124) \times 10^{-4}$
AZ91D #7	954	$(4.03 \pm 0.972) \times 10^{-4}$
AZ91D #9	921	$(7.85 \pm 1.52) \times 10^{-4}$

These results are presented in Figures 6.4 and 6.5 with values obtained from the literature and the theoretical calculations:

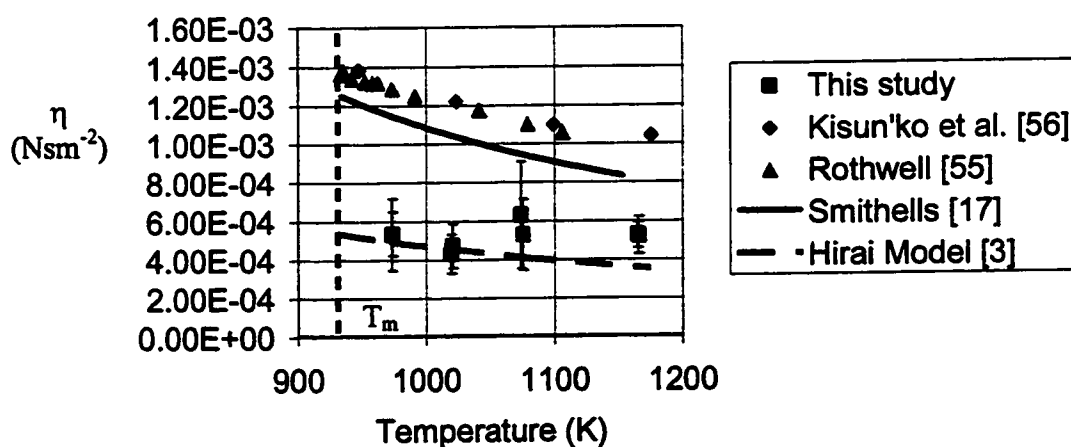


**Figure 6.3: Viscosity of 99.95% purity aluminum as a function of temperature compared with sources in the literature.**

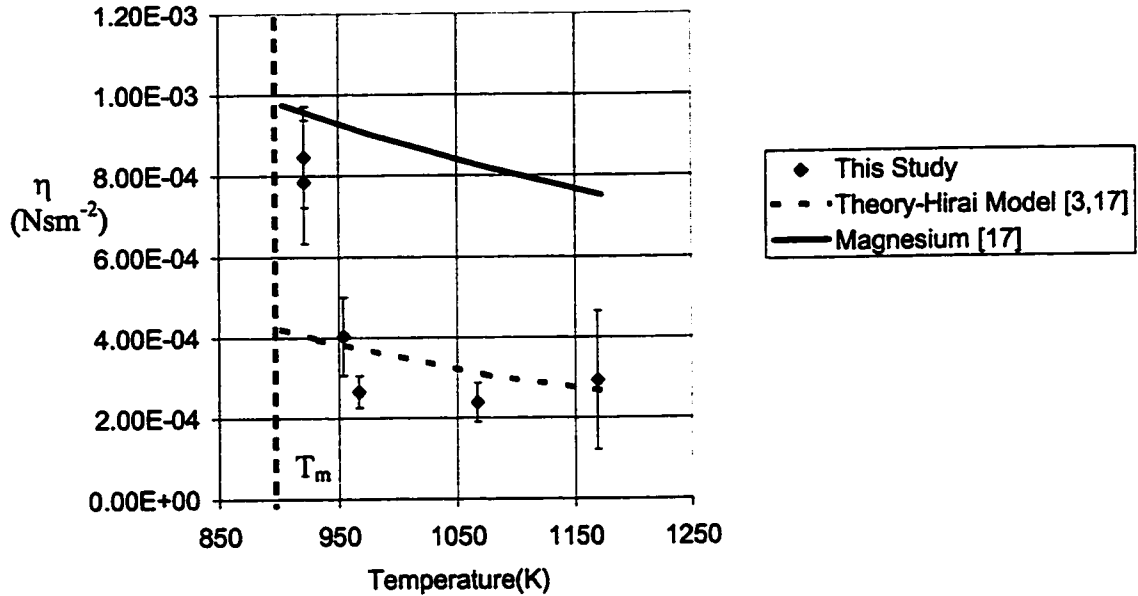


**Figure 6.4: Viscosity of AZ91D as a function of temperature.**

The experimental values for aluminum obtained from Rothwell [55], Kisun'ko et al. [56], and Smithells [17] are presented for comparison. The viscosity of aluminum has a small temperature dependence as shown in Figure 6.3. With AZ91D, temperature has little impact above 973 K. As the temperature decreases and approaches the liquidus point (903 K), however, the viscosity sharply increases. This sharp increase near the liquidus point has been observed experimentally by different researches [53,54]. These references dealt exclusively with aluminum based alloys; however, there hasn't been verification of this phenomenon for AZ91D alloy near the liquidus point in the literature. Results for aluminum are significantly lower than the experimental values obtained from other sources. AZ91D also exhibits low viscosities relative to pure magnesium referenced in the literature. The unique flow conditions in this technique must be

emphasized in comparison with other methods. Traditionally, techniques rely on laminar flow such that the viscosity is a constant relating shear stress with velocity gradient. This is an essential criterion for the measuring techniques described in Section 2.2.2 [2]. The gradient is unidirectional and produced from the laminar no-slip condition. Recall Equation (44) from Chapter 2:

$$\tau_s = \eta \frac{du}{dz} \quad (44)$$

The capillary, oscillating-vessel, rotational, and oscillating plate method all rely on this principle. Kisun'ko et al. used rotational principles and Rothwell used the principle of the oscillating plate method (using a sphere instead) [55,56]. The technique formulated in this study, however, is performed with Reynolds numbers in excess of 4000. This clearly indicates that turbulent conditions dictate the dynamics of the process. Further analysis into the flow conditions of these experiments must be made before a definitive explanation of the viscosity results is given. Such an analysis is beyond the scope of this study, however. There appears to be reasonable agreement with values obtained in this study and the theoretical formulations presented in Table 6.5 and 6.6. The approach taken by Andrade [48] to derive the theoretical expression is based on atomic vibration mechanisms, and not the principle stated by Equation (44). The formulation of the theoretical approach and how it may relate to this method is also beyond the scope of this study. Similar to the Saybolt instrument described in Section 2.4, experiments at lower Reynolds numbers (< 1500) may be considered to determine if experimental viscosities would reflect values determined using conventional methods. Unfortunately, the dynamics of this method makes it difficult to generate such low Reynolds numbers. This

is especially the case with molten metals where densities are particularly high with respect to viscosity.

### **6.3 Surface Tension**

Similar to the viscosity calculation, the surface tension of 99.95% aluminum and AZ91D alloy was determined using multiple non-linear regression analysis on only viscosity and surface tension. It is seen in Figure C.1 in Appendix C that for multiple non-linear regression on all three properties, modified results are obtained compared with results in this section. The following presents results for aluminum and AZ91D alloy and provides a discussion into their magnitude and dependence on temperature.

#### **6.3.1 Surface Tension of Aluminum**

Under equilibrium conditions with aluminum, the partial pressure of oxygen must be below  $10^{-44}$  atm [38] ( $10^{-39}$  Pa) to completely avoid oxidation (Recall Section 2.15 in Chapter 2). Oxygen contamination is surely expected since oxygen is present in these experiments at levels no less than 2Pa (20ppm). Due to the highly dynamic conditions of these experiments; however, it is possible that results are closer to the “pure dynamic surface tension” (or the surface tension at the instant that the surface is created [5]). If so, it is expected that unusually high surface tension values, corresponding to un-oxidized aluminum will be produced. Similarities between the results obtained from Goumri and Joud [32] (1.050N/m at 973 K) and calculated from Chacón [37] (1.184N/m) will be



expected if the rate at which the surface is replenished is faster than mass transfer and kinetic issues controlling oxidation. Table 6.7 presents results.

**Table 6.7: Surface tension of 99.95% aluminum determined experimentally.**

Test	Temperature (K)	$\sigma(\text{N/m})$
Aluminum #31	973	$0.846 \pm 0.015$
Aluminum #32	1075	$0.8355 \pm 0.020$
Aluminum #33	1165	$0.709 \pm 0.011$
Aluminum #34	1019	$0.833 \pm 0.012$
Aluminum #35	1074	$0.794 \pm 0.017$
Aluminum #36	973	$0.845 \pm 0.018$
Aluminum #38	1020	$0.872 \pm 0.020$
Aluminum #39	1165	$0.820 \pm 0.017$

The data in Table 6.7 is presented in Figure 6.5. Included are the relationships proposed by Keene [7] and presented in Iida and Guthrie [2]. The surface tension of “pure” aluminum obtained from Gourmiri and Joud [32] is included as well. There are a number of issues pertaining to Figure 6.5. It is immediately evident that the surface tension of 99.95% aluminum, determined using this method, is closer to the oxidized values as determined from a variety of sources [10,17-34]. This is an indication that there is a certain degree of oxidation on the surface of aluminum at the moment the stream exits the orifice. This illustrates the difficulties in measuring the “pure dynamic surface tension” of molten metals, even under the most dynamic circumstances.

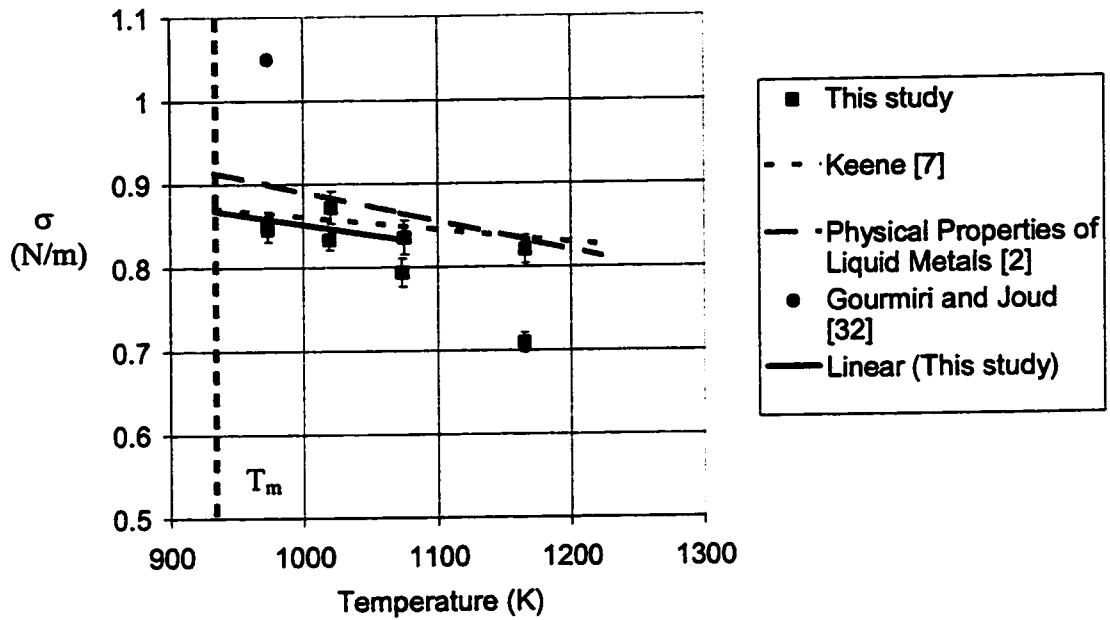


**Figure 6.5: Surface tension of 99.95% aluminum as a function of temperature compared with sources in the literature [2,7,32].**

There appears to be inconsistency in the data at higher temperatures. A variety of concepts have been considered to explain such irregularities. The purity of the aluminum (99.95%) was scrutinized so that the possibility of increasing activity of surface acting contaminants with temperature could be considered. The purity of the aluminum that previous researchers used was typically of a much higher quality. Table 2.1 in Chapter 2 indicates a number of sources in which the purity of the aluminum used is approximately 99.999%. Referring to Table 3.2 in Chapter 3, two major contaminants found in the aluminum used in this study are iron (0.0038%) and silicon (0.037%), two elements that exhibit essentially no surface activity [11]. The only element that affects the surface tension of aluminum considerably is lead that is present at levels  $< 0.0001\%$ .

A plausible explanation is that the variation in surface tension at increasing temperatures is due to increasing reactivity of oxygen. Refer to Appendix D for insight into the oxygen partial pressure in the apparatus for these tests. From the data given in Appendix D, the oxygen content appears to decrease significantly at temperatures above 1073 K when heating. This suggests that there are repeatability issues at higher temperatures concerning the oxygen content of the apparatus. For this reason, results between 973 K and 1073 K were only considered in determining the experimental relationship indicated in Figure 6.5 and presented in Table 6.8. The relationship quoted from Iida and Guthrie is based on data generated from one source. It is an important validation of the technique developed in this study to generate results that are more closely related to the formula developed by Keene, which is based on 20 independent sources [10,17-34]. In considering results between 973 K and 1073 K, the differences between Keene and this study are no greater than 6.5%.

**Table 6.8: Temperature dependence of surface tension determined from experiments and from sources in the literature [2,7,17].**

Source	Surface tension at melting point, $\sigma_m$ (N/m)	Temperature dependence of surface tension, $d\sigma/dT$ (Nm <sup>-1</sup> K <sup>-1</sup> )
Iida and Guthrie (1988); and Smithells (1998)	0.914	-0.35x10 <sup>-3</sup>
Keene (1996)	0.871	-0.155x10 <sup>-3</sup>
This Study	0.868	-0.25x10 <sup>-3</sup>

Recall from chapter 2:  $\sigma = \sigma_m + d\sigma/dT(T-T_m)$

### 6.3.2 Surface Tension of AZ91D Alloy

Unlike density and viscosity, the surface tension of metallic alloys is very rarely an additive property of the percentages of the alloying elements. AZ91D is used in this analysis to determine the effects of alloying elements on the surface tension of pure magnesium. The results from this analysis are presented at various temperatures in Table 6.9.

**Table 6.9: Surface tension of AZ91D alloy determined experimentally.**

Test	Temperature (K)	$\sigma$ (N/m)
AZ91D #2	967	0.539 $\pm$ 0.035
AZ91D #4	1067	0.556 $\pm$ 0.028
AZ91D #5	1169	0.590 $\pm$ 0.030
AZ91D #6	921	0.657 $\pm$ 0.022
AZ91D #7	954	0.662 $\pm$ 0.022
AZ91D #9	921	0.605 $\pm$ 0.022

These values are illustrated in Figure 6.6 with data in the literature for pure magnesium [17] and the available results in the literature corresponding to Mg-Al-Zn-Mn alloys [58]. The concentrations of alloying elements from Patrov et al. that were presented in Table 2.5 in Chapter 2 are included in Figure 6.6. Given the ranges presented in Figure 6.6, it is a reasonable assumption that AZ91D alloy would be within the range that is presented.

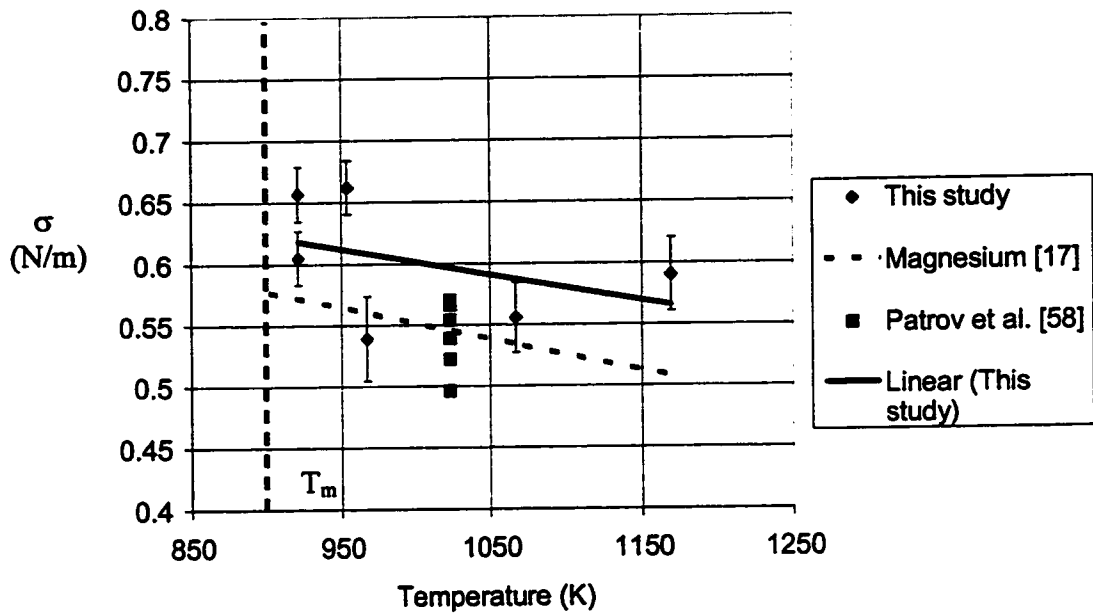


**Figure 6.6: Surface tension of AZ91D as a function of temperature compared with sources in the literature [17,58].**

A linear regression is fitted to the data. Due to lack of data and the variation between values; however, the results are considered inconclusive. There appears to be a high degree of scatter between experimental data points making the argument that repeatability may be an issue. Similar to measurements with aluminum at high temperatures ( $>1073\text{K}$ ), large fluctuations in oxygen partial pressure were observed during heating of the alloy. Figure D.6 in Appendix D illustrates the decrease in oxygen content after the alloy experiences melting. Nevertheless, considering the magnitude of the linear relationship, higher surface tension values indicate that the surface tension of magnesium appears to be affected by alloying additions of aluminum, zinc and manganese. At the liquidus point (903 K) the surface tension of the experimental linear relation is 8% higher than the case of pure magnesium. Due to complexities of the four-

component system, and the lack of thermodynamic activity information for this system, it is not possible to make a quantitative analysis of these results. Data from Patrov et al. indicate that the surface tension of magnesium alloys of similar composition is lower than the linear relationship proposed in Figure 6.5. Speculation can be made, due to the seemingly lower experimental values at  $\sim 973$  K and  $\sim 1073$  K, that a minimum may exist between these temperatures. Such would be an indication of complex interactions between the components in the alloy as temperature is increased. Further studies must be made using this technique to confirm whether the surface tension is approximately a linear relation with temperature, or if a minimum exists.

#### **6.4 Conclusions**

The results presented in this chapter have achieved, with varying degrees of success, the goals of performing experiments using molten aluminum and AZ91D alloy. The results for density have provided important validation to the technique in confirming that the density of 99.95% aluminum is in reasonable agreement with relationships available in the literature. Furthermore, using AZ91D alloy, it was determined that not only can the density of an alloy be experimentally determined using this method, but that a molten metallic alloy behaves as an ideal fluid in terms of additive density. The surface tension of aluminum has been confirmed to reflect the oxidized values that have been widely reported in the literature. Despite the highly dynamic nature of these experiments, the “pure dynamic surface tension” was not obtained using this method. Results are within reasonable agreement with previous studies and contribute to the validation of the

experimental method. However, more work must be performed in providing a definitive understanding of the surface tension of AZ91D alloy as a function of both temperature and composition. Also, in terms of viscosity, consideration into the highly turbulent conditions must be made to determine whether or not the true viscosity is calculated using this method.

## CHAPTER 7: SUMMARY

Experiments performed in this study have focused on an experimental system that has traditionally neglected surface tension. Using the analysis of a draining vessel through a small orifice (0.002m-0.005m), it has been confirmed experimentally that surface tension plays a fundamental role under various circumstances. The traditional energy balance, that is used to calculate the discharge coefficient, is insufficient in terms of characterizing frictional losses for certain liquids under certain processing conditions. The new model developed in this study is an extension of the traditional energy balance that includes a surface tension term in the formulation. The following conclusions have been made from experimental results:

1. The new formulation is relevant for low-density liquids with high surface tensions compared with high-density and low surface tension liquids.
2. The new formulation is relevant, from the perspective of design and operation, for small orifice radii operating under low head conditions compared with large orifice radii under high head conditions.
3. Low Bond numbers are an indication of conditions where the new formulation is most relevant (i.e.  $Bo = \rho g r h / \sigma$ ).
4. Molten metals should be considered in the new formulation more often than low temperature fluids due to larger surface tension values.

This approach can be used to calculate the physical properties of liquids since surface tension, viscosity and density are inherent in the formulation. By accurately measuring flow rate and head, these properties are determined using multiple non-linear



regression analysis. There is a statistical advantage to this technique over conventional methods since a vast amount of data is used to calculate the properties (due to varying head and flow rate). This technique is useful for molten metals because of the relatively simple design of the equipment, coupled with the simultaneous measurement of all three properties. There are also no optical measurements required. Furthermore, and unlike conventional methods, the surface tension is determined in a highly dynamic situation where the stream is replenished at a very high rate. The following conclusions are drawn:

5. Surface tension of water at 321 K was determined to be  $0.067 \pm 0.002$  N/m, 1.75% lower than values quoted in the literature. Errors associated with discharge coefficient are predominately the source of error.
6. Errors in calculating the surface tension, viscosity and density of molten aluminum in this study are attributed to errors in the determination of head.
7. The calculation of surface tension and density is favorable when low-density/high surface tension liquids operate at low head conditions through small orifice designs exhibiting high discharge coefficients. This is characterized by the Bond number, which accounts for the density-surface tension ratio (i.e.  $Bo = \rho g r h / \sigma$ ). Conditions are favorable when  $1/Bo \rightarrow 1$ .
8. The calculation of viscosity is favorable when high-density/low surface tension liquids operate at high head conditions. Conditions are favorable when  $1/Bo \rightarrow 0$ .

From experiments performed with molten aluminum and AZ91D alloy, the following are concluded:

9. Experimentally, the results for the surface tension of 99.95% aluminum are closely related to the relationship proposed by Keene [7] as a function of temperature, providing an important validation of the technique.
10. The surface tension of 99.95% aluminum reflects the oxidized values that agree with data available in the literature.
11. Experimentally, the surface tension of AZ91D as a function of temperature is approximately 8% higher than the surface tension values for pure magnesium quoted in the literature [7] if a linear estimate is assumed. There is evidence of a minimum in the surface tension as a function of temperature between temperatures of 973 K and 1073 K.
12. Experimentally, the viscosities of 99.95% aluminum and AZ91D alloy are approximately 50% lower than values obtained from the literature [17].
13. Experimentally, the density of 99.95% aluminum agrees reasonably with values obtained in the literature [2,17] and provides an important validation of the technique.
14. The density of AZ91D alloy reflects values predicted using the molar average approach using known data for aluminum and magnesium. This indicates that the metallic alloy behaves as an ideal liquid in this regard and provides further validation.

This technique is considered to be at the initial stages of development. Future work is required in resolving a number of issues. These include lower viscosities obtained in this study with respect to measurements made using conventional methods. Since it was determined in the literature concerning the Saybolt instrument that Reynolds

numbers must correspond to laminar viscous flow, it would be of interest to experiment under similar conditions. Also, more experiments with AZ91D alloy should be performed so that a more detailed discussion can be made into the effects of temperature and composition. However, in light of the results obtained in this study there appears to be significant potential that deserves future consideration. The philosophy behind this method is not to replace conventional methods but to provide an alternative where similar processing conditions may be relevant. As an example, the conditions in this study are very similar to atomization of melts in powder metallurgy. Also this method facilitates measurements at particularly high temperatures. For instance, measuring the surface tension of slag systems ( $> 1500^{\circ}\text{C}$ ) in steelmaking operations will provide information of tremendous practical importance from the perspective of corrosion of refractory material and/or gas adsorption.

Finally, a number of design issues can be made to facilitate more accurate measurements. For instance technology is available to electronically measure the melt head as a function of time. Independent measurements of head and cumulative mass data would reduce systematic errors in the calculation. Also, reducing the level of oxygen in the apparatus can be accomplished through implementing oxygen getters. Such consideration is recommended to improve upon the potential of this unique method.

## REFERENCES

- 1) Lü, Y.Z. Wang, Q.D. Ding, W.J, and Zeng, X.Q: "Fluidity of Mg-Al Alloys and the Effect of Alloying Elements", *Z. Metalkd*, 2000, vol.91, pp. 477-482.
- 2) Iida, T. Guthrie, R. I. L: The Physical Properties of Liquid Metals, Clarendon Press, Oxford, 1988, pp. 77-188.
- 3) Hirai, M: "Estimation of Viscosities of Liquid Alloys", *ISIJ Int.*, 1993, vol.33, pp. 251-258.
- 4) Yule, A.J. Dunkley, J.J: Atomization of Melts: For Powder Production and Spray Deposition, Clarendon Press, Oxford, 1994, p.17.
- 5) Joud, J.C. Passerone, A: "Surface Properties of Liquid Alloys: Thermodynamic Aspects and Chemical Reactivity", *Heterogeneous Chemistry Reviews*, 1995, vol.2, pp.173-211.
- 6) Mukai, K. Wang, Z: "Interfacial Phenomena of High Temperature Melts in Relation to Materials Processing", *J.M. Toguri Symposium: Fundamentals of Metallurgical Processing*, Met Soc, Ottawa, 2000, pp.265-279.
- 7) Keene, B.J: "Review of Data for the Surface Tension of Pure Metals", *International Materials Reviews*, 1993, vol 38, pp.157-192.
- 8) Kaptay, G: "On the Surface Properties of Molten Aluminum Alloys of Oxidized Surface", *Materials Science Forum*, 1991, vol.77, pp.315-330.
- 9) Sakkinen, D.J: "Physical Metallurgy of Magnesium Die Cast Alloys", *Society of Automotive Engineers, Inc*, 1994, pp.71-82.
- 10) Utigard, T: "Surface and Interfacial Tensions of Iron Based Systems", *ISIJ Int.*, 1994, vol.34, pp.951-959.
- 11) Lang, G: "Einflub von Zustzelementen auf die Oberflächenspannung von flüssigem Reinstaluminium", *Aluminium*, 1974, vol.50, pp.731-734. (German)
- 12) Richardson, E.D: Physical Chemistry of Melts in Metallurgy, vol 2. Academic Press, London, 1974, pp.426-439.
- 13) Callen, H.B: Thermodynamics and an Introduction to Thermostatistics, 2<sup>nd</sup> ed., John Wiley and Sons, New York, 1985, p.28.
- 14) Levine, I.N: Physical Chemistry, 3<sup>rd</sup> ed., McGraw Hill, New York, 1988, p.369.

- 15) Whalen, T.J. Kaufman, S.M. Humenik, M: *Trans. Am. Soc. Met.*, vol.58, 1962, p.778.
- 16) Belton, G. R: *Metall Trans.*, vol.3, 1972, p.1465.
- 17) Smithells, C. J: *Metals Reference Book*, 7<sup>th</sup> ed., Oxford, Boston, 1998, p.14-7.
- 18) Gourmiri, L. Joud, J.C: *Surf Sci.*, vol.83, (2), 1979, p.471.
- 19) Levin, E.S. Ayushina, G.D. Gel'd, P.V: "Density and Surface-Energy Polytherms of Liquid (Molten) Aluminum", Translated from *Teplofizika Vysokikh Temperatur.*, vol.6, (3), 1968, pp.432-435.
- 20) Naidich, Y.V, Eremenko, V.N: *Fiz. Met. Metalloved.*, vol.11, (6), p.883.(Russian)
- 21) Popel, S.I. Kozhurkov, V.N. Zhukov, A.A: *Izv. Akad. Nauk SSSR, Met.*, vol.5, 1975, p.69. (Russian)
- 22) Levin, E.S. Ayushina, G.D. Gel'd, P.V. RYSS, M.A. Seryii, V.F: In *Fiz. Khim. Poverkh.Yav. vys. Temp.*, (ed. Eremenko, V.N), Kiev, Naukova Dumka., vol.120, 1971. (Russian)
- 23) Paramanov, V.A. Karamyshev, E.P. Ukhov, V.F: In *Fiz. Khim. Poverkh. Rasp.*, (Colloq on Physics and Chemistry of Surface Melts), vol. 155, Metsniyereba, 1977. (Russian)
- 24) Ayushina, G.D. Levin, E.S. Gel'd, G.D: *Russ. J. Phys. Chem.*, vol.43, (11), 1969, p.1548.
- 25) Davies, V. de L. West, J.M: *J. Inst. Met.*, vol.92, 1963-64, p.208.
- 26) Cordovilla, C.G. Louis, P. Pamies, A: "The Surface Tension of Liquid Pure Aluminium and Aluminum-Magnesium Alloy", *J. Mater. Sci.*, vol.21, 1986, pp.2787-2792.
- 27) Bykova, N.A. Shevchenko, V.G: *Tr. Inst. Khim. Ural. Nauchn. Tsentr. Akad. Nauk SSR.*, vol.29, 1974, p.42. (Russian)
- 28) Laty, P. Joud, J.C. Desré: "Tension Superficielle D'Alliages Liquides Aluminium-Cuivre", *Surf. Sci.*, vol.69, pp.508-520. (French)
- 29) Yatsenko, S.P. Kononenko, V.I. Sukhman, A.L: "Experimental Studies of the Temperature Dependence of the Surface Tension and Density of Tin, Indium, Aluminium, and Gallium", Translated from *Teplofizika Vysokikh Temperatur.*, vol.10, (1), 1972, pp.66-71.

- 30) Pelzel, E: *Berg Hüttenmänn. Montatsh.*, vol.93, 1948, pp.247.
- 31) Pelzel, E: *Berg Hüttenmänn. Montatsh.*, vol.94, 1949, pp.10.
- 32) Gourmiri, L. Joud, J.C: "Auger Electron Spectroscopy Study of Aluminium-Tin Liquid System", *Acta Metall.*, vol.30, 1982, p.1397-1405.
- 33) Eustathopoulos, N. Joude, J.C. Desré, P. Hicter, J.M: *J. Mater. Sci.*, vol.9, 1974, p. 1233.
- 34) Vatolin, N.A. Esin, O.A. Ukhov, V.F. Dubinin, E.L: *Tr. Inst. Metall. (Sverdlovsk)*, vol.18, 1969, p.73. (Russian)
- 35) Pamies, A. Garcia Cordovilla, C. Louis, E: "The Measurement of Surface Tension of Liquid Aluminum by Means of the Maximum Bubble Pressure Method: The Effect of Surface Oxidation", *Scr. Metall.*, vol. 18, 1984, p. 869-872.
- 36) Janaf Thermodynamical Tables, 2<sup>nd</sup> ed., Edited by Still, D.R. Prophet, H.P., 1971.
- 37) Chacón, E. Flores, F. Navascués: "A Theory for Liquid Metal Surface Tension", *J. Phys. F: Met. Phys.*, vol.14, 1984, pp.1587-1601.
- 38) Anson, J.P. Drew, R.A.L. Gruzleski, J.E: "The Surface Tension of Molten Aluminum and Al-Si-Mg Alloy under Vacuum and Hydrogen Atmospheres", *Metallurgical and Materials Transactions B*, vol.30B, 1999, pp.1027-1032.
- 39) Franses, E.I. Basaran, O.A. Chang, C-H: "Techniques to Measure Dynamic Surface Tension", *Current Opinion in Colloid and Interface Science*, vol.1, 1996, pp.296-303.
- 40) Ricci, E. Nanni, L. Passerone, A: "Oxygen Transport and Dynamic Surface Tension of Liquid Metals", *Phil. Trans. R. Soc. Lond. A*, vol.356, pp.857-870.
- 41) Raleigh, J.S.W: "On the Instability of Jets", *Proc. London Math Soc.*, vol.10, 1879, pp.4-13.
- 42) Bashworth, F. Adams, J.C: An Attempt to Test the Theory of Capillary Action, Cambridge University Press, Cambridge, 1892.
- 43) Andreas, J.M. Hauser, E.A, Tucker, W.B: *J. Phys. Chem.*, vol.42, 1938, p.1001.
- 44) Harkins, W.D.Brown, F.E: *J. Am. Chem. Soc.*, vol.14, 1919, p.499.

- 45) Schrödinger, R: *Ann. Phys.*, vol.46, 1915, p.413.
- 46) Goicoechea, J. Garcia-Cordovilla, C. Louis, E. Pamies, A. "Effects of Wetting and Surface Oxidation on the Measurement of the Surface Tension of Al by the Maximum Bubble Pressure Method", *Scripta Metall.*, vol.25, 1991, pp.279-484.
- 47) DuNoüy, L: *J. Gen. Physiol.*, vol.1, 1919, p.521.
- 48) Andrade, E.N: *Philos. Mag* ,vol.17, 1934, p.698.
- 49) ASM Handbook : Alloy Phase Diagrams, vol.3, ASM International, 1999, p.2-48.
- 50) Knappwost, A.C: *Z. Metallk.*, vol.39, p.314.
- 51) Roscoe, R. Bainbridge, W: *Proc. Phys. Soc.*, vol.72, 1958, p.585.
- 52) Beyer, R.T, Ring, E.M: "The Viscosity of Liquid Metals", From Liquid Metals: Chemistry and Physics, Marcel Dekker Inc, New York, p.431-457.
- 53) Jones, W.R.D. Bartlett, W.L: "The Viscosity of Aluminium and Binary Aluminium Alloys", *J.I.M.*, vol.81, 1952-53, pp.145-152.
- 54) Yao, T.O. Kondic, V: "The Viscosity of Molten Tin, Lead, Zinc, Aluminium, and some of their Alloys", *J.I.M.*, vol.81, 1952-53, pp.17-24.
- 55) Rothwell, E: "A Precise Determination of the Viscosity of Liquid Tin, Lead, Bismuth, and Aluminum by an Absolute Method", *J.I.M.*, vol.90, 1961-62, pp.389-394.
- 56) Kisun'ko, V.Z. Novokhatskii, I.A. Beloborodov, A.Z. Bychkov, Y.B Pogorelov, A.I: "Viscosity of Secondary Aluminum Alloys with Si, Mn, Cu, and Mg", *Tsvetnaya Metallurgiya (Non-Ferrous)*, vol. 24, (1), 1983, pp.84-85.
- 57) Allen, B.C: "The Surface Tension of Liquid Metals", From Liquid Metals: Chemistry and Physics, Marcel Dekker Inc, New York, p.161-212.
- 58) Patrov, B.V. Polous, V.A. Barannik, I.A: "Interfacial Tension Between Magnesium Alloys and Chloride-Fluoride Melts", Translated from *Zhurnal Prikladnoi Khimii*, vol.57, (11), 1982, pp.2452-2455.
- 59) Kiljanski, T: "Discharge Coefficient for Free Jets from Orifice at Low Reynolds Number", *Journal of Fluids Engineering*, vol.115, 1993, 778-781.
- 60) Lienhard, J.H, Lienhard, J.H: "Velocity Coefficients for Free Jets from Sharp-Edged Orifices", *Journal of Fluids Engineering*, vol.106, 1984, pp. 13-17.

- 61) CRC Handbook of Chemistry and Physics, 49<sup>th</sup> ed. Edited by Weast, R.C, The Chemical Rubber Co., Cleveland, 1968.
- 62) John Bowen, Alfa Aesar, Ward Hill, Ma, private communication, Oct 2/2000.
- 63) Hoke, B.C. Chen, J.C: "Binary Aqueous-Organic Surface Tension Temperature Dependence", *J. Chem. Eng. Data*, vol.36, 1991, pp.322-326.
- 64) Taylor, J.R: An Introduction to Error Analysis: The Study of Uncertainties in Physical Measurements, 2<sup>nd</sup> ed., University Science Books, Sausalito Ca, 1997, p.75.
- 65) Herschel, W. H: "No. 100, Determination of Absolute Viscosity by Short-Tube Viscometers", *Technologic Papers of the Bureau of Standards*, 1917, pp. 3-55.
- 66) Herschel, W. H: "No. 112, Standardization of the Saybolt Universal Viscometer", *Technologic Papers of the Bureau of Standards*, 1919, pp. 3-25.
- 67) Herschel, W.H: "The Saybolt Viscosity of Oil Blends", *Chemical and Metallurgical Engineering*, vol.22, (24), 1920, pp. 1109-1112.
- 68) Osborne, W. F: " Lubrication-The Saybolt Viscosimeter", *Power*, vol. 55, (10), 1922, pp. 376-377.
- 69) Herschel, W.H: "The Change in Viscosity of Oils with the Temperature", *Journal of Industrial and Engineering Chemistry*, vol.14, (8), 1922, pp. 715-724.
- 70) Herschel, W.H: "Bath Temperatures of Viscometers of the Saybolt Type", *Industrial and Engineering Chemistry*, vol.15, (1), 1923, pp. 945-946.
- 71) Barr, G: A Monograph of Viscometry, Oxford University Press. London, 1931, pp. 97-102.
- 72) Bates, R. L: "Guide to Industrial Viscometry", *Chemical Engineering*, April 4, 1960, pp. 145-148.
- 73) Van Wazer, J. R. Lyons, J. W. Kim, K. Y. Colwell, R. E: Viscosity and Flow Measurement: A Laboratory Handbook of Rheology, Interscience Publishers, New York, 1963, pp.258-262.
- 74) Anaya, C. Bermudez, O: "Saybolt Universal Viscosity Converted to Kinematic", *Oil and Gas Journal*, Sept 21, 1987, pp. 98-100.
- 75) Anaya, C. Bermudez, O: "Converts Saybolt Furol Viscosities to Kinematic", *Oil and Gas Journal*, Nov 28, 1988, pp. 72-73.



- 76) Webster, J. G: "The Measurement, Instrumentation, and Sensor Handbook, CRC Press, Boca Raton, Fla, 1999.
- 77) ASTM Standard Test Method for: "Standard Test Method for Saybolt Viscosity", ASTM Designation D 88-94, 1999.
- 78) ASTM Standard Test Method for: "Standard Practice for Conversion of Kinematic Viscosity to Saybolt Universal Viscosity or to Saybolt Furol Viscosity", ASTM Designation D 2161-93, 1999.
- 79) Daugherty, R.L. Franzini, J.B. Finnemore, E.J: Fluid Mechanics with Engineering Applications, 8<sup>th</sup> ed., McGraw-Hill, New York, 1985, pp.450-451.
- 80) Whitaker, S: Introduction to Fluid Mechanics, Prentice Hall, New Jersey, 1968, pp. 32-252.

## APPENDIX A: QUANTIFYING TRANSIENT TERMS

The quasi-steady state approximation made in Chapter 4 for the Bernoulli formulation will be validated in this Appendix. Water at room temperature was used. The dimensions of the orifice and the crucible are illustrated in Figures 3.4 and 3.5. The radius of the vessel,  $r_v$ , is 0.045m and the radius of the orifice is 0.0025m.

From the Bernoulli formulation, Equation (71) was developed in Section 4.1:

$$u_2 = \sqrt{2g \left( h - \frac{(P_2 - P_1)}{\rho g} - \frac{h}{g} \left( \frac{\partial u}{\partial t} \right) \right)} \quad (71)$$

The accelerative head term,  $(h/g)(\partial u/\partial t)$ , is included in the formulation unless the quasi-steady state approximation is made. The pressures at the free surface and orifice tip are also included for the purposes of this analysis. If the accelerative head term is considered within the vessel and orifice separately, the following equation is stated:

$$u_2 = \sqrt{2g \left( h - \frac{(P_2 - P_1)}{\rho g} - \frac{(h - 0.0097)}{g} \left( \frac{\partial u_1}{\partial t} \right) - \frac{(0.0097)}{g} \left( \frac{\partial u_2}{\partial t} \right) \right)} \quad (A1)$$

This equation assumes that there is an instantaneous change in velocity from  $u_1$  and  $u_2$  at the entrance of the orifice. Recall from Chapter 3 that the height of the orifice plate is 0.0097m (9.7mm). The terms  $\partial u_1/\partial t$  and  $\partial u_2/\partial t$  can be determined by plotting  $u_1$  and  $u_2$  as a function of time. Refer to Figure A.1, which indicates a linear relationship. The slope of the curves depicted in Figure A.2 represents the gradients  $\partial u_1/\partial t$  and  $\partial u_2/\partial t$ . Note that these velocities were determined experimentally.

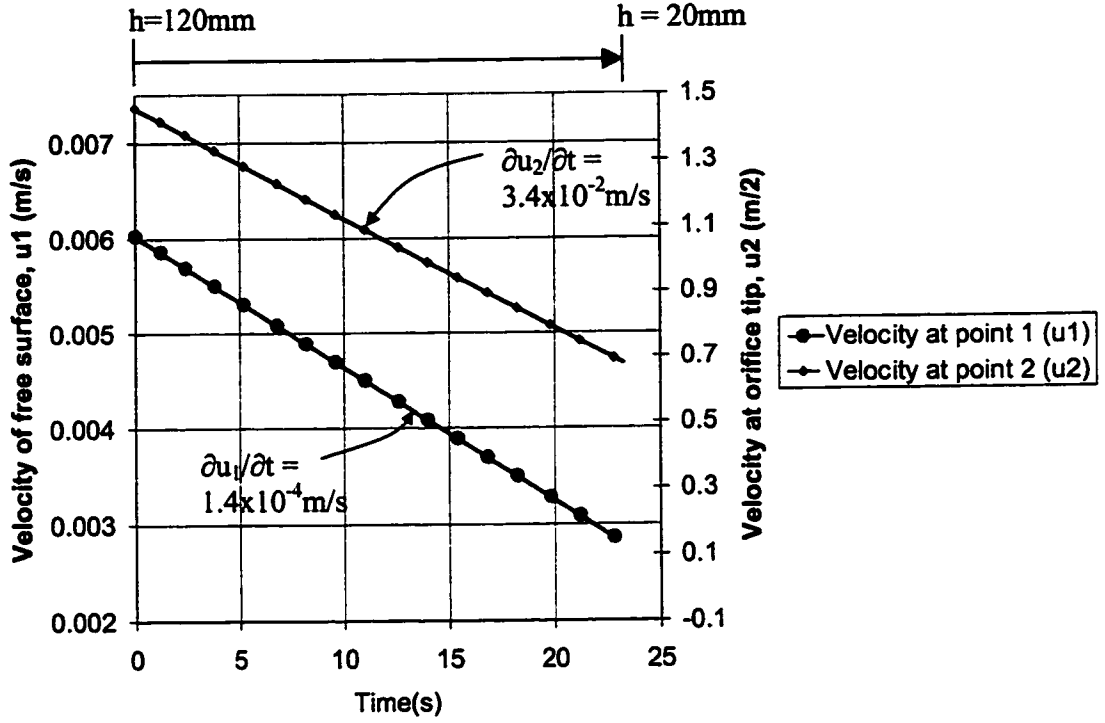


**Figure A.1: Velocity at reference points 1 and 2 indicated in Figure 4.1 as a function of time.**

The frictional characteristics of the orifice can now be determined using Equation

(A1):

$$C_d = \frac{Q_{exp}}{\pi r_o^2 \sqrt{2g \left( h - \frac{(P_2 - P_1)}{\rho g} - \frac{(h - 0.0097)}{g} \left( \frac{du_1}{dt} \right) - \frac{(0.0097)}{g} \left( \frac{du_2}{dt} \right) \right)}} \quad (A2)$$

Two cases will be presented. The first case will neglect surface tension in the analysis (i.e.  $P_1 = P_2$ ). The second case will state that there is pressure induced at the orifice tip due to the effects of surface tension ( $P_1 = 1 \text{ atm}$ ,  $P_2 = 1 \text{ atm} + \sigma/r_o$ ). This relationship will be compared with the formulation that assumes the quasi-steady state approximation:

$$C_d = \frac{Q_{exp}}{\pi r_o^2 \sqrt{2g \left( h - \frac{(P_2 - P_1)}{\rho g} \right)}} \quad (A3)$$

It is clear from Figure A.2 that the quasi-steady state assumption is a valid one since there is no difference between Equation (A2) and (A3). There is, however, a distinct difference if pressure effects due to surface tension are neglected in the analysis. This confirms that the quantification of surface tension in Section 4.2 is not affected by secondary effects derived from the transient effects of these experiments.

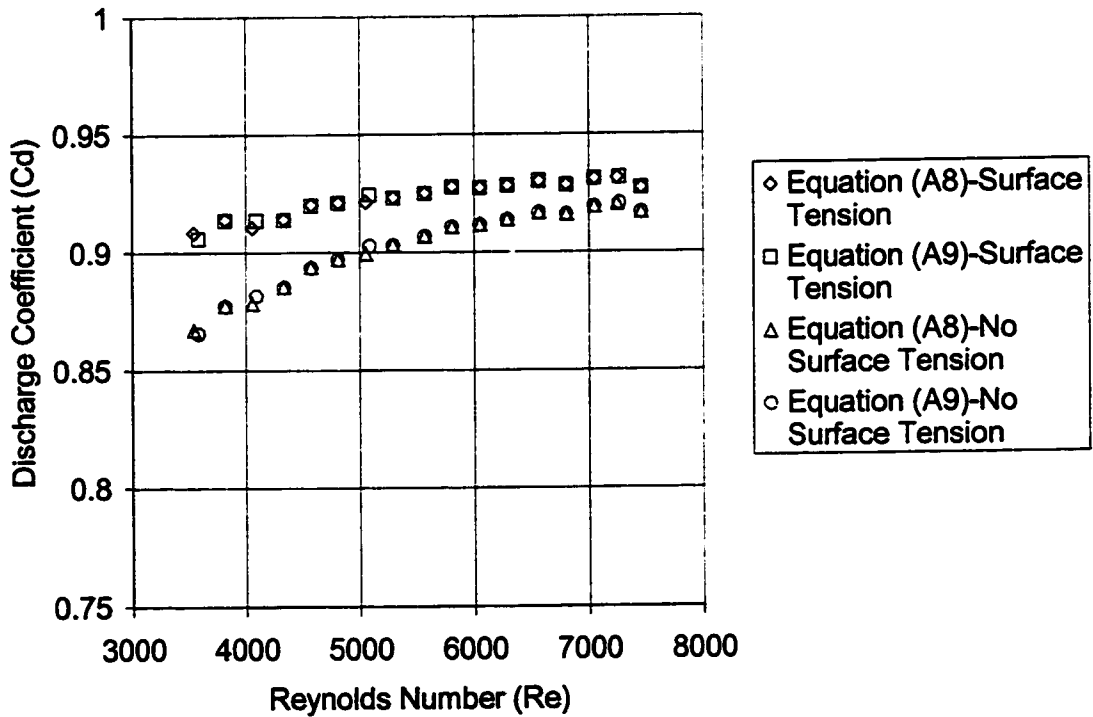


**Figure A.2: Discharge coefficient as a function of Reynolds number taking into account transient terms in the formulation.**

## **APPENDIX B:      MULTIPLE NON LINEAR REGRESSION PROGRAMS**

### **Legend of Symbols for Programs**

<b>A =</b>	<b>Surface tension (N/m).</b>
<b>Atol =</b>	<b>Surface tension calculated from previous iteration (N/m).</b>
<b>B =</b>	<b>Density (<math>\text{kg/m}^3</math>).</b>
<b>Btol =</b>	<b>Density calculated from previous iteration (<math>\text{kg/m}^3</math>).</b>
<b>C =</b>	<b>Viscosity (<math>\text{Ns/m}^2</math>).</b>
<b>Ctol =</b>	<b>Viscosity calculated from previous iteration (<math>\text{Ns/m}^2</math>).</b>
<b>c1 =</b>	<b>Polynomial constant (<math>\text{Re}^3</math> term) (no units).</b>
<b>c2 =</b>	<b>Polynomial constant (<math>\text{Re}^2</math> term) (no units).</b>
<b>c3 =</b>	<b>Polynomial constant (<math>\text{Re}</math> term) (no units).</b>
<b>c4 =</b>	<b>Polynomial constant (no units).</b>
<b>g =</b>	<b>Gravitational constant (<math>9.81 \text{ m/s}^2</math>).</b>
<b>h =</b>	<b>Head (m).</b>
<b>i =</b>	<b>Iteration number and position of value in vector (<math>i = 1</math> to <math>n</math>) (no units).</b>
<b>n =</b>	<b>Length of vector containing data (no units).</b>
<b>ncount =</b>	<b># of iterations (no units).</b>
<b>nsum =</b>	<b>0 when convergence is not met with respect to A, B, C.</b>
<b>ntol =</b>	<b>Condition where all three properties converge within limit of tol (<math>\text{ntol} = 3</math> when solving for surface tension, density and viscosity; <math>\text{ntol} = 2</math> when solving for surface tension and viscosity only) (no units).</b>
<b>Q =</b>	<b>Flow rate (g/s).</b>
<b>r =</b>	<b>Orifice radius (m).</b>
<b>tol =</b>	<b>Convergence tolerance for surface tension, viscosity and density (no units).</b>

V = Flux ( $\text{kg/m}^2/\text{s}$ ).

y = Vector corresponding to difference between experimental and calculated head data (m).

z = Matrix of partial derivatives with respect to A, B, C.

**Program # 1: Solving for Surface Tension, Viscosity and Density Simultaneously.**

```
function value = surf2(h,Q,A,B,C,tol)
```

```
% This program determines the coefficients for nonlinear regression on % Surface  
Tension Viscosity and Density
```

```
% Insert vectors of data for flow rate and head here:
```

```
Q=[];
```

```
h=[];
```

```
% Initial Guess for Surface Tension:
```

```
A=0.5;
```

```
% Initial Guess for Density:
```

```
B=2000;
```

```
% Initial Guess for Viscosity:
```

```
C=1e-4;
```

```
% Radius of orifice:
```

```
r=2.50/1000;
```

```
% Constants related to 3rd order polynomial for discharge coefficient % vs Reynolds  
number (assuming linear relation)
```

```
%  $C_d=c_1*Re^3+c_2*Re^2+c_3*Re+c_4$ :
```

```
c1=0;
```

```
c2=0;
```

```
c3=2.196E-06;
```

```
c4= 0.914;
```

```
% Tolerance that calculation must reach for convergence criterion:
```

```
tol=0.000001;
```

```
ntol =1;
```

```
% Initiate count
```

```
ncount =0;
```

```
g=9.81;
```

```
% determine size of problem:
```

```
n=length(Q);
```

```
% Calculate flux from flow rate data:
```

```
for i=1:n
```

```
    V(i,1)=Q(i)/(1000*pi*(r)^2);
```

```
end
```

```
% Set Conditions for Convergence
```

```

Atol=1;
Btol=1;
Ctol=1;

% Convergence check loop
while ntol == 1
    ncount=ncount+1;
% Set up matrices to be solved. First Y matrix:
    for i = 1:n
        y(i,1)=(h(i)+9.7/1000-0.0004)-1/(2*g)*(c1*B*V(i)^2*(2*r)^3/C^3
            +c2*B*V(i)*(2*r)^2/C^2+c3*B*(2*r)/C+c4*B/V(i))^(-2)-A/(B*g*r);
    end
% Set up Z matrix:
    for i = 1:n
        z(i,1)=1/(B*g*r);
        z(i,2)=1/g*(c1*B*V(i)^2*(2*r)^3/C^3+c2*B*V(i)*(2*r)^2/C^2
            +c3*B*(2*r)/C+c4*B/V(i))^(-3)*(c1*V(i)^2*(2*r)^3/C^3
            +c2*V(i)*(2*r)^2/C^2+c3*(2*r)/C+c4/V(i))-A/(g*r*B^2);
        z(i,3)=1/g*(c1*B*V(i)^2*(2*r)^3/C^3+c2*B*V(i)*(2*r)^2/C^2
            +c3*B*(2*r)/C+c4*B/V(i))^(-3)*(3*c1*B*V(i)^2*(2*r)^3/C^4
            +2*c2*B*V(i)*(2*r)^2/C^3+c3*B*(2*r)/C^2);
    end
% Solve for x where [y]=[z][x]:
    x=inv(transpose(z)*z)*transpose(z)*y;
% Maximum number of iterations allowed:
    if ncount > 100
        return
    end
% Determine new values of A,B,C:
    A = A+x(1);
    B = B+x(2);
    C = C+x(3);
% Tolerance check:
    nsum = 0;

    if abs((A-Atol)/Atol) < tol
        nsum = nsum + 1;
    end

    if abs((B-Btol)/Btol) < tol
        nsum = nsum + 1;
    end

    if abs((C-Ctol)/Ctol) < tol
        nsum = nsum + 1;
    end
end

```

```

if nsum == 3 % if all variables meet convergence then
    ntol = 0;
end

% Redefine initial tolerance check variables
Atol=A;
Btol=B;
Ctol=C;

```

```

end

```

```

% Output Results:
SurfaceTension=A
Density=B
Viscosity=C

```

## **Program # 2: Solving for Surface Tension and Viscosity Simultaneously.**

```

function value = surf2(h,Q,A,C,tol)
% This program determines the coefficients for nonlinear regression on %Surface
Tension and Viscosity only
% Insert vectors of data for flow rate and head here:
Q=[];
h=[];

% Initial Guess for Surface Tension:
A=0.5;
% Initial Guess for Viscosity:
C=1e-4;
% Radius of orifice:
r=2.50/1000;

% Constants related to 3rd order polynomial for discharge coefficient % % vs Reynolds
number (assuming linear relation)
%  $C_d = c_1 * Re^3 + c_2 * Re^2 + c_3 * Re + c_4$ :
c1=0;
c2=0;
c3=2.196E-06;
c4= 0.914;
% Tolerance that calculation must reach for convergence criterion:
tol=0.000001;
ntol =1;
% Initiate count
ncount =0;
g=9.81;
% determine size of problem:

```



```

n=length(Q);

% Calculate flux from flow rate data:
for i=1:n
    V(i,1)=Q(i)/(1000*pi*(r)^2);
end

% Set Conditions for Convergence
Atol=1;
Ctol=1;

%convergence check loop
while ntol == 1
    ncount=ncount+1;
% Set up matrices to be solved. First Y matrix:
for i = 1:n
    y(i,1)=(h(i)+9.7/1000-0.0004)-1/(2*g)*(c1*B*V(i)^2*(2*r)^3/C^3
        +c2*B*V(i)*(2*r)^2/C^2+c3*B*(2*r)/C
        +c4*B/V(i)^(-2)-A/(B*g*r);
end
% Set up Z matrix:
for i = 1:n
    z(i,1)=1/(B*g*r);
    z(i,2)=1/g*(c1*B*V(i)^2*(2*r)^3/C^3+c2*B*V(i)*(2*r)^2/C^2
        +c3*B*(2*r)/C+c4*B/V(i)^(-3)*(3*c1*B*V(i)^2*(2*r)^3/C^4
        +2*c2*B*V(i)*(2*r)^2/C^3+c3*B*(2*r)/C^2);
end
% Solve for x where [y]=[z][x]:
x=inv(transpose(z)*z)*transpose(z)*y;
% maximum number of iterations allowed:
if ncount > 100
    return
end
% Determine new values of A,B,C:
A = A+x(1);
C = C+x(2);
% Tolerance check:
nsum = 0;

if abs((A-Atol)/Atol) < tol
    nsum = nsum + 1;
end
if abs((C-Ctol)/Ctol) < tol
    nsum = nsum + 1;
end
if nsum ==2 % if all variables meet convergence then

```

```
        ntol = 0;
end

% Redefine initial tolerance check variables
    Atol=A;
    Ctol=C;
end

% Output Results:
SurfaceTension=A
Viscosity=C
```

# **APPENDIX C: SURFACE TENSION AND VISCOSITY OF ALUMINUM (REGRESSION ON ALL THREE PROPERTIES)**

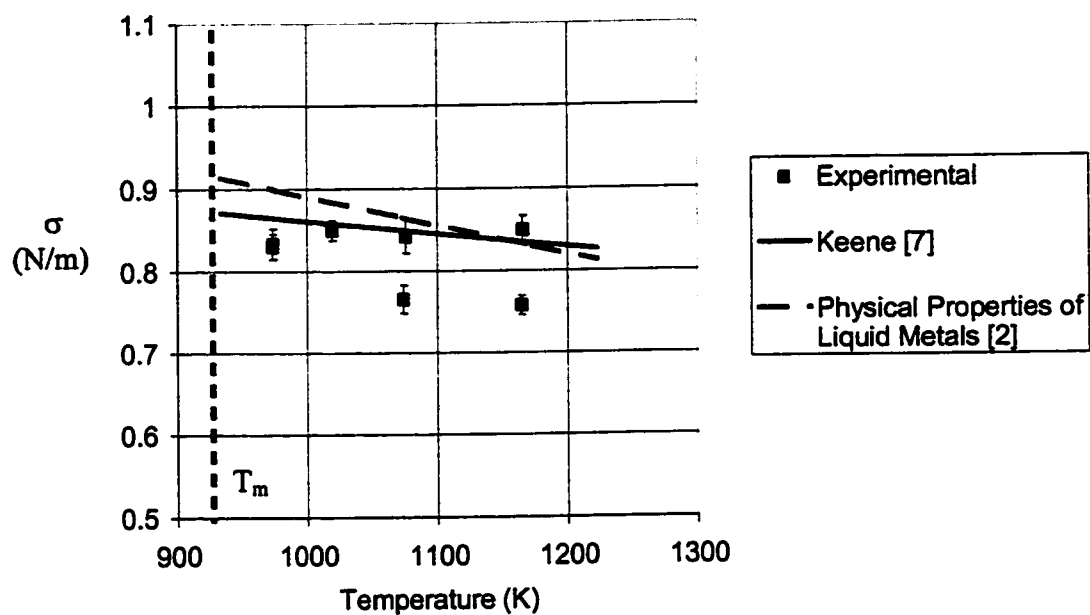


**Figure C.1: Surface tension of aluminum as a function of temperature determined through multiple non-linear regression on all three properties.**

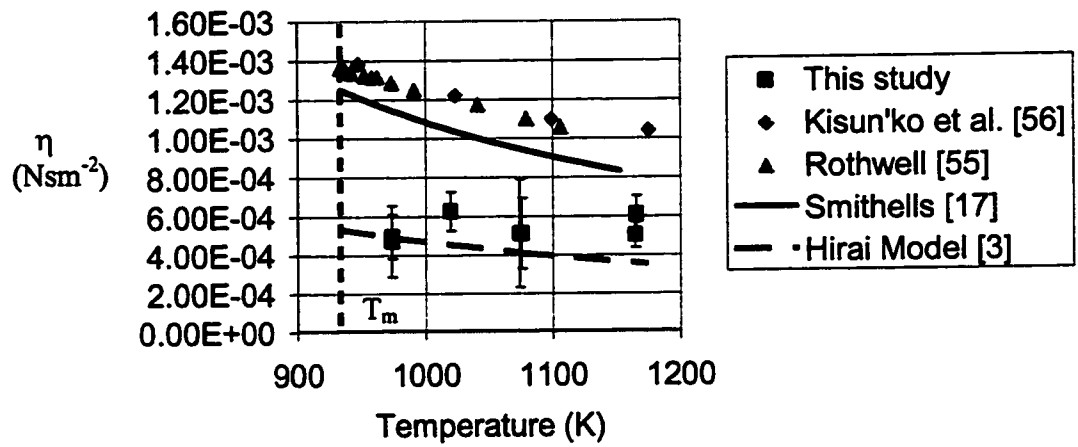


**Figure C.2: Viscosity of aluminum as a function of temperature determined through multiple non-linear regression on all three properties.**

## APPENDIX D: OXYGEN PARTIAL PRESSURE

During the heating cycle, the oxygen content was measured every 30s and monitored as a function of temperature. The partial pressure of oxygen after purging is approximately 2Pa ( $\approx 20$ ppm) as discussed in Chapter 3. Once this level is achieved, the aluminum is heated to the desired temperature. Near the melting point, a rapid decrease in oxygen content is observed, corresponding to oxidation of the aluminum or AZ91D alloy. This means that oxygen entering the tower is rapidly consumed in the reaction. Under repeatable conditions, and once the material is molten, the oxygen level steadily ascends to the original level ( $\approx 20$ ppm) indicating that the system has stabilized. The melt is held at the specified temperature for approximately 30 min to give the system time to stabilize to the nominal oxygen pressure. If the oxygen partial pressure is plotted against temperature, a curve similar to what is represented in Figure 6.4 is produced.

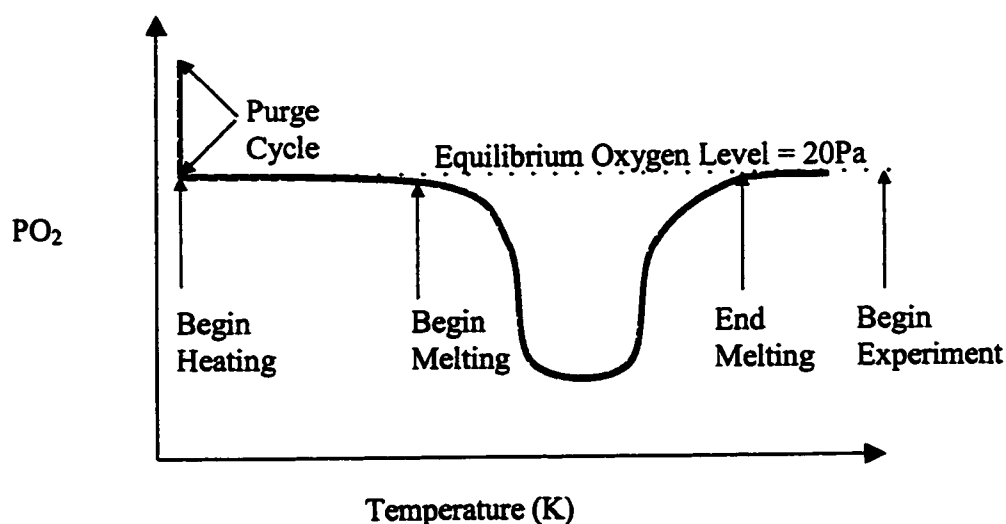


**Figure D.1: Representation for the partial pressure of oxygen as a function of temperature during a purging and heating cycle.**

A plot similar to Figure D.1 was generated for aluminum at 973 K (Figure D.2), 1023 K (Figure D.3), 1073 K (Figure D.4) and 1173 K (Figure D.5). AZ91D alloy heated to 967 K is also represented in Figure D.6. Each data point on these charts represents a measurement taken every 30 seconds.

It is clear from Figure D.5 that the oxygen did not reach the nominal oxygen pressure (20ppm) in the apparatus when the experiment commenced. As the temperature climbed past 1100 K, the oxygen partial pressure experienced another decrease with temperature. This is typical of experiments with aluminum when the temperature is increased beyond 1073 K, and is attributed to an increase in reactivity. The same can be stated for all experiments with AZ91D alloy. It is clear from Figure D.6 that the system did not reach the nominal concentration of 20ppm due to the high reactivity of magnesium in the presence of oxygen. The conclusion drawn from Figures D.2 through D.6 is that aluminum experiments above 1073K, and all AZ91D experiments, were performed under oxygen conditions different than the aluminum experiments at lower temperatures ( $< 1073$  K).

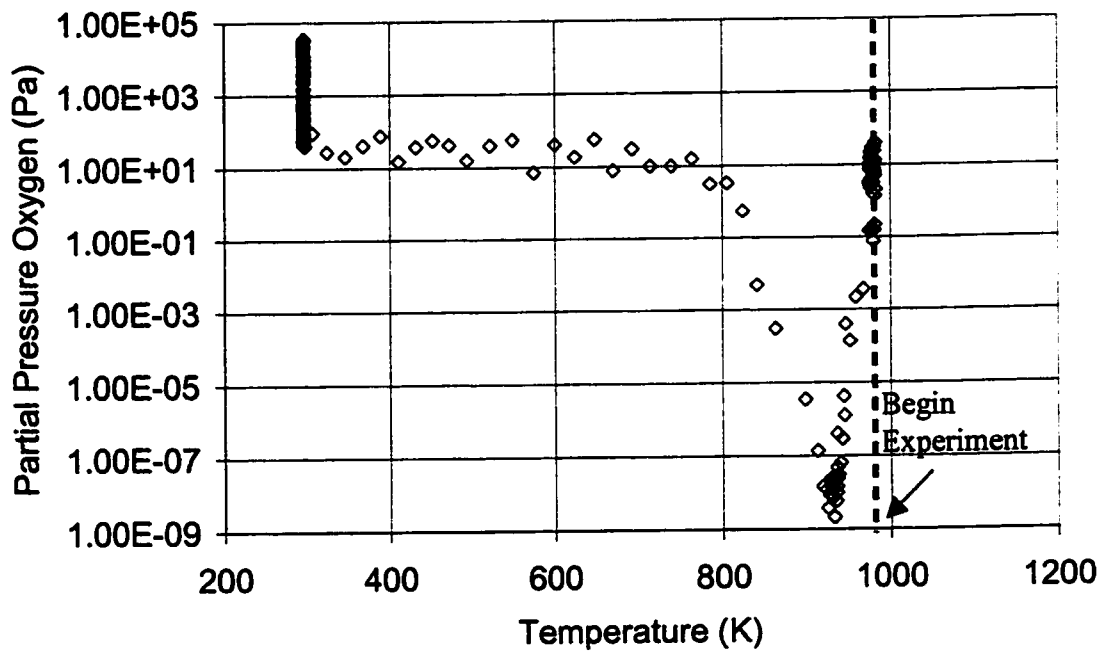


**Figure D.2: Oxygen partial pressure during the purging and heating cycle for Aluminum Test #31 up to 973 K.**

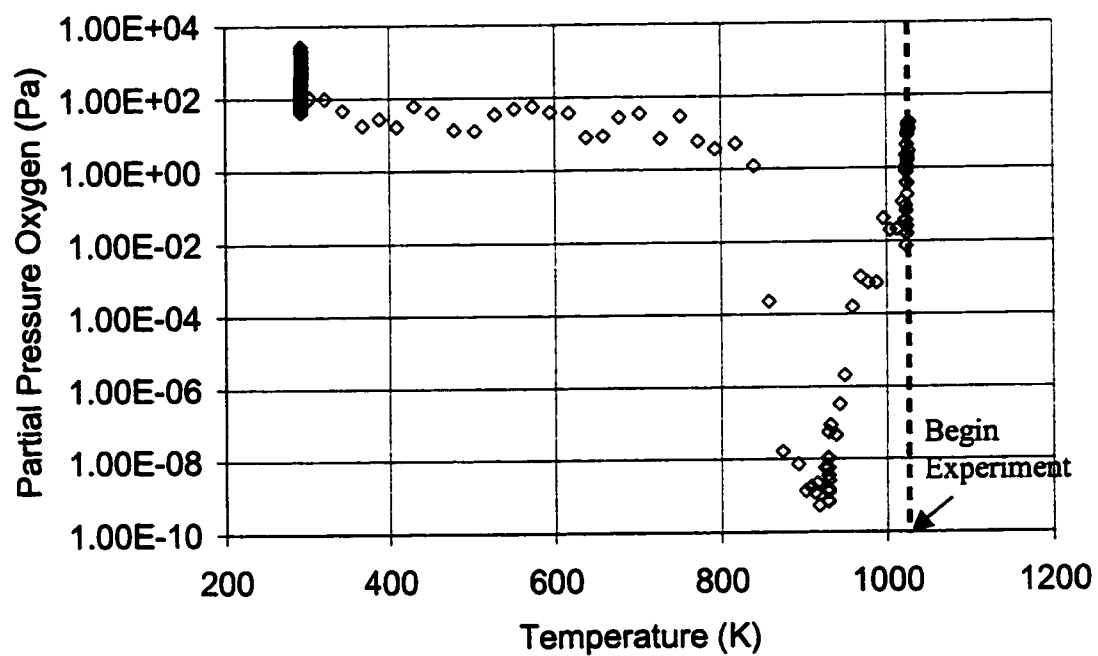


**Figure D.3: Oxygen partial pressure during the purging and heating cycle for Aluminum Test #38 up to 1023 K.**



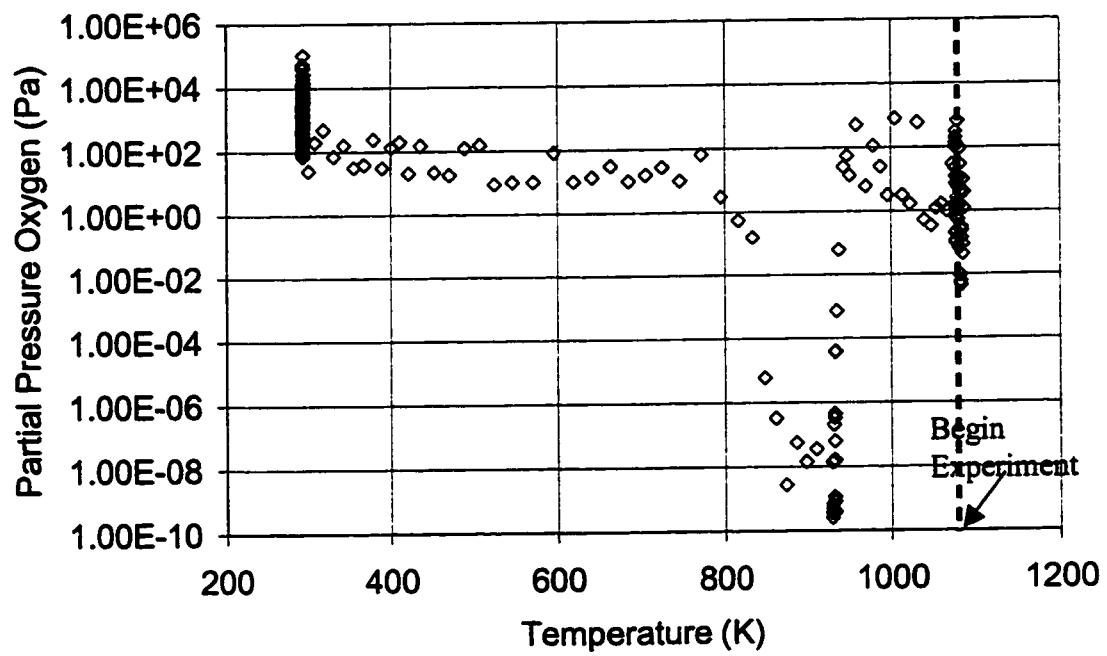
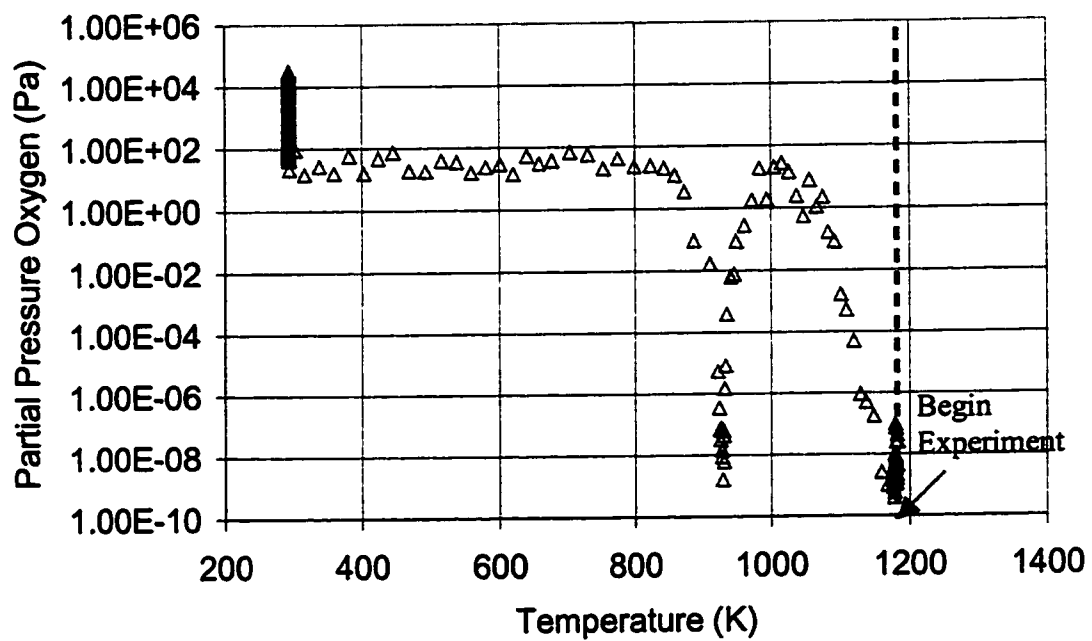


**Figure D.4: Oxygen partial pressure during the purging and heating cycle for Aluminum Test #35 up to 1073 K.**



**D.5: Oxygen partial pressure during the purging and heating cycle for Aluminum Test #39 up to 1173 K.**

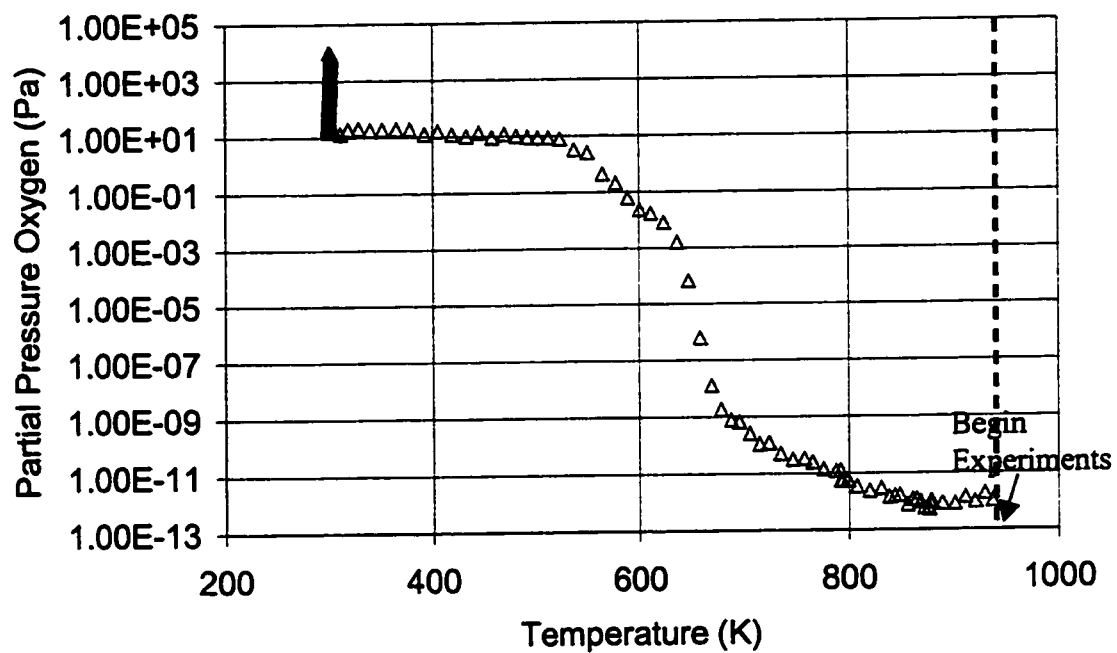


**Figure D.6: Oxygen partial pressure during the purging and heating cycle for AZ91D Test #2 up to 967 K.**